Article:

Viaro, S. and Ricco, P. orcid.org/0000-0003-1537-1667 (2019) Compressible unsteady Görtler vortices subject to free-stream vortical disturbances. Journal of Fluid Mechanics, 867. pp. 250-299. ISSN 0022-1120

https://doi.org/10.1017/jfm.2019.83

Compressible unsteady Görtler vortices subject to free-stream vortical disturbances

Samuele Viaro[1]† and Pierre Ricco[1]

[1]Department of Mechanical Engineering, The University of Sheffield, Sheffield, S1 3JD, UK

(Received xx; revised xx; accepted xx)

The perturbations triggered by free-stream vortical disturbances in compressible boundary layers developing over concave walls are studied numerically and through asymptotic methods. We employ an asymptotic framework based on the limit of high Görtler number, the scaled parameter defining the centrifugal effects, we use an eigenvalue formulation where the free-stream forcing is neglected, and solve the receptivity problem by integrating the compressible boundary-region equations complemented by appropriate initial and boundary conditions that synthesize the influence of the free-stream vortical flow. Near the leading edge, the boundary-layer perturbations develop as thermal Klebanoff modes and, when centrifugal effects become influential, these modes turn into thermal Görtler vortices, i.e., streamwise rolls characterized by intense velocity and temperature perturbations. The high-Görtler-number asymptotic analysis reveals the condition for which the Görtler vortices start to grow. The Mach number is destabilizing when the spanwise diffusion is negligible and stabilizing when the boundary-layer thickness is comparable with the spanwise wavelength of the vortices. When the Görtler number is large, the theoretical analysis also shows that the vortices move towards the wall as the Mach number increases. These results are confirmed by the receptivity analysis, which additionally clarifies that the temperature perturbations respond to this reversed behavior further downstream than the velocity perturbations. A matched-asymptotic composite profile, found by combining the inviscid core solution and the near-wall viscous solution, agrees well with the receptivity profile sufficiently downstream and at high Görtler number. The Görtler vortices tend to move towards the boundary-layer core when the flow is more stable, i.e., as the frequency or the Mach number increase, or when the curvature decreases. As a consequence, a region of unperturbed flow is generated near the wall. We also find that the streamwise length scale of the boundary-layer perturbations is always smaller than the free-stream streamwise wavelength. During the initial development of the vortices, only the receptivity calculations are accurate. At streamwise locations where the free-stream disturbances have fully decayed, the growth rate and wavelength are computed with sufficient accuracy by the eigenvalue analysis, although the correct amplitude and evolution of the Görtler vortices can only be determined by the receptivity calculations. It is further proved that the eigenvalue predictions of the growth rate and wavenumber worsen as the Mach number increases as these quantities show a dependence on the wall-normal direction. We conclude by qualitatively comparing our results with the direct numerical simulations available in the literature.

Key words: Compressible boundary layer, Görtler instability, receptivity.

---

† Email address for correspondence: sviaro1@sheffield.ac.uk

1. Introduction

In 1940 Görtler (1940) published a paper where a new type of boundary-layer instability was introduced. This instability originates from an inviscid unbalance between pressure and centrifugal forces caused by the curvature of flow streamlines. The resulting perturbation evolves in the form of counter-rotating vortices that are elongated in the streamwise direction. They have been referred to as Görtler vortices. Görtler's mathematical result was confirmed experimentally by Liepmann (1945), who first showed that transition to turbulence is anticipated with respect to the flat-plate case. Comprehensive reviews on Görtler flow have been published by Hall (1990), Floryan (1991), and Saric (1994).

1.1. *Incompressible Görtler vortices*

The original work of Görtler (1940) was based on a theory that was simplified by the parallel mean-flow assumption, in contrast with the growing nature of boundary layers. Tani (1962) first performed detailed measurements of the perturbed flow proving that Görtler vortices evolve with a nearly constant spanwise wavelength. An improvement to the original theory was achieved in the work of Floryan & Saric (1982) by introducing non-parallel effects and using other assumptions that led to an eigenvalue system of ordinary differential equations. When the spanwise wavelength of Görtler vortices is of the same order as the boundary-layer thickness, Hall (1983) demonstrated that any theory simplifying the governing partial differential equations to ordinary differential equations does not lead to a precise description of the evolution of the Görtler vortices, so that for example the amplitude of the perturbations, the dependence of the growth rate on the wall-normal direction, and the flow behaviour near the leading edge would not be computed correctly. In Hall (1983) several disturbance profiles were introduced at different streamwise locations near the leading edge as initial conditions and, for each location and initial profile, the instability developed in a different manner. The influence of the external disturbances was not accounted for and the perturbations were assumed to vanish outside of the boundary layer. Swearingen & Blackwelder (1983) and Kottke (1988) proved experimentally that the receptivity of the base flow to free-stream turbulence, i.e., the process by which external disturbances interact with the boundary layer to trigger instability, has a strong impact on the properties of Görtler instability, such as the spanwise wavelength, and on the breakdown of the vortices to turbulence. Hall (1990) was the first to introduce the effect of receptivity to free-stream turbulence on the Görtler vortices, obtaining a better agreement with experimental data than for the cases where artificial initial conditions were imposed at a fixed streamwise location. More recently, Borodulin *et al.* (2017) also claimed that free-stream turbulence is one of the most efficient ways to excite Görtler instability.

For the flat-plate case, a further pioneering step towards understanding receptivity was achieved by Leib *et al.* (1999), who formulated a rigorous mathematical framework based on the unsteady boundary region equations. This framework, through asymptotic matching, unequivocally fixes the initial and outer boundary conditions based on the external free-stream vortical disturbances. Leib *et al.* (1999) focused on the incompressible viscous instabilities that arise in flat-plate boundary layers in the form of streamwise elongated vortices, known as Klebanoff modes, now widely recognized to be initiators of bypass transition to turbulence (Matsubara & Alfredsson 2001; Ovchinnikov *et al.* 2008). Recently, Ricco *et al.* (2016) highlighted the strengths of this theory compared to other theoretical approaches found in literature for the analysis of bypass transition, and proved its validity by showing good agreement with the experimental data and with the direct numerical simulation data of Wu & Moin (2009). When streamwise concave curvature is present, Klebanoff modes turn into Görtler vortices as they evolve downstream. This was first proved by Wu *et al.* (2011) by extending the theory of Leib *et al.* (1999) to flows over concave surfaces where free-stream turbulence was modeled by three-dimensional vortical disturbances. Their theoretical results agree well with the experimental data in the linear region of evolution (Tani 1962; Finnis & Brown 1997; Boiko *et al.* 2010*b*). Viaro & Ricco (2018) adopted the formulation of Wu *et al.* (2011) to compute the neutral curves of Görtler instability triggered by free-stream vortical disturbances, i.e., the curves in the parameter space that distinguish between regions of growth and decay of the boundary-layer perturbations. In the limit of high Görtler number, the asymptotic analysis of Wu *et al.* (2011) revealed the different stages through which the Görtler instability evolves. It undergoes two pre-modal stages before its exponential amplification. During their growth, the vortices become trapped in a wall layer. This is a distinctive feature of incompressible Görtler vortices and it is markedly different from the behavior of Klebanoff modes, which tend to move to the upper part of the boundary layer.

The effects of nonlinearity on the unsteady Görtler vortices triggered by free-stream vortical disturbances have been studied by Boiko *et al.* (2010*a*), Xu *et al.* (2017) and Marensi & Ricco (2017). In addition, the excitation of Görtler vortices by local surface nonuniformities has been recently investigated by Boiko *et al.* (2017).

1.2. *Compressible Görtler vortices*

Transition to turbulence caused by Görtler instability influences the performance of several technological applications, especially in the compressible regime. A typical important example is the high-speed flow in turbine engine intakes, where the free stream is highly disturbed. It is thus crucial to study the influence of free-stream disturbances to predict transition in these systems and to evince how the change of the flow regime from laminar to turbulent affects the performance of turbomachinery (Mayle 1991; Volino & Simon 1995). Additional examples of Görtler flows in the compressible regime include airfoils (Mangalam *et al.* 1985), hypersonic air breathing vehicles (Ciolkosz & Spina 2006), and supersonic nozzles (Chen *et al.* 1992).

Compressible Görtler vortices were originally described by the parallel theory of Hammerlin (1961) and were first visualized by Ginoux (1971). A parallel theory was also employed later by Kobayashi & Kohama (1977) and was further extended to include non-parallel effects by El-Hady & Verma (1983), Hall & Malik (1989), and Hall & Fu (1989). The eigenvalue approach was improved by Spall & Malik (1989) by solving a system of partial differential equations coupled with prescribed initial conditions under the assumption of vanishing perturbations outside the boundary layer. Spall & Malik (1989) also mentioned that physically meaningful initial conditions do require receptivity. This work was later modified by Wadey (1992) through a new set of improved initial conditions, but receptivity was still not introduced. The eigenvalue approach with vanishing perturbations in the free stream was also adopted by Dando & Seddougui (1993) to study compressible Görtler vortices. From these early theories it was first noticed that increasing the Mach number leads to a more stable flow and to a shift of the vortices away from the wall. More recently, two conference papers by Whang & Zhong (2002, 2003) reported direct numerical simulation results on the influence of free-stream disturbances on Görtler vortices in the hypersonic regime, Li *et al.* (2010) investigated the nonlinear development of Görtler instability through nonlinear parabolized stability equations and direct numerical simulations, and Ren & Fu (2015) showed how differences in the primary instability lead to considerable changes in the secondary instability, thereby impacting the transition to turbulence.

Experimental works on compressible Görtler flows are more limited than incompressible flows. De Luca *et al.* (1993) experimentally confirmed that in the compressible regime Görtler vortices also evolve with a constant spanwise wavelength. Ciolkosz & Spina (2006) ran experimental tests on transonic and supersonic Görtler vortices and showed that the spanwise wavelength of the vortices remained approximately constant as the Mach number and Görtler number varied and that the measured growth rates agreed reasonably well with existing stability results. Görtler vortices were also noticed to be the unwanted cause of transition for the design of quiet hypersonic wind tunnels (Schneider 2008). Wang *et al.* (2018) performed a flow visualization of the complete evolution of Görtler vortices from the laminar to the turbulent regime reporting that, although the linear growth rate decreases as the Mach number increases, the secondary instability was enhanced. They also stressed that the theoretical works are steps ahead of the limited number of experimental works on compressible Görtler instability. To the best of our knowledge, rigorous experiments on compressible flows over concave surfaces describing the effect of free-stream turbulence on the Görtler vortices are indeed not available in the literature. This has arguably been one of the reasons why, although progresses have been made, there are no theoretical works on the receptivity of compressible boundary layers over concave surfaces to free-stream vortical disturbances and on the engendered unsteady Görtler vortices.

1.3. *Objective of the paper*

The objective of this paper is to study the receptivity of compressible boundary layers over streamwise-concave surfaces to free-stream vortical disturbances and the consequent growth of unsteady Görtler vortices. We use asymptotic methods and numerical computations to solve the equations of motion. We achieve our goal by combining the theoretical framework of Wu *et al.* (2011) for incompressible flows over concave surfaces and the one of Ricco & Wu (2007), who extended the theory by Leib *et al.* (1999) to study compressible Klebanoff modes over flat surfaces. We focus on boundary layers where the free-stream Mach number is of order one and the instability only takes the form of Görtler vortices, i.e., at sufficiently low frequencies for which oblique Tollmien-Schlichting waves do not appear at realistic streamwise locations. We thus exclude the range of frequencies for which the receptivity mechanism discovered by Ricco & Wu (2007) is operational.

Section §2.1 outlines the flow scaling and decomposition, while §2.2 presents the unsteady boundary-region equations with curvature effects. Starting from these equations, in §2.3 we derive a compressible eigenvalue framework with and without the parallel-flow assumption, while in §3 we adopt an asymptotic framework valid at high Görtler numbers to study the different evolution stages. Section 4 shows the influence of compressibility, radius of curvature, and different oncoming vortical disturbances on the development of the instability. The numerical boundary-region solutions are compared with the eigenvalue and the asymptotic solutions in §4.2 and §4.3, respectively. Qualitative comparisons with the direct numerical simulation (DNS) results by Whang & Zhong (2003) are given in §4.4.

2. Scaling and equations of motion

We consider a uniform compressible air flow of velocity U_∞^* and temperature T_∞^* past a slightly concave plate with constant radius of curvature r^*. Hereinafter the asterisk * identifies dimensional quantities. In the proximity of the surface, the flow is described by the orthogonal curvilinear coordinate system $\mathbf{x} = \{x, y, z\}$ that defines the streamwise, wall-normal, and spanwise directions. Therefore, x is the streamwise coordinate, y is the wall-normal coordinate, and z is the spanwise coordinate, orthogonal to x and y. The

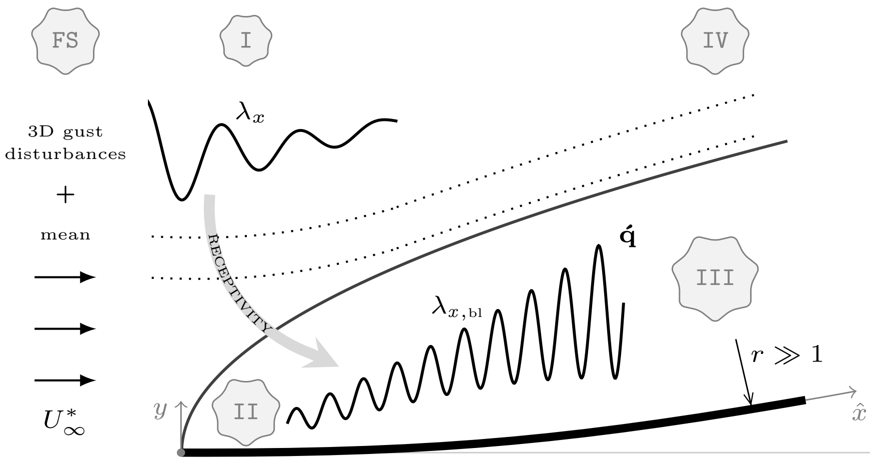

Figure 1: Schematic of the boundary-layer asymptotic regions $\mathtt{I}, \mathtt{II}, \mathtt{III}, \mathtt{IV}, \mathtt{FS}$ and the receptivity mechanism to free-stream vortical disturbances, where λ_x is the streamwise wavelength of the free-stream disturbance and $\lambda_{x,\mathrm{bl}}$ is the streamwise wavelength of the boundary-layer perturbation $\acute{\mathbf{q}}$ sufficiently downstream from the leading edge.

conversion from the Cartesian to the curvilinear coordinates system is achieved through the Lamé coefficients $h_x = 1 - y^*/r^*, h_y = 1$, and $h_z = 1$ which are also used in Wu *et al.* (2011). These coefficients are only valid when $\delta^*/r^* \ll 1$ (Goldstein 1938), where δ^* is a measure of the boundary-layer thickness. This condition is always satisfied in our calculations and therefore the singularity at $r^* = 0$ is not an issue in the analysis. The flow domain is represented in figure 1.

Small-intensity free-stream vortical perturbations are passively advected by the uniform free-stream flow and are modeled as three-dimensional vortical disturbances of the gust type, which, sufficiently upstream and away from the plate, have the form

$$\mathbf{u} - \mathbf{i} = \epsilon \hat{\mathbf{u}}^\infty \, e^{i\left(\mathbf{k}\cdot\mathbf{x} - k_x \mathtt{R} \hat{t}\right)} + \text{c.c.}, \tag{2.1}$$

where c.c. indicates the complex conjugate, ϵ is a small parameter, $\mathbf{i}$ is the unit vector along the streamwise direction, and $\hat{t}$ is the dimensionless time defined below. The wavenumber vector $\mathbf{k} = \{k_x, k_y, k_z\}$ and the amplitude of the free-stream velocity disturbance $\hat{\mathbf{u}}^\infty = \{\hat{u}^\infty, \hat{v}^\infty, \hat{w}^\infty\}$ satisfy the solenoidal condition $\mathbf{k}\cdot\hat{\mathbf{u}}^\infty = 0$. Lengths are scaled by $\Lambda^*_z = \lambda^*_z/2\pi$, where λ^*_z is the spanwise wavelength of the gust. As the flow is periodic along the spanwise direction and the boundary-layer dynamics is linear because the perturbation is assumed of small amplitude, λ^*_z is also the spanwise wavelength of the Görtler vortices. This is supported by laboratory evidence as experiments in both incompressible and compressible boundary layers over concave plates have reported a constant spanwise length scale of the vortices (Tani 1962; De Luca *et al.* 1993; Ciolkosz & Spina 2006). Velocities are scaled by U^*_∞, the temperature is scaled by T^*_∞, and the pressure is scaled by $\rho^*_\infty {U^*_\infty}^2$, where ρ^*_∞ is the mean density of air in the free stream.

The Reynolds number is defined as $\mathtt{R} = U^*_\infty \Lambda^*_z/\nu^*_\infty \gg 1$, where ν^*_∞ is the kinematic viscosity of air in the free stream, the Görtler number is $\mathtt{G} = \mathtt{R}^2 \Lambda^*_z/r^* = \mathcal{O}(1)$, and the Mach number is defined as $\mathtt{M} = U^*_\infty/a^*_\infty = \mathcal{O}(1)$, where $a^*_\infty = (\gamma \mathcal{R}^* T^*_\infty)^{1/2}$ is the speed of sound in the free stream, $\mathcal{R}^* = 287.06$ J kg^{-1} K^{-1} is the ideal gas constant for air, and $\gamma = 1.4$ is the ratio of specific heats. The dimensionless spanwise wavenumber is $k_z = 1$

and the frequency parameter is $k_x\mathtt{R} = 2\pi\Lambda_z^{*2}U_\infty^*/(\lambda_x^*\nu_\infty^*)$. The streamwise coordinate and time are scaled as $\hat{x} = x^*/(\mathtt{R}\Lambda_z^*)$ and $\hat{t} = U_\infty^* t^*/(\mathtt{R}\Lambda_z^*)$, respectively, due to our interest in streamwise elongated perturbations. The streamwise scaling used in Ricco & Wu (2007) could have been implemented, i.e., $\bar{x} = k_x x$, but we would have not been able to investigate the steady perturbations $k_x = 0$ as in Wu *et al.* (2011).

Ricco & Wu (2007) proved that, for certain flow conditions defined by the parameter $\kappa = k_z/(k_x\mathtt{R})^{1/2}$, the spanwise pressure gradient of the disturbance couples with the boundary-layer vortical disturbances to generate highly oblique Tollmein-Schlichting waves at sufficiently large streamwise locations $\hat{x}_c$. For $\mathtt{M} = 3$, this instability appears when $0 < \kappa < 0.03$. As the Mach number decreases, the neutral point $\hat{x}_c$ moves downstream and if $\mathtt{M} < 0.8$ the $\hat{x}_c$ location is too far downstream to be physically relevant. In our study we restrict ourselves to cases for which $\kappa > 0.15$, a value that comes from our choice of experimental parameters given in §4, and therefore the highly-oblique Tollmein-Schlichting waves investigated by Ricco & Wu (2007) do not occur.

2.1. *Flow decomposition*

The boundary-layer velocity, pressure, and temperature $\mathbf{q} = \{u, v, w, p, \tau\}$ are decomposed into their mean $\mathbf{Q}$ and perturbation $\acute{\mathbf{q}}$ as

$$\mathbf{q}(\mathbf{x}, t) = \mathbf{Q}(\mathbf{x}) + \epsilon\,\acute{\mathbf{q}}(\mathbf{x}, t). \tag{2.2}$$

Under the assumption $r \gg 1$, curvature effects on the mean flow can be neglected (Spall & Malik 1989) and, consequently, at leading order the mean flow behaves as if the plate were flat. Neither a mean streamwise pressure gradient nor a mean spanwise pressure gradient is present. The Dorodnitsyn-Howarth transformation can then be applied to obtain the mean-flow momentum equation $\mathcal{M}$ and the energy equation $\mathcal{E}$ in similarity form (Stewartson 1964),

$$\mathcal{M}\rceil \quad \left(\frac{\mu F''}{T}\right)' + FF'' = 0, \tag{2.3}$$

$$\mathcal{E}\rfloor \quad \left(\frac{\mu T'}{\mathtt{Pr}T}\right)' + \mathtt{M}^2(\gamma - 1)\frac{\mu F''^2}{T} + FT' = 0, \tag{2.4}$$

where we have introduced the compressible Blasius function $F = F(\eta)$, the temperature $T = T(\eta)$, and the dynamic viscosity $\mu(T) = T^\omega$, where $\omega = 0.76$ (Stewartson 1964). The prime $'$ indicates the derivative with respect to the independent similarity variable $\eta = \bar{Y}/(2\hat{x})^{1/2}$, where $\bar{Y}(\hat{x}, y) = \int_0^y 1/T(\hat{x}, \bar{y})\mathrm{d}\bar{y}$. The Prandtl number, assumed to be constant, is $\mathtt{Pr} = 0.707$. The boundary conditions for (2.3) and (2.4) are

$$\eta = 0\rceil \quad F = F' = 0, \qquad T' = 0, \tag{2.5}$$

$$\eta \to \infty\rfloor \quad F' \to 1, \qquad T \to 1. \tag{2.6}$$

The streamwise velocity U and the wall-normal velocity V of the mean flow are

$$U = F', \qquad V = \frac{T(\eta_c F' - F)}{\mathtt{R}(2\hat{x})^{1/2}}, \tag{2.7}$$

where $\eta_c(\eta) = T^{-1}\int_0^\eta T(\hat{\eta})\mathrm{d}\hat{\eta}$ (Stewartson 1964). The wall-normal mean velocity V can only be approximated by (2.7) in specific ranges of η and $\hat{x}$, as discussed in Appendix B.

2.2. *The compressible boundary-region equations with curvature effects*

The theoretical framework used herein is a combination of the work of Wu *et al.* (2011) on incompressible Görtler flows over concave surfaces with the work of Ricco & Wu (2007) on compressible Klebanoff modes over flat surfaces. Both papers are extensions of the original theory developed by Leib *et al.* (1999) for the incompressible flat-plate case.

Before introducing the boundary-region equations it is instructive to discuss the different asymptotic flow regions, represented in figure 1. The flow domain is divided in five main regions: region FS (free stream) for which $x^2 + y^2 \gg 1$, and regions I, II, III, and IV. Goldstein (1978) developed an analytic framework for the description of the free-stream vortical disturbances in region I. Here, the external disturbances are described as a superposition of inviscid harmonic vortical disturbances which, in the limit $\epsilon \ll 1$, can be analyzed separately due to the linearity of the problem. As the free-stream vortical disturbances evolve further downstream, the outer flow enters region IV where the mean flow is still inviscid. Here, the displacement effect caused by the boundary-layer growth and the energy decay due to viscous dissipation are analytically treated (Leib *et al.* 1999). The dynamics of the flow disturbance in these outer regions causes the origin and growth of the perturbation in the viscous regions II and III inside the boundary layer. The method of matched asymptotic expansion is used to link the outer regions I and IV with the boundary-layer regions II and III. Region II is governed by the linearized unsteady boundary-layer equations, i.e., the linearized unsteady boundary-region (LUBR) equations with the spanwise diffusion and normal pressure gradient terms neglected. Originally introduced by Kemp (1951), the LUBR equations are the full Navier-Stokes and continuity equations with the terms pertaining to the streamwise viscous diffusion and the streamwise pressure gradient neglected. This is a rigorous simplification that follows directly from the assumptions $\mathtt{R} \to \infty$ and $k_x \to 0$. Gulyaev *et al.* (1989), Choudhari (1996), and Leib *et al.* (1999) recognized that the linearized unsteady boundary-layer equations are only appropriate in a small region near the leading edge where the spanwise wavelength λ_z^* is much larger than the boundary-layer thickness $\delta^* = \mathcal{O}((x^*\nu_\infty^*/U_\infty^*)^{1/2})$. As the boundary layer grows to a thickness comparable with the spanwise wavelength, i.e., $\delta^* = \mathcal{O}(\lambda_z^*)$, the spanwise diffusion terms become of the same order of the wall-normal diffusion terms. This occurs in region III, where the Klebanoff modes in the flat-plate case and the Görtler vortices for flows over concave surfaces are fully developed. The LUBR equations, complemented by rigorous initial and free-stream boundary conditions, must therefore be used to study the flow in region III. The boundary-layer perturbations are assumed to be periodic in time t and along the spanwise direction z. They are expressed as in Gulyaev *et al.* (1989),

$$\acute{\mathbf{q}}(\mathbf{x},t) = ik_z\breve{w}\left\{\mathtt{R}\bar{u},\ (2\hat{x})^{1/2}\bar{v},\ \frac{1}{ik_z}\bar{w},\ \frac{1}{\mathtt{R}}\bar{p},\ \mathtt{R}\bar{\tau}\right\} e^{i\left(k_z z - k_x \mathtt{R}\hat{t}\right)} + \text{c.c.}, \tag{2.8}$$

where $\breve{w} \equiv \hat{w}^\infty + ik_z\hat{v}^\infty(k_x^2+k_z^2)^{-1/2}$ and $\bar{\mathbf{q}}(\hat{x},\eta) = \{\bar{u},\bar{v},\bar{w},\bar{p},\bar{\tau}\}(\hat{x},\eta)$.

The full compressible continuity and Navier-Stokes equations in curvilinear coordinates are first simplified using the Lamé coefficients. The mean flow (2.7) and the perturbation flow (2.8) are then introduced into the equations and, taking the limits $\mathtt{R} \to \infty$ and $k_x \to 0$ with $k_x\mathtt{R} = \mathcal{O}(1)$, the LUBR equations are obtained:

$$\mathcal{C}\rceil\ \ \frac{\eta_c}{2\hat{x}}\frac{T'}{T}\bar{u} + \frac{\partial\bar{u}}{\partial\hat{x}} - \frac{\eta_c}{2\hat{x}}\frac{\partial\bar{u}}{\partial\eta} - \frac{T'}{T^2}\bar{v} + \frac{1}{T}\frac{\partial\bar{v}}{\partial\eta} + \bar{w} + \left(ik_x\mathtt{R}\frac{1}{T} - \frac{1}{2\hat{x}}\frac{FT'}{T^2}\right)\bar{\tau} - \frac{F'}{T}\frac{\partial\bar{\tau}}{\partial\hat{x}} +$$

$$\frac{1}{2\hat{x}}\frac{F}{T}\frac{\partial\bar{\tau}}{\partial\eta} = 0, \tag{2.9}$$

$$\mathcal{X}| \quad \left(-ik_x\mathtt{R} - \frac{\eta_c}{2\hat{x}}F'' + k_z^2\mu T\right)\bar{u} + F'\frac{\partial \bar{u}}{\partial \hat{x}} - \frac{1}{2\hat{x}}\left(F + \frac{\mu' T'}{T} - \frac{\mu T'}{T^2}\right)\frac{\partial \bar{u}}{\partial \eta} - \frac{1}{2\hat{x}}\frac{\mu}{T}\frac{\partial^2 \bar{u}}{\partial \eta^2} +$$

$$\frac{F''}{T}\bar{v} + \frac{1}{2\hat{x}T}\left(FF'' - \mu'' F'' T' + \frac{\mu' F'' T'}{T} - \mu' F'''\right)\bar{\tau} - \frac{1}{2\hat{x}}\frac{\mu' F''}{T}\frac{\partial \bar{\tau}}{\partial \eta} = 0, \qquad (2.10)$$

$$\mathcal{Y}| \quad \frac{1}{4\hat{x}^2}\left[\eta_c\left(FT' - F'T\right) - \eta_c^2 F'' T + FT\right]\bar{u} + \frac{\mu' T'}{3\hat{x}}\frac{\partial \bar{u}}{\partial \hat{x}} - \frac{\mu}{6\hat{x}}\frac{\partial^2 \bar{u}}{\partial \hat{x}\partial \eta} + \frac{\eta_c \mu}{12\hat{x}^2}\frac{\partial^2 \bar{u}}{\partial \eta^2} +$$

$$\frac{1}{12\hat{x}^2}\left(\eta_c\mu' T' + \mu - \frac{\eta_c \mu T'}{T}\right)\frac{\partial \bar{u}}{\partial \eta} + \left[\frac{1}{2\hat{x}}\left(F' + \eta_c F'' - \frac{FT'}{T}\right) - ik_x\mathtt{R} + k_z^2\mu T\right]\bar{v} +$$

$$F'\frac{\partial \bar{v}}{\partial \hat{x}} + \frac{1}{\hat{x}}\left[\frac{2}{3T}\left(\frac{\mu T'}{T} - \mu' T'\right) - \frac{F}{2}\right]\frac{\partial \bar{v}}{\partial \eta} - \frac{2}{3\hat{x}}\frac{\mu}{T}\frac{\partial^2 \bar{v}}{\partial \eta^2} + \frac{\mu' T'}{3\hat{x}}\bar{w} - \frac{\mu}{6\hat{x}}\frac{\partial \bar{w}}{\partial \eta} + \frac{1}{2\hat{x}}\frac{\partial \bar{p}}{\partial \eta} +$$

$$\left[\frac{1}{3\hat{x}^2 T}\left(\mu'' F T'^2 - \frac{\mu' F T'^2}{T} + \mu' F T'' + \mu' F' T'\right) - \frac{1}{4\hat{x}^2}\left(F'F - \eta_c F'^2 - \eta_c F F'' +\right.\right.$$

$$\left.\left.\frac{F^2 T'}{T} + \mu' F'' + \eta_c \mu'' F'' T' - \frac{\eta_c \mu' F'' T'}{T} + \eta_c F''' \mu'\right)\right]\bar{\tau} + \frac{\mu'}{\hat{x}^2}\left(\frac{FT'}{3T} - \frac{\eta_c F''}{4}\right)\frac{\partial \bar{\tau}}{\partial \eta} -$$

$$\frac{\mu' F''}{2\hat{x}}\frac{\partial \bar{\tau}}{\partial \hat{x}} + \boxed{\frac{\mathtt{G}}{(2\hat{x})^{1/2}}\left(2F'\bar{u} - \frac{F'^2}{T}\bar{\tau}\right)} = 0, \qquad (2.11)$$

$$\mathcal{Z}| \quad -\frac{k_z^2 \eta_c \mu' T T'}{2\hat{x}}\bar{u} + \frac{k_z^2 \mu T}{3}\frac{\partial \bar{u}}{\partial \hat{x}} - \frac{k_z^2 \eta_c \mu T}{6\hat{x}}\frac{\partial \bar{u}}{\partial \eta} + k_z^2 \mu' T' \bar{v} + \frac{k_z^2 \mu}{3}\frac{\partial \bar{v}}{\partial \eta} +$$

$$\left(\frac{4}{3}k_z^2 \mu T - ik_x\mathtt{R}\right)\bar{w} + F'\frac{\partial \bar{w}}{\partial \hat{x}} + \frac{1}{2\hat{x}}\left(\frac{\mu T'}{T^2} - F - \frac{\mu' T'}{T}\right)\frac{\partial \bar{w}}{\partial \eta} - \frac{1}{2\hat{x}}\frac{\mu}{T}\frac{\partial^2 \bar{w}}{\partial \eta^2} -$$

$$k_z^2 T\bar{p} + \frac{k_z^2}{3\hat{x}}\mu' F T' \bar{\tau} = 0, \qquad (2.12)$$

$$\mathcal{E}| \quad -\frac{\eta_c}{2\hat{x}}T'\bar{u} + \frac{T'}{T}\bar{v} + \left[\frac{FT'}{2\hat{x}T} - ik_x\mathtt{R} + \frac{k_z^2 \mu T}{\mathtt{Pr}} - \frac{1}{2\hat{x}\mathtt{Pr}}\frac{\partial}{\partial \eta}\left(\frac{\mu' T'}{T}\right)\right]\bar{\tau} + F'\frac{\partial \bar{\tau}}{\partial \hat{x}} +$$

$$\frac{1}{2\hat{x}}\left(\frac{\mu T'}{\mathtt{Pr}T^2} - F - \frac{2\mu' T'}{\mathtt{Pr}T}\right)\frac{\partial \bar{\tau}}{\partial \eta} - \frac{1}{2\hat{x}\mathtt{Pr}}\frac{\mu}{T}\frac{\partial^2 \bar{\tau}}{\partial \eta^2} - \mathtt{M}^2\frac{\gamma - 1}{\hat{x}T}\left(\mu F''\frac{\partial \bar{u}}{\partial \eta} + \frac{\mu' F''^2}{2}\bar{\tau}\right) = 0, \qquad (2.13)$$

where $\mathcal{C}$, $\mathcal{X}$, $\mathcal{Y}$, $\mathcal{Z}$, $\mathcal{E}$ indicate the continuity, x-momentum, y-momentum, z-momentum, and energy equations. The prime $'$ represents differentiation with respect to the independent variable. The equations of Ricco & Wu (2007) for the compressible flow over a flat surface and of Wu *et al.* (2011) for the incompressible flow over a concave surface are recovered by setting $\mathtt{G} = 0$ and $\mathtt{M} = 0$, respectively. Curvature effects derive from the centrifugal force and only appear in the convective terms of the $\mathcal{Y}$ equation (2.11). These terms, boxed in (2.11), are proportional to the Görtler number $\mathtt{G}$ and, in the compressible case, also include the temperature perturbation (El-Hady & Verma 1983; Hall & Malik 1989). The LUBR equations are parabolic along the streamwise direction and are influenced by $\mathtt{G}$, k_y, $k_x\mathtt{R}$, and $\mathtt{M}$, which account for the effects of curvature, ratio of the free-stream spanwise wavelength to the wall-normal wavelength, frequency, and compressibility, respectively.

The streamwise velocity $\bar{u}$ and the temperature perturbation $\bar{\tau}$ inside the boundary layer tend to zero as the free stream is approached because they amplify inside the boundary layer to an order of magnitude larger than the corresponding free-stream disturbances (Ricco & Wu 2007). Therefore, the boxed curvature terms in (2.11) can be neglected as $\eta \to \infty$ and we recover the free-stream boundary conditions used by Ricco & Wu (2007):

$$\eta = 0\rceil \quad \bar{u} = \bar{v} = \bar{w} = \frac{\partial \bar{\tau}}{\partial \eta} = 0, \tag{2.14}$$

$$\eta \to \infty\rfloor \quad \bar{u} \to 0, \tag{2.15}$$

$$\frac{\partial \bar{v}}{\partial \eta} + |k_z|(2\hat{x})^{1/2}\bar{v} \to -e^{i[k_x \mathrm{R}\hat{x} + k_y(2\hat{x})^{1/2}(\eta-\beta_c)] - \left(k_y^2+k_z^2\right)\hat{x}}, \tag{2.16}$$

$$\frac{\partial \bar{w}}{\partial \eta} + |k_z|(2\hat{x})^{1/2}\bar{w} \to ik_y(2\hat{x})^{1/2} e^{i[k_x \mathrm{R}\hat{x} + k_y(2\hat{x})^{1/2}(\eta-\beta_c)] - \left(k_y^2+k_z^2\right)\hat{x}}, \tag{2.17}$$

$$\frac{\partial \bar{p}}{\partial \eta} + |k_z|(2\hat{x})^{1/2}\bar{p} \to 0, \tag{2.18}$$

$$\bar{\tau} \to 0, \tag{2.19}$$

where compressibility effects are taken into account by the parameter $\beta_c(\mathtt{M}) \equiv \lim_{\eta\to\infty}(\eta - F)$, which is computed numerically (Ricco *et al.* 2009). Since curvature effects are also negligible in the limit $\hat{x} \to 0$, the initial conditions of Ricco & Wu (2007) apply:

$$\hat{x} \to 0\rceil \quad \bar{u} \to 2\hat{x}U_0 + (2\hat{x})^{3/2}U_1, \tag{2.20}$$

$$\bar{v} \to V_0 + (2\hat{x})^{1/2}V_1 - \left[V_c - \frac{1}{2}g_1|k_z|(2\hat{x})^{1/2}\right] e^{-|k_z|(2\hat{x})^{1/2}\bar{\eta}} + \frac{i}{(k_y - i|k_z|)(2\hat{x})^{1/2}}\left[e^{ik_y(2\hat{x})^{1/2}\bar{\eta} - \left(k_y^2+k_z^2\right)\hat{x}} - e^{-|k_z|(2\hat{x})^{1/2}\bar{\eta}}\right] - \bar{v}_c, \tag{2.21}$$

$$\bar{w} \to W_0 + (2\hat{x})^{1/2}W_1 - V_c|k_z|(2\hat{x})^{1/2}e^{-|k_z|(2\hat{x})^{1/2}\bar{\eta}} + \frac{1}{k_y - i|k_z|}\left[k_y e^{ik_y(2\hat{x})^{1/2}\bar{\eta} - \left(k_y^2+k_z^2\right)\hat{x}} - i|k_z|e^{-|k_z|(2\hat{x})^{1/2}\bar{\eta}}\right] - \bar{w}_c, \tag{2.22}$$

$$\bar{p} \to \frac{P_0}{(2\hat{x})^{1/2}} + P_1 + \left[g_1 - \frac{V_c}{|k_z|(2\hat{x})^{1/2}}\right] e^{-|k_z|(2\hat{x})^{1/2}\bar{\eta}} - \bar{p}_c, \tag{2.23}$$

$$\bar{\tau} \to 2\hat{x}T_0 + (2\hat{x})^{3/2}T_1, \tag{2.24}$$

where $\bar{\eta} \equiv \eta - \beta_c$. Appendix B further discusses the ranges of validity of the outer boundary conditions (2.15)-(2.19) and of the initial conditions (2.20)-(2.24) in terms of η and $\hat{x}$. The common parts $\bar{v}_c$, $\bar{w}_c$, and $\bar{p}_c$, the constants g_1 and V_c, and the solutions $U_0, V_0, W_0, P_0, T_0, U_1, V_1, W_1, P_1, T_1$ are derived in Appendix C. The numerical procedure for solving the LUBR equations is described in Appendix A. To stress the importance of receptivity, we note that the solution is influenced by k_y only through the initial and boundary conditions as k_y does not appear in the LUBR equations (2.9)-(2.13).

2.3. *The eigenvalue equations with curvature effects*

Because of the inviscid unbalance between the centrifugal force and the wall-normal pressure, the Görtler instability exhibits an exponential streamwise amplification. Following the work of Wu *et al.* (2011), we can take advantage of this property by adopting a simplified mathematical framework based on an additional decomposition of the quantities defined in (2.8),

$$\bar{\mathbf{q}}(\hat{x},\eta) = \{\bar{u},\bar{v},\bar{w},\bar{p},\bar{\tau}\} \equiv \widetilde{\mathbf{q}}(\eta)\, e^{\int^{\hat{x}} \sigma_{\text{EV}}(x)\mathrm{d}x}, \tag{2.25}$$

where $\widetilde{\mathbf{q}} = \{\widetilde{u},\widetilde{v},\widetilde{w},\widetilde{p},\widetilde{\tau}\}$ and $\sigma_{\text{EV}} = \sigma_{\text{EV, Re}} + i\sigma_{\text{EV, Im}}$ is a complex function whose real part $\sigma_{\text{EV, Re}}(\hat{x})$ is the local growth rate and the imaginary part $\sigma_{\text{EV, Im}}(\hat{x})$ is proportional to the streamwise wavenumber of the boundary-layer perturbation, i.e.,

$$k_{x,\,\text{EV}}(\hat{x}) = \frac{1}{\hat{x}}\int^{\hat{x}} \sigma_{\text{EV}}(x)\mathrm{d}x. \tag{2.26}$$

Expression (2.25) is a local eigenvalue (EV) decomposition, i.e., valid at a specified streamwise location, which implies that the streamwise dependence of the perturbation is absorbed in $\sigma(\hat{x})$, while the wall-normal variation is distilled in $\widetilde{\mathbf{q}}(\eta)$. The EV perturbation (2.25) is only defined within an undetermined amplitude that can only be found through the receptivity analysis, i.e., by accounting for the influence of the free-stream disturbance. Nevertheless, upon comparison with the LUBR solution, the EV approach identifies the streamwise locations where the perturbation exhibits exponential growth and where its growth rate and streamwise length scale are not influenced by the initial and free-stream boundary conditions.

By substituting (2.25) into (2.9)-(2.13) we obtain the non-parallel EV system of equations, which preserves the growing nature of the boundary-layer mean flow. The equations can be further simplified by invoking the η-based parallel mean-flow assumption, which implies $V = 0$, and by taking the limit $\hat{x} \gg 1$ (Wu *et al.* 2011). For numerical reasons, the system of ordinary differential equations is written as a system of first order equations by introducing three new variables,

$$\widetilde{f}(\eta) \equiv \frac{\partial\widetilde{u}}{\partial\eta}, \qquad \widetilde{g}(\eta) \equiv \frac{\partial\widetilde{w}}{\partial\eta}, \qquad \widetilde{h}(\eta) \equiv \frac{\partial\widetilde{\tau}}{\partial\eta}. \tag{2.27}$$

The non-parallel compressible EV equations are given in the following, where the terms between $\langle\,\rangle$ can be neglected under the parallel flow assumption because they arise from the wall-normal velocity V given in (2.7).

$$\mathcal{C}\rceil\ \ \frac{\partial\widetilde{v}}{\partial\eta} = (\sigma F' - ik_x\mathtt{R})\,\widetilde{\tau} - \sigma T\widetilde{u} + \widetilde{v}\frac{T'}{T} - T\widetilde{w} + \left\langle \frac{FT'}{2\hat{x}T}\widetilde{\tau} - \frac{\eta_c}{2\hat{x}}T'\widetilde{u} - \frac{F}{2\hat{x}}\widetilde{h} + \frac{\eta_c T}{2\hat{x}}\widetilde{f} \right\rangle, \tag{2.28}$$

$$\mathcal{X}|\ \ \frac{\partial\widetilde{f}}{\partial\eta} = \left(-ik_x\mathtt{R}\frac{2\hat{x}T}{\mu} + 2\hat{x}\sigma\frac{F'T}{\mu} + 2\hat{x}k_z^2T^2\right)\widetilde{u} - \frac{F''\mu'}{\mu}\widetilde{h} + \frac{2\hat{x}F''}{\mu}\widetilde{v} - \left(\frac{\mu'T'}{\mu} - \frac{T'}{T}\right)\widetilde{f} +$$
$$\left(\frac{\mu'F''T'}{\mu T} - \frac{\mu''F''T'}{\mu} - \frac{\mu'F'''}{\mu}\right)\widetilde{\tau} + \left\langle \frac{FF''}{\mu}\widetilde{\tau} - \frac{\eta_c F''T}{\mu}\widetilde{u} - \frac{FT}{\mu}\widetilde{f} \right\rangle, \tag{2.29}$$

$$\mathcal{Y}| \quad \frac{\partial\widetilde{p}}{\partial\eta} = -\sigma\mu\widetilde{f} - 2\sigma T'\left(\mu' + \frac{2}{3}\frac{\mu}{T}\right)\widetilde{u} + 2\hat{x}\left(ik_x\mathtt{R} - k_z^2\mu T - \sigma F'\right)\widetilde{v} - \mu\widetilde{g} + \left(F''\mu'\sigma + \frac{4}{3}\frac{\mu'T'F'\sigma}{T} - \frac{4}{3}\frac{\mu F''\sigma}{T} - \frac{4}{3}ik_x\mathtt{R}\frac{\mu'T'}{T}\right)\widetilde{\tau} + \frac{4}{3}\frac{\mu}{T}\left(\sigma F' - ik_x\mathtt{R}\right)\widetilde{h} - 2T'\left(\mu'+\frac{2}{3}\frac{\mu}{T}\right)\widetilde{w} + (2\hat{x})^{1/2}\mathtt{G}F'\left(\frac{F'}{T}\widetilde{\tau} - 2\widetilde{u}\right) + \left\langle \frac{\mu}{2\hat{x}}\widetilde{f} + \left(-ik_x\mathtt{R}\eta_c T + \sigma\eta_c F'T + k_z^2\eta_c\mu T^2 - \frac{2\eta_c}{3\hat{x}}\frac{\mu'T'^2}{T} + \frac{2\eta_c}{3\hat{x}}\frac{\mu T'^2}{T^2} - \frac{2}{3\hat{x}}\frac{\mu T'}{T} - \frac{2\eta_c}{3\hat{x}}\frac{\mu T''}{T} + \frac{\eta_c}{2\hat{x}}F'T - \frac{FT}{2\hat{x}} - \frac{\eta_c FT'}{\hat{x}} - \sigma FT\right)\widetilde{u} + \left(\frac{4}{3}\frac{\mu'T'^2}{T^2} - \frac{4}{3}\frac{\mu T'^2}{T^3} + \frac{4}{3}\frac{\mu T''}{T^2} - F' + 2\frac{FT'}{T}\right)\widetilde{v} + \left(\frac{\mu'F''}{2\hat{x}} - \frac{2}{3\hat{x}}\frac{\mu''FT'^2}{T} + \frac{4}{3\hat{x}}\frac{\mu'FT'^2}{T^2} - \frac{2}{3\hat{x}}\frac{\mu'FT''}{T} - \frac{2}{3\hat{x}}\frac{\mu'F'T'}{T} - \frac{2}{3\hat{x}}\frac{\mu FT'^2}{T^3} + \frac{2}{3\hat{x}}\frac{\mu F'T'}{T^2} + \frac{2}{3\hat{x}}\frac{\mu FT''}{T^2} - ik_x\mathtt{R}F + \sigma FF' + \frac{FF'}{2\hat{x}} + \frac{1}{2\hat{x}}\frac{2F^2T'}{T} - \frac{\eta_c F'^2}{2\hat{x}}\right)\widetilde{\tau} + \left(\frac{2}{3\hat{x}}\frac{\mu FT'}{T^2} - \frac{4}{3\hat{x}}\frac{\mu'FT'}{T} - \frac{2}{3\hat{x}}\frac{\mu F'}{T} - \frac{F^2}{2\hat{x}}\right)\widetilde{h} - FT\widetilde{w} - \frac{2}{3\hat{x}}\frac{\mu F}{T}\frac{\partial\widetilde{h}}{\partial\eta}\right\rangle, \tag{2.30}$$

$$\mathcal{Z}| \quad \frac{\partial\widetilde{g}}{\partial\eta} = 2\hat{x}\left(-\frac{ik_x\mathtt{R}T}{\mu} + \frac{\sigma F'T}{\mu} + k_z^2T^2\right)\widetilde{w} + \left(-\frac{\mu'T'}{\mu} + \frac{T'}{T}\right)\widetilde{g} - \frac{2\hat{x}k_z^2T^2}{\mu}\widetilde{p} + 2\hat{x}k_z^2\left(\frac{\mu'T'T}{\mu} + \frac{T'}{3}\right)\widetilde{v} + \frac{2\hat{x}k_z^2}{3}T\left(-ik_x\mathtt{R} + F'\sigma\right)\widetilde{\tau} + \left\langle \frac{FT'}{3}\left(1 + \frac{2\mu'T}{\mu}\right)\widetilde{\tau} - \frac{FT}{\mu}\widetilde{g} - k_z^2\eta_c T'T\left(\frac{\mu'T}{\mu} + \frac{1}{3}\right)\widetilde{u} - \frac{k_z^2FT}{3}\widetilde{h}\right\rangle, \tag{2.31}$$

$$\mathcal{E}\rfloor \quad \frac{\partial\widetilde{h}}{\partial\eta} = T'\left(-\frac{2\mu'}{\mu} + \frac{1}{T}\right)\widetilde{h} + \frac{2\hat{x}\mathtt{Pr}T'}{\mu}\widetilde{v} - 2(\gamma-1)\mathtt{M}^2\mathtt{Pr}F''\widetilde{f} + 2\hat{x}T\left(-\frac{ik_x\mathtt{RPr}}{\mu} + \frac{\sigma\mathtt{Pr}F'}{\mu} + k_z^2T\right)\widetilde{\tau} + \left\langle \frac{1}{\mu}\left[\mathtt{Pr}FT' - (\gamma-1)\mathtt{M}^2\mathtt{Pr}\mu'F''^2 - T\frac{\partial}{\partial\eta}\left(\frac{\mu'T'}{T}\right)\right]\widetilde{\tau} - \frac{\eta_c\mathtt{Pr}T'T}{\mu}\widetilde{u} - \frac{\mathtt{Pr}FT}{\mu}\widetilde{h}\right\rangle. \tag{2.32}$$

The EV system (2.28)-(2.32) is solved with homogeneous boundary conditions: $\widetilde{u} = \widetilde{v} = \widetilde{w} = \widetilde{\tau} = 0$ at $\eta = 0$ and $\widetilde{u}, \widetilde{v}, \widetilde{w}, \widetilde{\tau} \to 0$ as $\eta \to \infty$. For $\mathtt{M} = 0$, the equations of Wu *et al.* (2011) for the incompressible case are recovered. The numerical procedure for solving the EV equations is described in Appendix A.

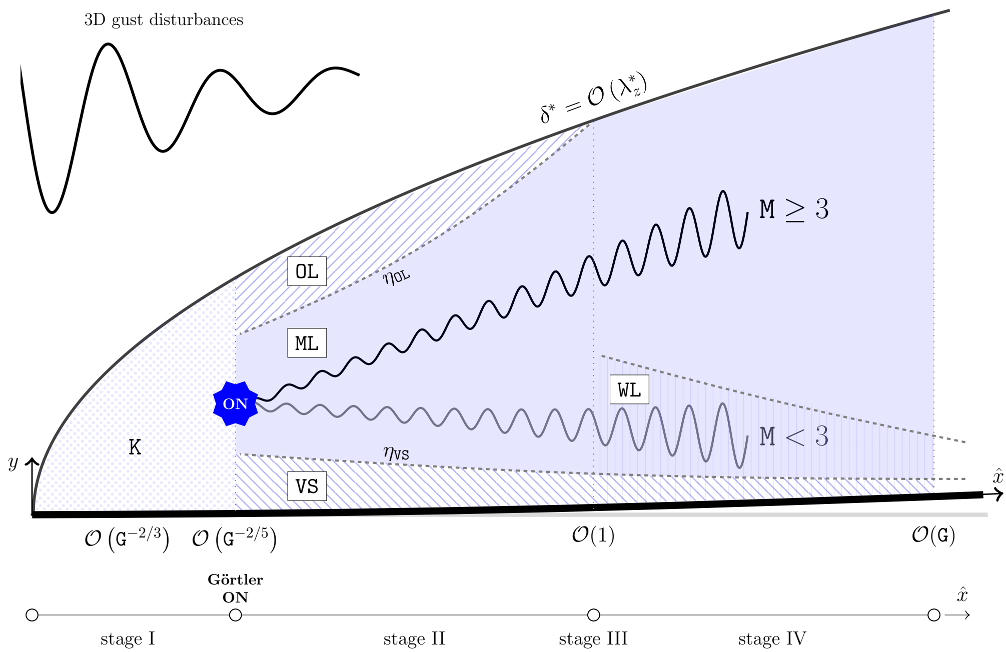

Figure 2: Sketch of the boundary-layer asymptotic stages for $\mathtt{G} \to \infty$: Klebanoff modes $\mathtt{K}$, main layer $\mathtt{ML}$, viscous sublayer $\mathtt{VS}$, outer layer $\mathtt{OL}$, and wall layer $\mathtt{WL}$.

3. Theoretical results

In most experiments where flows over concave surfaces have been investigated in incompressible and compressible conditions, the Görtler number has been larger than 10^2. This motivated Wu *et al.* (2011) to study the asymptotic limit $\mathtt{G} \to \infty$ that revealed the necessary conditions for the inviscid instability and the different stages of the evolution of the incompressible Görtler vortices. We herein extend the analysis of Wu *et al.* (2011) to the compressible case with $\mathtt{M} = \mathcal{O}(1)$. A summary of the physical results extracted through the asymptotic analysis of this section is given in §3.5 on page 25. Even though this theoretical analysis unveils crucial physical characteristics that are not revealed by a purely numerical approach, it will become evident that the numerical solution of the LUBR equations is nevertheless needed for a thorough understanding and an accurate computation of the flow, especially for $\mathtt{G} = \mathcal{O}(1)$, where the asymptotic analysis is invalid.

Figure 2 shows the different streamwise stages through which the perturbation evolves in the limit $\mathtt{G} \gg 1$. In this limit we can identify four main layers, namely the main layer $\mathtt{ML}$, the outer layer $\mathtt{OL}$, the viscous sublayer $\mathtt{VS}$, and the wall layer $\mathtt{WL}$.

3.1. *Stage I. Pre-modal regime: $\hat{x} \leqslant \mathtt{G}^{-2/5}$*

We first consider the region in the proximity of the leading edge, i.e., $\hat{x} \ll 1$, where the power-series expansion (C 7) is valid. By assuming that $\bar{w} = \mathcal{O}(1)$, $\eta = \mathcal{O}(1)$, $\eta_c = \mathcal{O}(1)$, and $T, T', F, F' = \mathcal{O}(1)$, an order of magnitude analysis of the terms in the $\mathcal{C}$ equation (2.9) leads to

$$\bar{u} = \mathcal{O}(\hat{x}), \qquad \bar{\tau} = \mathcal{O}(\hat{x}), \qquad \bar{v} = \mathcal{O}(1). \tag{3.1}$$

The terms of the $\mathcal{Y}$ equation (2.11) become of order

$$\underbrace{\mathcal{O}(1)}_{\text{unsteadiness}} \quad + \underbrace{\mathcal{O}\left(\frac{1}{\hat{x}}\right)}_{\text{inertia}} + \underbrace{\mathcal{O}\left(\hat{x}^{1/2}\mathtt{G}\right)}_{\text{curvature}} = \underbrace{\frac{P_0'(\eta)}{(2\hat{x})^{3/2}}}_{\eta\ \text{pressure gradient}} \quad + \underbrace{\mathcal{O}\left(\frac{1}{\hat{x}}\right)}_{\text{diffusion}}, \tag{3.2}$$

by using the power-series expansion (C 7) for the pressure. When $\hat{x} \ll \mathtt{G}^{-2/3}$, the equations are steady and the curvature effects are negligible compared to the other terms. Therefore, the perturbation evolves as flat-plate Klebanoff modes, denoted by the letter $\mathtt{K}$ in figure 2, and the wall-normal gradient of the pressure perturbation is negligible because the term dominates as $\hat{x} \ll 1$. Further downstream where $\hat{x} = \mathcal{O}\left(\mathtt{G}^{-2/3}\right)$, curvature effects start to influence the other terms, including the pressure field, rendering the asymptotic series expansion (C 7) invalid. The gradient of the pressure $\overline{p}$ along η grows to an order-one magnitude as it balances the centrifugal term. Substituting the scaled variables

$$x^\dagger = \hat{x}\, \mathtt{G}^{2/3}, \qquad u^\dagger = \bar{u}\, \mathtt{G}^{2/3}, \qquad \tau^\dagger = \bar{\tau}\, \mathtt{G}^{2/3}, \tag{3.3}$$

into (2.9)-(2.13) and neglecting terms $\ll 1$, the perturbation field is described by

$$\mathcal{C}\rceil \;\; \frac{\eta_c}{2x^\dagger}\frac{T'}{T}u^\dagger + \frac{\partial u^\dagger}{\partial x^\dagger} - \frac{\eta_c}{2x^\dagger}\frac{\partial u^\dagger}{\partial \eta} - \frac{T'}{T^2}\bar{v} + \frac{1}{T}\frac{\partial \bar{v}}{\partial \eta} - \frac{FT'}{2x^\dagger T^2}\tau^\dagger - \frac{F'}{T}\frac{\partial \tau^\dagger}{\partial x^\dagger} + \frac{F}{2x^\dagger T}\frac{\partial \tau^\dagger}{\partial \eta} + \bar{w} = 0, \tag{3.4}$$

$$\mathcal{X}| \;\; -\frac{\eta_c}{2x^\dagger}F''u^\dagger + F'\frac{\partial u^\dagger}{\partial x^\dagger} + \frac{1}{2x^\dagger}\left(\frac{\mu T'}{T^2} - F - \frac{\mu' T'}{T}\right)\frac{\partial u^\dagger}{\partial \eta} - \frac{\mu}{2x^\dagger T}\frac{\partial^2 u^\dagger}{\partial \eta^2} + \frac{F''}{T}\bar{v} + \frac{1}{2x^\dagger T}\left(FF'' - \mu'' F'' T' + \frac{\mu' F'' T'}{T} - \mu' F'''\right)\tau^\dagger - \frac{\mu' F''}{2x^\dagger T}\frac{\partial \tau^\dagger}{\partial \eta} = 0, \tag{3.5}$$

$$\mathcal{Z}| \;\; F'\frac{\partial \bar{w}}{\partial x^\dagger} + \frac{1}{2x^\dagger}\left(\frac{\mu T'}{T^2} - F - \frac{\mu' T'}{T}\right)\frac{\partial \bar{w}}{\partial \eta} - \frac{\mu}{2x^\dagger T}\frac{\partial^2 \bar{w}}{\partial \eta^2} = 0, \tag{3.6}$$

$$\mathcal{E}| \;\; -\frac{\eta_c T'}{2x^\dagger}u^\dagger - \mathtt{M}^2\frac{(\gamma-1)}{x^\dagger}\frac{\mu F''}{T}\frac{\partial u^\dagger}{\partial \eta} + \frac{T'}{T}\bar{v} + \frac{1}{2x^\dagger}\left[\frac{FT'}{T} - \mathtt{M}^2(\gamma-1)\frac{\mu' F''^2}{T} - \frac{1}{\mathtt{Pr}}\frac{\partial}{\partial \eta}\left(\frac{\mu' T'}{T}\right)\right]\tau^\dagger + F'\frac{\partial \tau^\dagger}{\partial x^\dagger} + \frac{1}{2x^\dagger}\left(\frac{\mu T'}{\mathtt{Pr}T^2} - F - \frac{2\mu' T'}{\mathtt{Pr}T}\right)\frac{\partial \tau^\dagger}{\partial \eta} - \frac{1}{2x^\dagger \mathtt{Pr}}\frac{\mu}{T}\frac{\partial^2 \tau^\dagger}{\partial \eta^2} = 0. \tag{3.7}$$

It is sufficient to solve $\mathcal{C}$, $\mathcal{X}$, $\mathcal{Z}$, and $\mathcal{E}$ to find the velocity and temperature perturbations. The pressure $\bar{p}$ is solved a posteriori from $\mathcal{Y}$, which reads

$$\mathcal{Y}\rfloor \;\; \frac{1}{(2x^\dagger)^2}\left[FT - \eta_c F' T - \eta_c^2 F'' T + \eta_c F T' + \frac{2F'}{(2x^\dagger)^{1/2}}\right]u^\dagger + \frac{\mu' T'}{3x^\dagger}\frac{\partial u^\dagger}{\partial x^\dagger} - \frac{\mu}{6x^\dagger}\frac{\partial^2 u^\dagger}{\partial \eta \partial x^\dagger} + \frac{\eta_c \mu}{12{x^\dagger}^2}\frac{\partial^2 u^\dagger}{\partial \eta^2} + \frac{1}{12{x^\dagger}^2}\left(\eta_c \mu' T' + \mu - \frac{\eta_c \mu T'}{T}\right)\frac{\partial u^\dagger}{\partial \eta} + \frac{1}{2x^\dagger}\left(F' + \eta_c F'' - \frac{FT'}{T}\right)\bar{v} + F'\frac{\partial \bar{v}}{\partial x^\dagger} + \frac{1}{x^\dagger}\left(\frac{2}{3}\frac{\mu T'}{T^2} - \frac{2}{3}\frac{\mu' T'}{T} - \frac{F}{2}\right)\frac{\partial \bar{v}}{\partial \eta} - \frac{2}{3x^\dagger}\frac{\mu}{T}\frac{\partial^2 \bar{v}}{\partial \eta^2} + \frac{\mu' T'}{3x^\dagger}\bar{w} -$$

$$\frac{\mu}{6x^\dagger}\frac{\partial \bar{w}}{\partial \eta}+\frac{1}{2x^\dagger}\frac{\partial \bar{p}}{\partial \eta}+\left[\frac{1}{(2x^\dagger)^2}\left(\eta_c F'^2-FF'+\eta_c FF''-\frac{F^2T'}{T}-\mu'F''-\eta_c\mu''F''T'+\right.\right.$$

$$\left.\frac{\eta_c\mu'F''T'}{T}-\eta_c\mu'F'''\right)+\frac{1}{3{x^\dagger}^2T}\left(\mu''T'^2F-\frac{\mu'T'^2F}{T}+\mu'T''F+\mu'T'F'\right)-$$

$$\left.\frac{F'^2}{(2x^\dagger)^{1/2}T}\right]\tau^\dagger-\frac{\mu'F''}{2x^\dagger}\frac{\partial\tau^\dagger}{\partial x^\dagger}+\mu'\left[\frac{T'F}{3{x^\dagger}^2T}-\frac{\eta_cF''}{(2x^\dagger)^2}\right]\frac{\partial\tau^\dagger}{\partial\eta}=0. \tag{3.8}$$

Equation (3.8) is decoupled from the other equations since, in the new scaling (3.3), the pressure term in $\mathcal{Z}$ is negligible, so the flow is governed by the boundary-layer equations, i.e., the effects of the spanwise viscous diffusion and of the spanwise pressure gradient are negligible (although the boundary-layer equations may also apply if a mean spanwise pressure gradient is imposed).

As the flow evolves further downstream we seek the location where the curvature effects begin to influence the perturbation velocity also through the pressure gradient along the z direction in the $\mathcal{Z}$ equation (2.12). The pressure has now grown to an unknown order of magnitude. This is found by balancing the curvature and the pressure terms of the $\mathcal{Y}$ equation (2.11) to obtain $\mathtt{G}\hat{x}^{1/2} \sim \bar{p}/\hat{x}$, hence $\bar{p}=\mathcal{O}\left(\mathtt{G}\,\hat{x}^{3/2}\right)$. The terms of the $\mathcal{Z}$ equation (2.12) become of order

$$\underbrace{\mathcal{O}(1)}_{\text{unsteadiness}}+\underbrace{\mathcal{O}\left(\frac{1}{\hat{x}}\right)}_{\text{inertia}}=\underbrace{\mathcal{O}\left(\mathtt{G}\,\hat{x}^{3/2}\right)}_{\eta\text{ pressure gradient}}+\underbrace{\mathcal{O}\left(\frac{1}{\hat{x}}\right)}_{\text{diffusion}}, \tag{3.9}$$

from which it is inferred that the pressure comes into play in the $\mathcal{Z}$ equation when $\hat{x}=\mathcal{O}\left(\mathtt{G}^{-2/5}\right)$. A new scaling can thus be introduced for $\eta=\mathcal{O}(1)$, as follows

$$\breve{x}=\hat{x}\,\mathtt{G}^{2/5},\qquad \breve{u}=\bar{u}\,\mathtt{G}^{2/5},\qquad \breve{\tau}=\bar{\tau}\,\mathtt{G}^{2/5},\qquad \breve{p}=\bar{p}\,\mathtt{G}^{-2/5}. \tag{3.10}$$

After substitution into the LUBR equations (2.9)-(2.13), the equations of motion become

$$\mathcal{C}]\quad \frac{\eta_c}{2\breve{x}}\frac{T'}{T}\breve{u}+\frac{\partial\breve{u}}{\partial\breve{x}}-\frac{\eta_c}{2\breve{x}}\frac{\partial\breve{u}}{\partial\eta}-\frac{T'}{T^2}\bar{v}+\frac{1}{T}\frac{\partial\bar{v}}{\partial\eta}+\bar{w}-\frac{FT'}{2\breve{x}T^2}\breve{\tau}-\frac{F'}{T}\frac{\partial\breve{\tau}}{\partial\breve{x}}+\frac{F}{2\breve{x}T}\frac{\partial\breve{\tau}}{\partial\eta}=0, \tag{3.11}$$

$$\mathcal{X}|\quad -\frac{\eta_cF''}{2\breve{x}}\breve{u}+F'\frac{\partial\breve{u}}{\partial\breve{x}}+\frac{1}{2\breve{x}}\left(\frac{\mu T'}{T^2}-\frac{\mu'T'}{T}-F\right)\frac{\partial\breve{u}}{\partial\eta}-\frac{\mu}{2\breve{x}T}\frac{\partial^2\breve{u}}{\partial\eta^2}+\frac{F''}{T}\bar{v}+$$

$$\frac{1}{2\breve{x}T}\left(FF''-\mu''F''T'+\frac{\mu'F''T'}{T}-\mu'F'''\right)\breve{\tau}-\frac{F''\mu'}{2\breve{x}T}\frac{\partial\breve{\tau}}{\partial\eta}=0 \tag{3.12}$$

$$\mathcal{Y}|\quad \frac{2F'}{(2\breve{x})^{1/2}}\breve{u}+\frac{1}{2\breve{x}}\frac{\partial\breve{p}}{\partial\eta}-\frac{F'^2}{(2\breve{x})^{1/2}T}\breve{\tau}=0, \tag{3.13}$$

$$\mathcal{Z}|\quad F'\frac{\partial\bar{w}}{\partial\breve{x}}+\frac{1}{2\breve{x}}\left(\frac{\mu T'}{T^2}-F-\frac{\mu'T'}{T}\right)\frac{\partial\bar{w}}{\partial\eta}-\frac{\mu}{2\breve{x}T}\frac{\partial^2\bar{w}}{\partial\eta^2}-k_z^2T\breve{p}=0, \tag{3.14}$$

$$\mathcal{E}\rfloor\quad -\frac{\eta_cT'}{2\breve{x}}\breve{u}-\mathtt{M}^2\frac{(\gamma-1)}{\breve{x}}\frac{\mu F''}{T}\frac{\partial\breve{u}}{\partial\eta}+\frac{T'}{T}\bar{v}+F'\frac{\partial\breve{\tau}}{\partial\breve{x}}+\frac{1}{2\breve{x}}\left(\frac{1}{\mathtt{Pr}}\frac{\mu T'}{T^2}-F-\frac{2}{\mathtt{Pr}}\frac{\mu'T'}{T}\right)\frac{\partial\breve{\tau}}{\partial\eta}+$$

$$\frac{1}{2\breve{x}}\left[\frac{T'F}{T}-\mathtt{M}^2\left(\gamma-1\right)\frac{\mu'}{T}F''^2-\frac{1}{\mathtt{Pr}}\frac{\partial}{\partial\eta}\left(\frac{\mu'T'}{T}\right)\right]\breve{\tau}-\frac{\mu}{2\breve{x}\mathtt{Pr}T}\frac{\partial^2\breve{\tau}}{\partial\eta^2}=0. \tag{3.15}$$

In (3.11)-(3.15), the unsteady effects are still negligible and the perturbation is thus steady. Since we know that the Görtler vortices eventually acquire a modal form it can be inferred that, if (3.11)-(3.15) admit an asymptotic eigensolution, $\hat{x}=\mathcal{O}\left(\mathtt{G}^{-2/5}\right)$ is the location where the Görtler instability ensues (Wu *et al.* 2011).

3.2. *Stage II. Asymptotic eigensolution regime:* $\mathtt{G}^{-2/5}\ll\hat{x}\ll 1$

Following the incompressible case of Wu *et al.* (2011), we assume that the leading order asymptotic eigensolution for $\breve{x}\gg 1$, i.e., $\hat{x}\gg\mathtt{G}^{-2/5}$, and $\eta=\mathcal{O}(1)$ for the middle layer ML is of the form

$$\breve{\mathbf{q}}=\breve{x}^{\varphi}\left[\left(\breve{x}^{-\alpha+1}U_E,\,V_E,\,W_E,\,\breve{x}^{-\alpha+3/2}P_E,\breve{x}^{-\alpha+1}T_E\right)+...\right]e^{\breve{\sigma}(\breve{x})}, \tag{3.16}$$

where the eigenvalue $\breve{\sigma}(\breve{x})$ is expanded at leading order as

$$\breve{\sigma}(\breve{x})=\breve{\sigma}_0\,\breve{x}^{\alpha}+..., \tag{3.17}$$

$\breve{\mathbf{q}}(\hat{x},\eta)=\{\breve{u},\bar{v},\bar{w},\breve{p},\breve{\tau}\}(\hat{x},\eta)$, $\mathbf{Q_E}(\eta)=\{U_E,V_E,W_E,P_E,T_E\}(\eta)$, and $\breve{\sigma}$, α, φ are unknown constants. Substituting (3.16) and (3.17) into (3.14) yields

$$\breve{\sigma}_0\alpha F'\breve{x}^{\alpha}W_E-k_z^2\breve{x}^{-\alpha+5/2}TP_E=\mathcal{O}(1), \tag{3.18}$$

from which, equating the exponentials, $\alpha=5/4$. A system of ordinary differential equations for the eigenfunctions $\mathbf{Q_E}(\eta)$ is then derived by substituting (3.16) and (3.17) into (3.11)-(3.15) and taking the limit $\breve{x}\gg 1$. The resulting inviscid equations are

$$\mathcal{C}\rceil\;\;\alpha\breve{\sigma}_0U_E-\frac{T'}{T^2}V_E+\frac{1}{T}V_E'+W_E-\alpha\breve{\sigma}_0\frac{F'}{T}T_E=0, \tag{3.19}$$

$$\mathcal{X}|\;\;\alpha\breve{\sigma}_0F'U_E+\frac{F''}{T}V_E=0, \tag{3.20}$$

$$\mathcal{Y}|\;\;2\sqrt{2}F'U_E+P_E'-\frac{\sqrt{2}F'^2}{T}T_E=0, \tag{3.21}$$

$$\mathcal{Z}|\;\;\alpha\breve{\sigma}_0F'W_E-k_z^2TP_E=0, \tag{3.22}$$

$$\mathcal{E}\rfloor\;\;\alpha\breve{\sigma}_0F'T_E+\frac{T'}{T}V_E=0. \tag{3.23}$$

These equations can be rearranged to obtain an equation for V_E,

$$\frac{\mathrm{d}^2V_E}{\mathrm{d}\eta^2}-\frac{2T'}{T}\frac{\mathrm{d}V_E}{\mathrm{d}\eta}+\left[\frac{2F''T'}{F'T}-\frac{F'''}{F'}+\frac{\sqrt{2}k_z^2}{(\breve{\sigma}_0\alpha)^2}\left(\frac{2F''T}{F'}-T'\right)\right]V_E=0, \tag{3.24}$$

subject to the boundary conditions

$$\eta=0\rceil\;\;V_E=0, \tag{3.25}$$

$$\eta\to\infty\rfloor\;\;\frac{\mathrm{d}V_E}{\mathrm{d}\eta}\to 0, \tag{3.26}$$

which correspond to the no-penetration and bounded conditions, respectively. Equation (3.24) is solved with the same numerical method used to solve the EV system (2.28)-(2.32). For $\mathtt{M}=0$ the results agree with those of Wu *et al.* (2011). The first three

M	0	0.5	0.9	1.5	3	4
$\breve{\sigma}_0^{(1)}$	0.811	0.828	0.864	0.949	1.259	1.501
$\breve{\sigma}_0^{(2)}$	0.505	0.516	0.538	0.591	0.785	0.937
$\breve{\sigma}_0^{(3)}$	0.370	0.377	0.394	0.433	0.575	0.685
$\breve{\sigma}_1^{(1)}$	-1.567	-1.580	-1.608	-1.676	-1.927	-2.122
$\breve{\sigma}_1^{(2)}$	-1.656	-1.670	-1.700	-1.773	-2.042	-2.248
$\breve{\sigma}_1^{(3)}$	-1.709	-1.723	-1.754	-1.829	-2.105	-2.316
$\breve{\mathtt{B}}$	1.016	1.004	0.978	0.925	0.779	0.701

Table 1: The first three eigenvalues $\breve{\sigma}_0$ from (3.17) and $\breve{\sigma}_1$ from (3.42), and the wall-normal scaling coefficient $\breve{\mathtt{B}}$ used in (3.28) for different Mach numbers.

eigenvalues $\breve{\sigma}_0$ are shown in table 1 for different values of the Mach number. There is a very mild influence of the Mach number in subsonic flow conditions while in supersonic flow conditions $\breve{\sigma}_0$ increases as the Mach number increases, so the Görtler vortices are more unstable as the compressibility effects intensify.

To study the flow in the vicinity of the wall, we take the mean-flow values at $\eta = 0$, i.e., $F = F' = F''' = T' = 0$, while F'', T, $T'' = \mathcal{O}(1)$. Locally, since $\eta = 0$ is a regular singular point, the solution V_E can be written as a Fröbenius series (Wu *et al.* 2011) that gives $V_E'(0) = 1$ when normalized. Additionally, the no-penetration condition requires $V_E(0) = 0$. Taking the derivative of (3.22) and substituting P_E' from (3.21) shows that the spanwise velocity component satisfies the no-slip condition, i.e., $W_E(0) = 0$. However, the streamwise velocity component does not satisfy the no-slip condition since, from (3.19) we find $U_E(0) \to -\left(\breve{\sigma}_0 \alpha T_0\right)^{-1}$, where $T_0 \equiv T(0)$. This is consistent with the inviscid nature of the governing equations (3.19)-(3.23) for $\hat{x} = \mathcal{O}\left(\mathtt{G}^{-2/5}\right)$ from which (3.24) is derived. In order for the streamwise velocity to satisfy the no-slip condition at the wall, a viscous sublayer VS is introduced in the near-wall region. Substituting (3.16) into (3.12) and balancing convection and diffusion in the limits $\eta \to 0$ and $\breve{x} \gg 1$ yields

$$\alpha \breve{\sigma}_0 F' U_E \sim \breve{x}^{-\alpha} \frac{\mu}{2T} U_E'', \tag{3.27}$$

from which

$$\eta \sim \breve{\mathtt{B}}\, \breve{x}^{-5/12}, \tag{3.28}$$

where $\breve{\mathtt{B}} \equiv \left[\mu_0 / \left(2\lambda\alpha\breve{\sigma}_0 T_0\right)\right]^{1/3}$ and T_0, $\mu_0 \equiv \mu(0)$, $\lambda \equiv F''(0)$ arise from Taylor-expanding the mean flow at $\eta = 0$. The thickness of the VS is $\eta_{\mathtt{VS}} = \mathcal{O}\left(\breve{x}^{-5/12}\right)$ where the constant of proportionality $\breve{\mathtt{B}}$ decreases as the Mach number increases, as shown in table 1. The wall-normal scaled variable for the VS becomes

$$\zeta_{\text{II}} = \breve{\mathtt{B}}^{-1} \breve{x}^{5/12} \eta. \tag{3.29}$$

An order of magnitude balance of the equations for $\eta \to 0$ reveals that $P_E = \mathcal{O}(\eta)$ from (3.22), $V_E = \mathcal{O}(\eta)$ from (3.19), and consequently $T_E = \mathcal{O}(\eta)$ from (3.23). Therefore, the solution in the VS expands as

$$\breve{\mathbf{q}} = \breve{x}^{\varphi} \left[\left(\breve{x}^{-1/4} u_s,\, \eta v_s,\, w_s,\, \breve{x}^{1/4} \eta p_s, \breve{x}^{-1/4} \eta \tau_s \right) + \ldots \right] e^{\breve{\sigma}(\breve{x})}, \tag{3.30}$$

where $\check{\mathbf{q}}(\hat{x}, \zeta_{\rm II}) = \{\breve{u}, \breve{v}, \breve{w}, \breve{p}, \breve{\tau}\}(\hat{x}, \zeta_{\rm II})$. Starting from the system of equations (3.11)-(3.15) for $\eta = \mathcal{O}(1)$ and $\breve{x} = \mathcal{O}(1)$, introducing the change of variable (3.29) and the expansion (3.30), the system of equations for $\zeta_{\rm II} = \mathcal{O}(1)$ and $\breve{x} \gg 1$ becomes

$$\mathcal{C}\rceil\ \ \alpha\breve{\sigma}_0 u_s + \frac{1}{T_0} v_s' + w_s = 0, \tag{3.31}$$

$$\mathcal{X}|\ \ \alpha\breve{\sigma}_0 \left(\zeta_{\rm II} u_s - u_s''\right) + \frac{1}{T_0} v_s = 0, \tag{3.32}$$

$$\mathcal{Y}|\ \ p_s' = 0, \tag{3.33}$$

$$\mathcal{Z}|\ \ \lambda\alpha\breve{\sigma}_0 \left(\zeta_{\rm II} w_s - w_s''\right) - k_z^2 T_0 p_s = 0, \tag{3.34}$$

$$\mathcal{E}\rfloor\ \ \tau_s'' = 0, \tag{3.35}$$

where the prime $'$ indicates the derivative with respect to $\zeta_{\rm II}$. The energy equation $\mathcal{E}$ in the `VS` does not contain the pressure and the velocity components. Equations (3.31)-(3.35) are rearranged to obtain an equation for $v_s(\zeta_{\rm II})$,

$$\left(\frac{\mathrm{d}^2}{\mathrm{d}\zeta_{\rm II}^2} - \zeta_{\rm II}\right) v_s'' = 0, \tag{3.36}$$

subject to the boundary conditions

$$\zeta_{\rm II} = 0\rceil\ \ v_s = 0, \qquad v_s' = 0, \tag{3.37}$$

$$\zeta_{\rm II} \to \infty\rfloor\ \ v_s' \to 1. \tag{3.38}$$

The first boundary condition, i.e., $v_s = 0$, represents the no-penetration condition, while the derivatives of the wall-normal velocity come from the continuity equation. Only three boundary conditions are needed since two constants of integration can be obtained from (3.38). The solution of (3.36) has the same form as in the incompressible case of Wu *et al.* (2011),

$$v_s = \mathtt{C}_s \int_0^{\zeta_{\rm II}} \left(\zeta_{\rm II} - \bar{\zeta}_{\rm II}\right) \mathtt{Ai}\left(\bar{\zeta}_{\rm II}\right) \mathrm{d}\bar{\zeta}_{\rm II}, \tag{3.39}$$

where $\mathtt{C}_s = 1/\int_0^\infty \mathtt{Ai}\left(\zeta_{\rm II}\right) \mathrm{d}\zeta_{\rm II} = 3$ and $\mathtt{Ai}$ is the Airy function of the first kind. For $\zeta_{\rm II} \to \infty$ the solution becomes $v_s \to \zeta_{\rm II} + v_\infty$, where the transpiration velocity v_∞ is

$$v_\infty \equiv -\mathtt{C}_s \int_0^\infty \zeta_{\rm II} \mathtt{Ai}\left(\zeta_{\rm II}\right) \mathrm{d}\zeta_{\rm II}. \tag{3.40}$$

For $\zeta_{\rm II} \to \infty$ the `VS` solution must match the `ML` solution for $\eta = \mathcal{O}(1)$.

The transpiration velocity (3.40) thus induces a correction term of order $\mathcal{O}\left(\breve{x}^{-5/12}\right)$ in the `ML`. We can then further expand (3.16) and (3.17) to take this viscous correction into account. We obtain

$$\begin{aligned}\check{\mathbf{q}} =& \breve{x}^{\varphi}\Big[\Big(\breve{x}^{-1/4} U_E,\, V_E,\, W_E,\, \breve{x}^{-1/4} P_E, \breve{x}^{-1/4} T_E\Big) + \\ & \breve{x}^{-5/12}\Big(\breve{x}^{-1/4} U_E^{(1)},\, V_E^{(1)},\, W_E^{(1)},\, \breve{x}^{-1/4} P_E^{(1)}, \breve{x}^{-1/4} T_E^{(1)}\Big) + \ldots\Big] e^{\breve{\sigma}(\breve{x})},\end{aligned} \tag{3.41}$$

where the eigenvalue $\breve{\sigma}(\breve{x})$ expands as

$$\breve{\sigma}(\breve{x}) = \breve{\sigma}_0\, \breve{x}^{5/4} + \breve{x}^{-5/12}\left(\breve{\sigma}_1\, \breve{x}^{5/4}\right) + \ldots\,. \tag{3.42}$$

Substituting (3.41) and (3.42) into (3.11)-(3.15) for $\hat{x} = \mathcal{O}\left(\mathtt{G}^{-2/5}\right)$ and $\eta = \mathcal{O}(1)$, and collecting the $\mathcal{O}\left(\breve{x}^{-5/12}\right)$ terms gives

$$\mathcal{C}\rceil\;\; \frac{5\breve{\sigma}_0}{4}U_E^{(1)} - \frac{T'}{T^2}V_E^{(1)} + \frac{1}{T}V_E'^{(1)} + W_E^{(1)} - \frac{5\breve{\sigma}_0}{4}\frac{F'}{T}T_E^{(1)} = \frac{2\breve{\sigma}_1}{3\breve{\sigma}_0 T}\left(\frac{F''}{F'} - \frac{T'}{T}\right)V_E, \tag{3.43}$$

$$\mathcal{X}|\;\; \frac{5\breve{\sigma}_0}{4}F'U_E^{(1)} + \frac{F''}{T}V_E^{(1)} = \frac{2\breve{\sigma}_1}{3\breve{\sigma}_0}\frac{F''}{T}V_E, \tag{3.44}$$

$$\mathcal{Y}|\;\; 2\sqrt{2}F'U_E^{(1)} + P_E'^{(1)} - \frac{\sqrt{2}F'^2}{T}T_E^{(1)} = 0, \tag{3.45}$$

$$\mathcal{Z}|\;\; \frac{5\breve{\sigma}_0}{4}F'W_E^{(1)} - k_z^2 T P_E^{(1)} - \frac{5\breve{\sigma}_1}{6}\frac{F'}{T}V_E' = -\frac{5\breve{\sigma}_1}{6}\frac{F''}{T}V_E, \tag{3.46}$$

$$\mathcal{E}\rfloor\;\; \frac{T'}{T}V_E^{(1)} + \frac{5\breve{\sigma}_0}{4}F'T_E^{(1)} = \frac{2\breve{\sigma}_1}{3\breve{\sigma}_0}\frac{T'}{T}V_E. \tag{3.47}$$

An equation for $V_E^{(1)}$ can be derived from (3.43)-(3.47),

$$\frac{\mathrm{d}^2V_E^{(1)}}{\mathrm{d}\eta^2} - 2\frac{T'}{T}\frac{\mathrm{d}V_E^{(1)}}{\mathrm{d}\eta} + \left[2\frac{F''T'}{F'T} - \frac{F'''}{F'} + \frac{2\sqrt{2}k_z^2}{\left(\alpha\breve{\sigma}_0\right)^2}\frac{F''T}{F'} - \frac{\sqrt{2}k_z^2}{\left(\alpha\breve{\sigma}_0\right)^2}T'\right]V_E^{(1)} = \frac{10\sqrt{2}k_z^2\breve{\sigma}_1}{3\left(\breve{\sigma}_0\alpha\right)^3}\left(\frac{F''T}{F'} - \frac{1}{2}T'\right)V_E, \tag{3.48}$$

subject to the boundary conditions

$$\eta = 0\rceil\;\; V_E^{(1)}(0) = \breve{\mathtt{B}}\,v_\infty, \tag{3.49}$$

$$\eta \to \infty\rfloor\;\; \frac{\mathrm{d}V_E^{(1)}}{\mathrm{d}\eta} \to 0, \tag{3.50}$$

where (3.49) comes from the matching at $\mathcal{O}\left(\breve{x}^{-5/12}\right)$ of the wall-normal velocity in the ML for $\eta \to 0$ with the wall-normal velocity in the VS for $\zeta_{\text{II}} \to \infty$. Condition (3.50) comes from requiring that the solution be bounded. The eigenvalue $\breve{\sigma}_1$ can either be computed numerically from the solution of (3.48) with its boundary conditions (3.49) and (3.50) or from the solvability condition

$$\frac{10\sqrt{2}k_z^2\breve{\sigma}_1}{3\left(\alpha\breve{\sigma}_0\right)^3}\left(\int_0^\infty \frac{F''T}{F'}{V_E}^2\mathrm{d}\eta - \frac{1}{2}\int_0^\infty T'{V_E}^2\mathrm{d}\eta\right) = \frac{2\lambda\breve{\sigma}_0\alpha T}{\mu}v_\infty\left(1 + 2\int_0^\infty \frac{T'}{T}\frac{\mathrm{d}V_E}{\mathrm{d}\eta}\mathrm{d}\eta\right), \tag{3.51}$$

derived by multiplying (3.48) by V_E, integrating from zero to infinity, and matching the $\mathcal{O}\left(\hat{x}^{-5/12}\right)$ terms of (3.41) with (3.30), using (3.24) and (3.29). The numerical values of $\breve{\sigma}_1$ are shown in table 1. They are all negative, thus indicating decaying perturbations. Similar to the eigenvalues $\breve{\sigma}_0$, the effect of Mach number is very small for subsonic conditions, while in the supersonic regime $\breve{\sigma}_1$ grows in absolute value as compressible effects intensify as the Mach number increases.

The no-slip condition is now satisfied, but we still need to require that the ML solution respect the condition $V_E \to 0$ for $\eta \to \infty$. By requiring the solution to be bounded as the free stream is approached, condition (3.26) gives $V_E = \mathtt{C}_2$, where $\mathtt{C}_2$ is an undefined constant determined by the numerical solution. An outer layer OL must therefore be introduced to allow V_E to vanish as $\eta \to \infty$. Introducing the mean-flow simplification for $\eta \to \infty$, i.e., $F \to \eta - \beta$ and $T = 1$, into (3.19), (3.20), (3.22), and (3.23) we find $U_E = 0$, $T_E = 0$, $W_E = 0$, and $P_E = 0$, respectively. We then expand (3.10) as

$$\bar{u} = \breve{u}\mathtt{G}^{-2/5} + \mathcal{O}\left(\mathtt{G}^{-3/5}\right), \qquad \bar{\tau} = \breve{\tau}\mathtt{G}^{-2/5} + \mathcal{O}\left(\mathtt{G}^{-3/5}\right), \qquad \bar{p} = \breve{p}\mathtt{G}^{2/5} + \mathcal{O}\left(\mathtt{G}^{1/5}\right). \tag{3.52}$$

Substituting these expansions into the $\mathcal{Y}$ equation (2.11) and neglecting terms $\ll \mathtt{G}^{-2/5}$, the equation is balanced if $\eta_{\mathtt{OL}} \sim \mathtt{G}^{1/5}\left(2\breve{x}\right)^{-1/2}$. It follows that the new $\mathcal{O}(1)$ wall-normal coordinate for the OL is

$$y_0 = \mathtt{G}^{-1/5}\left(2\breve{x}\right)^{1/2}\eta. \tag{3.53}$$

From (2.9) and (3.52), the scaling in the OL for $y_0 = \mathcal{O}(1)$ is

$$\bar{\mathbf{q}} = \left\{\mathtt{G}^{-3/5}\bar{u}_0,\ \bar{v}_0,\ \mathtt{G}^{-1/5}\bar{w}_0,\ \mathtt{G}^{1/5}\bar{p}_0,\ \mathtt{G}^{-3/5}\bar{\tau}_0\right\}, \tag{3.54}$$

where $\bar{\mathbf{q}}(\breve{x}, y_0) = \{\bar{u}, \bar{v}, \bar{w}, \bar{p}, \bar{\tau}\}(\breve{x}, y_0)$. Substituting (3.54) into the LUBR equations (2.9)-(2.13) and taking the limit $\eta \to \infty$ gives the OL system

$$\mathcal{C}\rceil \quad (2\breve{x})^{1/2}\frac{\partial \bar{v}_0}{\partial y_0} + \bar{w}_0 = 0, \tag{3.55}$$

$$\mathcal{X}| \quad \frac{\partial \bar{u}_0}{\partial y_0} = 0, \tag{3.56}$$

$$\mathcal{Y}| \quad \frac{\bar{v}_0}{2\breve{x}} + \frac{\partial \bar{v}_0}{\partial \breve{x}} + \frac{1}{(2\breve{x})^{1/2}}\frac{\partial \bar{p}_0}{\partial y_0} = 0, \tag{3.57}$$

$$\mathcal{Z}| \quad \frac{\partial \bar{w}_0}{\partial y_0} - k_z^2 \bar{p}_0 = 0, \tag{3.58}$$

$$\mathcal{E}\rfloor \quad \frac{\partial \bar{\tau}_0}{\partial y_0} = 0, \tag{3.59}$$

where, in order to satisfy the boundary condition $V_E \to 0$ as $\eta \to \infty$, $\bar{u}_0$ and $\bar{\tau}_0$ must be set to zero. The solution to (3.55)-(3.59) is

$$\{\bar{p}_0, \bar{w}_0, \bar{v}_0\} = \left\{g_0', k_z^2 g_0, |k_z| g_0 / \left(2\breve{x}\right)\right\} e^{-|k_z| y_0}, \tag{3.60}$$

where

$$g_0(\breve{x}) = \breve{x}^{\gamma+1/2}\left[V_{E,\infty} + \mathcal{O}\left(\breve{x}^{-5/12}\right)\right] e^{\breve{\sigma}(\breve{x})} \tag{3.61}$$

and $V_{E,\infty} = V_E(\eta \to \infty)$ is determined by solving (3.24) numerically.

3.3. *Stage III. Fully developed regime: $\hat{x} = \mathcal{O}(1)$*

As the instability develops further downstream the local boundary-layer thickness δ^* becomes of the same order as the spanwise wavelength λ_z^*, i.e., $\delta^* = \mathcal{O}(\lambda_z^*)$, and the spanwise viscous diffusion and the spanwise pressure gradient are at work. At this location the Görtler vortices are fully developed (Wu *et al.* 2011) with $\breve{x} = \mathcal{O}\left(\mathtt{G}^{2/5}\right)$, i.e., $\hat{x} = \mathcal{O}(1)$, $\eta_{\mathtt{OL}} = \mathcal{O}(1)$ and the OL merging with the ML. Stage III is therefore only composed of the ML and the VS. Equations (3.41), (3.42), and (3.52) suggest that the solution in the fully developed regime can be expanded in the WKBJ form (Wu *et al.* 2011)

$$\bar{\mathbf{q}} = \Big\{ \Big[\mathtt{G}^{-1/2}u_0, v_0, w_0, \mathtt{G}^{1/2}p_0, \mathtt{G}^{-1/2}\tau_0\Big] + \mathtt{G}^{-1/6}\Big[\mathtt{G}^{-1/2}u_1, v_1, w_1, \mathtt{G}^{1/2}p_1, \mathtt{G}^{-1/2}\tau_1\Big] + \ldots\Big\} e^{\mathtt{G}^{1/2}\int^{\hat{x}}\hat{\sigma}(x)\mathrm{d}x}, \tag{3.62}$$

where

$$\hat{\sigma}(\hat{x}) = \hat{\sigma}_0 + \mathtt{G}^{-1/6}\hat{\sigma}_1 + \ldots, \tag{3.63}$$

and the second term of order $\mathcal{O}(\mathtt{G}^{-1/6})$ takes into account the effect of the VS. Substituting (3.62) into the LUBR equations (2.9)-(2.13) gives the system at leading order for $\hat{x} = \mathcal{O}(1)$ and $\eta = \mathcal{O}(1)$,

$$\mathcal{C}\rceil\ \ \hat{\sigma}_0 u_0 - \frac{T'}{T^2}v_0 + \frac{1}{T}\frac{\partial v_0}{\partial \eta} + w_0 - \hat{\sigma}_0\frac{F'}{T}\tau_0 = 0, \tag{3.64}$$

$$\mathcal{X}|\ \ \hat{\sigma}_0 F' u_0 + \frac{F''}{T}v_0 = 0, \tag{3.65}$$

$$\mathcal{Y}|\ \ \frac{2F'}{(2\hat{x})^{1/2}}u_0 + \hat{\sigma}_0 F' v_0 - \frac{F'^2}{(2\hat{x})^{1/2}T}\tau_0 + \frac{1}{2\hat{x}}\frac{\partial p_0}{\partial \eta} = 0, \tag{3.66}$$

$$\mathcal{Z}|\ \ \hat{\sigma}_0 F' w_0 - k_z^2 T p_0 = 0, \tag{3.67}$$

$$\mathcal{E}\rfloor\ \ \hat{\sigma}_0 F' \tau_0 + \frac{T'}{T}v_0 = 0. \tag{3.68}$$

We can rearrange (3.64)-(3.68) to find

$$\frac{\partial^2 v_0}{\partial \eta^2} - \frac{2T'}{T}\frac{\partial v_0}{\partial \eta} + \left[\frac{2F''T'}{F'T} - \frac{F'''}{F'} - 2\hat{x}k_z^2T^2 + (2\hat{x})^{1/2}\frac{k_z^2}{\hat{\sigma}_0^2}\left(\frac{2F''T}{F'} - T'\right)\right]v_0 = 0, \tag{3.69}$$

subject to the boundary conditions

$$\eta = 0\rceil\ \ v_0 = 0, \tag{3.70}$$

$$\eta \to \infty\rfloor\ \ v_0 \to 0. \tag{3.71}$$

Note that v_0 vanishes as $\eta \to \infty$ since no outer layer is needed to take the wall-normal velocity to zero like in stage II. Equation (3.69), also derived by Dando & Seddougui (1993), is solved with the same method used to solve (3.24) and the EV system (2.28)-(2.32). In the limit $\hat{x} \to 0$ the solution in the fully developed regime of stage III must be consistent with the solution of the asymptotic stage II. The dominant balance in (3.69) shows that, in order for all the terms except the third term in the brackets to remain $\mathcal{O}(1)$, $\hat{\sigma}_0 = \mathcal{O}\left(\hat{x}^{1/4}\right)$ and, from the exponential in (3.62),

$$\int^{\hat{x}} \hat{\sigma}_0(x)\mathrm{d}x \sim \frac{4}{5}\hat{x}^{5/4}, \tag{3.72}$$

which is consistent, at leading order, with the exponential in (3.41).

Changing the Mach number affects the boundary-layer thickness δ_{99}^*, i.e., the wall-normal location where $U^* = 0.99U_\infty^*$, and η through the mean temperature T. We therefore use the dimensionless wall-normal coordinate $y_{99} \equiv y^*/\delta_{99}^*$ when comparing

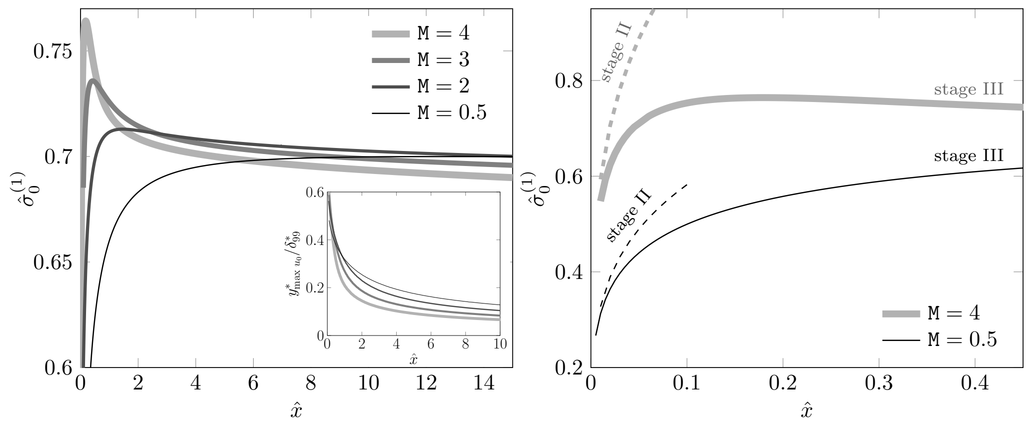

Figure 3: The effect of the Mach number on $\hat{\sigma}_0^{(1)}$ (left) and detail of the graph on the left in the region $\hat{x} \ll 1$ for comparison with stage II (right). Inset: the wall-normal location of $\mathtt{G_V}$-vortices (right) for stage III.

results at different Mach numbers. Figure 3 (left) shows the growth rate of the perturbation along the streamwise direction for the first eigenvalue $\hat{\sigma}_0^{(1)}$. As the Mach number increases, its stabilizing effect begins closer to the leading edge. Up to $\mathtt{M} = 2$, the growth rate at $\hat{x} \approx 15$ converges to a constant. The wall-normal location of the vortices, shown in the inset of figure 3 (left), decreases as the Mach number increases. However, for $\mathtt{M} > 3$ and high enough $\hat{x}$ the location of the vortices asymptotically approaches a constant value. Figure 3 (right) demonstrates that for $\hat{x} \ll 1$ the growth rate (3.63) from stage III asymptotically matches the growth rate (3.17) from stage II.

In stage III, as for the asymptotic eigensolution regime of stage II, a VS has to be introduced to guarantee that the no-slip condition at the wall will be satisfied because it is found that $u_0 \to -\left(\hat{\sigma}_0 T_0\right)^{-1}$ as $\eta \to 0$. Substituting (3.62) into the $\mathcal{X}$ equation (2.10) and balancing the convection and the diffusion terms in the limit $\eta \to 0$, the new $\mathcal{O}(1)$ wall-normal scaling variable, proportional to the VS thickness, becomes

$$\zeta_{\text{III}} = \mathtt{G}^{1/6}\, \hat{\mathtt{B}}^{-1}\, \hat{x}^{1/3} \eta, \tag{3.73}$$

where $\hat{\mathtt{B}}(\hat{x}) \equiv \left[\mu_0 / \left(2\lambda \hat{\sigma}_0 T_0\right)\right]^{1/3}$. A comparison with (3.29) shows that, by fixing G and $\hat{\mathtt{B}}$, if $\hat{x}$ increases the VS becomes thinner more rapidly in stage II $\left(\mathcal{O}\left(\hat{x}^{-5/12}\right)\right)$ than in stage III $\left(\mathcal{O}\left(\hat{x}^{-1/3}\right)\right)$ since ζ_{II} and ζ_{III} are of order one. The value of $\hat{\mathtt{B}}(\hat{x})$ approaches a constant for $\hat{x} > 5$. From (3.73) it can be noticed that, in order to maintain $\zeta_{\text{III}} = \mathcal{O}(1)$, η must increase when G increases, i.e., the VS thickness is larger for flows over strong curvature. Substituting (3.62) into the LUBR equations (2.9)-(2.13) and balancing the convection and diffusion terms gives the expansion of the flow in the VS,

$$\bar{\mathbf{q}} = \left\{ \mathtt{G}^{-1/2} u_b, \mathtt{G}^{-1/6} \hat{\mathtt{B}} \hat{x}^{-1/3} v_b, w_b, \mathtt{G}^{-2/3} \hat{\mathtt{B}} \hat{x}^{-1/3} p_b, \mathtt{G}^{-1/2} \tau_b \right\} e^{\mathtt{G}^{1/2} \int^{\hat{x}} \hat{\sigma}(x) \mathrm{d}x}, \tag{3.74}$$

where $\bar{\mathbf{q}}(\hat{x}, \zeta_{\text{III}}) = \{\bar{u}, \bar{v}, \bar{w}, \bar{p}, \bar{\tau}\}(\hat{x}, \zeta_{\text{III}})$. By substituting (3.74) into the LUBR equations (2.9)-(2.13), we recover the system of equations for $\hat{x} = \mathcal{O}(1)$ and $\eta \to 0$,

$$\mathcal{C}\rceil \;\; \hat{\sigma}_0 u_b + \frac{1}{T_0} v_b' + w_b = 0, \tag{3.75}$$

$$\mathcal{X}| \;\; \hat{\sigma}_0 \left(\zeta_{\rm III} u_b - u_b''\right) + \frac{1}{T_0} v_b = 0, \tag{3.76}$$

$$\mathcal{Y}| \;\; p_b' = 0, \tag{3.77}$$

$$\mathcal{Z}| \;\; \lambda \hat{\sigma}_0 \left(\zeta_{\rm III} w_b - w_b''\right) - k_z^2 T_0 p_b = 0, \tag{3.78}$$

$$\mathcal{E}\rfloor \;\; \tau_b' = 0, \tag{3.79}$$

where the prime $'$ indicates the derivative with respect to $\zeta_{\rm III}$. The equations are similar to the asymptotic eigensolution equations (3.31)-(3.35) and therefore v_b satisfies the Airy equation (3.36) along with the boundary conditions (3.37) and (3.38). A composite solution for the streamwise velocity u_c can be constructed from the solution in the $\mathtt{ML}$ and $\mathtt{VS}$, i.e., u_0 and u_b, respectively, as

$$u_c = u_0 + u_b - u_{com}, \tag{3.80}$$

where

$$u_{com} = \lim_{\eta \to 0} u_0 = \lim_{\zeta_{\rm III} \to \infty} u_b = -\frac{1}{\hat{\sigma}_0 T_0} \tag{3.81}$$

is the common solution.

The streamwise velocity u_b is computed by integrating (3.76) through the method of variation of parameters with the known velocity v_b as the forcing term. The solution is:

$$u_b(\zeta_{\rm III}) = \mathtt{C}_1 \mathtt{Ai} + \mathtt{C}_2 \mathtt{Bi} - \mathtt{Ai} \int_0^{\zeta_{\rm III}} \frac{\mathtt{f}\;\mathtt{Bi}}{\mathtt{W}} \mathrm{d}\bar{\zeta}_{\rm III} + \mathtt{Bi} \int_0^{\zeta_{\rm III}} \frac{\mathtt{f}\;\mathtt{Ai}}{\mathtt{W}} \mathrm{d}\bar{\zeta}_{\rm III}, \tag{3.82}$$

where $\mathtt{Ai} = \mathtt{Ai}(\zeta_{\rm III})$ and $\mathtt{Bi} = \mathtt{Bi}(\zeta_{\rm III})$ are the two linearly independent solutions of the Airy equation, $\mathtt{f}(\zeta_{\rm III}) = v_b(\zeta_{\rm III})/(\hat{\sigma}_0 T_0)$ and $\mathtt{W}(\zeta_{\rm III}) = \mathtt{Ai}\,\mathtt{Bi}' - \mathtt{Bi}\,\mathtt{Ai}'$ is the Wronskian. The constant $\mathtt{C}_2 = -0.2061$ is found first by numerically imposing the outer boundary condition (3.81) as the term proportional to $\mathtt{C}_1$ vanishes as $\zeta_{\rm III} \to \infty$. Once $\mathtt{C}_2$ is known, the constant $\mathtt{C}_1 = 0.3571$ is found by imposing the first of (3.37). The resulting solutions $\bar{u}_b$, $\bar{u}_0$, and $\bar{u}_c$ for $\mathtt{M} = 0.5$ and $\mathtt{M} = 3$ are displayed in figure 4. These results confirm that as the Mach number increases, but still remaining an order-one quantity, the vortices tend to move towards the wall when $\mathtt{G} \gg 1$. The requirement of a very high $\mathtt{G}$ value in figure 4 arises from the inner coordinate being proportional to $\mathtt{G}^{1/6}$ in (3.73) and is necessary to guarantee that the $\mathtt{VS}$ is thinner than the $\mathtt{ML}$. The composite solution follows the inner $\mathtt{VS}$ solution near the wall and the outer $\mathtt{ML}$ solution away from the wall.

The viscous correction for $\hat{x} = \mathcal{O}(1)$ and $\eta = \mathcal{O}(1)$ is found by substituting the expansion (3.62) into the LUBR equations (2.9)-(2.13) and collecting the $\mathcal{O}\left(\mathtt{G}^{-1/6}\right)$ terms for $u_1, v_1, w_1, p_1, \tau_1$ in (3.62),

$$\mathcal{C}\rceil \;\; \hat{\sigma}_0 u_1 - \frac{T'}{T^2} v_1 + \frac{1}{T}\frac{\partial v_1}{\partial \eta} + w_1 - \hat{\sigma}_0 \frac{F'}{T} \tau_1 - \hat{\sigma}_1 \frac{F'}{T} \tau_0 + \hat{\sigma}_1 u_0 = 0, \tag{3.83}$$

$$\mathcal{X}| \;\; \hat{\sigma}_0 F' u_1 + \frac{F''}{T} v_1 + \hat{\sigma}_1 F' u_0 = 0, \tag{3.84}$$

$$\mathcal{Y}| \;\; \frac{2F'}{(2\hat{x})^{1/2}} u_1 + \hat{\sigma}_0 F' v_1 + \frac{1}{2\hat{x}} \frac{\partial p_1}{\partial \eta} - \frac{F'^2}{(2\hat{x})^{1/2}\, T} \tau_1 + \hat{\sigma}_1 F' v_0 = 0, \tag{3.85}$$

$$\mathcal{Z}| \;\; \hat{\sigma}_0 F' w_1 - k_z^2 T p_1 + \hat{\sigma}_1 F' w_0 = 0, \tag{3.86}$$

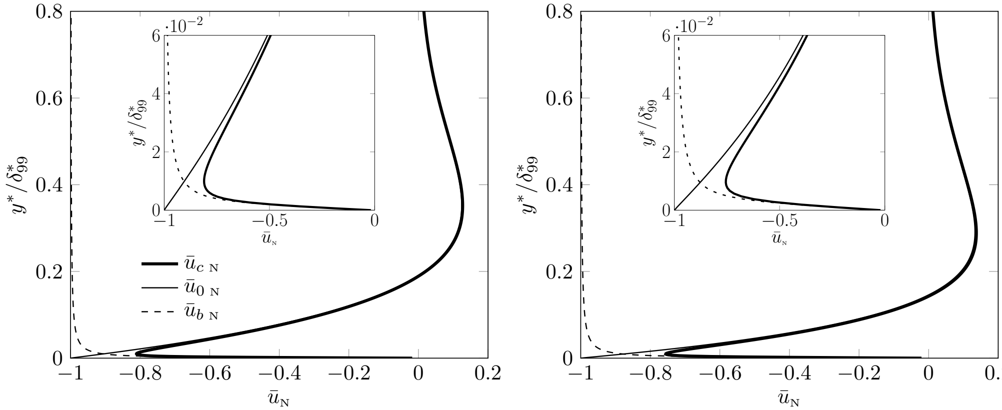

Figure 4: Normalized profiles of the streamwise velocity perturbation for $\mathtt{M} = 0.5$ (left) and $\mathtt{M} = 3$ (right) from the eigensolution of stage III at $\mathtt{G} = 10^{15}$ and $\hat{x} = 1$. Insets: details of the solutions near the wall.

$$\mathcal{E}\rfloor \quad \frac{T'}{T} v_1 + \hat{\sigma}_0 F' \tau_1 + \hat{\sigma}_1 F' \tau_0 = 0, \tag{3.87}$$

from which the equation for v_1 is derived

$$\frac{\partial^2 v_1}{\partial \eta^2} - 2\frac{T'}{T}\frac{\partial v_1}{\partial \eta} + \left[2\frac{F''T'}{F'T} - \frac{F'''}{F'} - 2\hat{x}k_z^2 T^2 + \frac{2\,(2\hat{x})^{1/2}\,k_z^2}{\hat{\sigma}_0^2}\frac{F''T}{F'} - \frac{(2\hat{x})^{1/2}\,k_z^2}{\hat{\sigma}_0^2} T' \right] v_1 =$$

$$\frac{2\,(2\hat{x})^{1/2}\,k_z^2 \hat{\sigma}_1}{\hat{\sigma}_0^3} \left(2\frac{F''T}{F'} - T' \right) v_0, \tag{3.88}$$

along with its boundary conditions

$$\eta = 0\rceil \quad v_1 = \hat{\mathtt{B}}\,\hat{x}^{-1/3} v_\infty, \tag{3.89}$$

$$\eta \to \infty\rfloor \quad \frac{\partial v_1}{\partial \eta} \to 0. \tag{3.90}$$

As for the asymptotic eigensolution regime, the boundary condition for $\eta \to 0$ stems from the matching with the ML solution. Applying the solvability condition to (3.88) gives

$$\left(1 + 2\int_0^\infty \frac{T'}{T}\frac{\partial v_0}{\partial \eta} \mathrm{d}\eta \right) \left(\frac{2\lambda \hat{\sigma}_0 T}{\mu} \right)^{-1/3} \hat{x}^{-1/3} v_\infty =$$

$$- \frac{2\,(2\hat{x})^{1/2}\,k_z^2 \hat{\sigma}_1}{\hat{\sigma}_0^3} \left(\int_0^\infty T' v_0^2 \mathrm{d}\eta - 2\int_0^\infty \frac{F''T}{F'} v_0^2 \mathrm{d}\eta - 2\int_0^\infty \frac{F''T}{F'} v_0^2 \mathrm{d}\eta \right). \tag{3.91}$$

The eigenvalue $\hat{\sigma}_1$ can either be calculated from the solvability condition or from the numerical integration of (3.88).

3.4. *Stage IV. Wall layer regime: $\hat{x} \gg 1$*

It has been shown by Hall (1983) and Wu *et al.* (2011) for the incompressible case that, contrary to the Klebanoff modes generated over flat plates, Görtler vortices move towards the surface as they develop downstream in the limit $\hat{x} \gg 1$ ($\delta^* \gg \lambda_z^*$). It will be shown in §4 that this is true only up to $\mathtt{M} \simeq 3$. For $\mathtt{M} \geqslant 3$, the perturbation initially tends to concentrate near the wall, but then, as $\hat{x}$ increases, it moves to the core of the boundary layer. Following the work of Wu *et al.* (2011), the eigenvalue problem for the inviscid regime (3.69) can be simplified in the limit $\hat{x} \gg 1$ and $\eta \to 0$. From the simplifications of the mean flow near the wall and introducing a new WL variable $\hat{\zeta}_{\text{III}} = (2\hat{x})^{1/2}\,\eta T_0$ to cancel the dependence on $\hat{x}$, (3.69) simplifies to

$$\frac{\partial^2 v_0}{\partial \hat{\zeta}_{\text{III}}^2} - \left(1 - \frac{2}{\hat{\zeta}_{\text{III}}\hat{\sigma}_0^2}\right) k_z^2 v_0 = 0. \tag{3.92}$$

This equation is the same as for the incompressible case and has a set of eigenvalues $\hat{\sigma}_0 = (k_z/n)^{1/2}$, with $n = 1, 2, 3, ...$ (Denier *et al.* 1991). Applying the same procedure to (3.88), we find that $\hat{\sigma}_1 = \mathcal{O}\left(\hat{x}^{1/6}\right)$ for $\hat{x} \gg 1$ and $\eta \to 0$, which implies that, referring to (3.63), the viscous correction terms for the growth rate at $\eta = \mathcal{O}(1)$ become of leading order as the flow evolves to $\hat{x} = \mathcal{O}(\mathtt{G})$.

For $\hat{x} \gg 1$, we investigate the flow at $\hat{x} = \mathcal{O}(\mathtt{G})$, where the viscous correction term becomes of leading order. The streamwise and wall-normal variables rescale as

$$\tilde{x} = \frac{\hat{x}}{\mathtt{G}}, \qquad \zeta_{\text{IV}} = (2\tilde{x})^{1/2}\,\eta \mathtt{G}^{1/2} T_0, \tag{3.93}$$

respectively. From an order of magnitude analysis of the LUBR equations (2.9)-(2.13) the flow expands as

$$\bar{\mathbf{q}} = \left\{\tilde{u}_0, \tilde{v}_0, \mathtt{G}^{1/2}\tilde{w}_0, \mathtt{G}^{1/2}\tilde{p}_0, \mathtt{G}^{1/2}\tilde{\tau}_0\right\} e^{\mathtt{G}^{3/2}\int^{\tilde{x}} \hat{\sigma}(x)\mathrm{d}x}, \tag{3.94}$$

where $\bar{\mathbf{q}}(\tilde{x}, \zeta_{\text{IV}}) = \{\bar{u}, \bar{v}, \bar{w}, \bar{p}, \bar{\tau}\}(\tilde{x}, \zeta_{\text{IV}})$. Substituting (3.94) into the LUBR equations (2.9)-(2.13) and using the near-wall approximations for the mean flow, the system of equations for $\hat{x} = \mathcal{O}(\mathtt{G})$ becomes

$$\mathcal{C}\rceil \;\; \hat{\sigma}\tilde{u}_0 + (2\tilde{x})^{1/2}\frac{\partial \tilde{v}_0}{\partial \zeta_{\text{IV}}} + \tilde{w}_0 + \left[\frac{ik_x\mathtt{R}}{T} - \frac{\lambda\zeta_{\text{IV}}\hat{\sigma}}{(2\tilde{x})^{1/2}T^2}\right]\tilde{\tau}_0 = 0, \tag{3.95}$$

$$\mathcal{X}| \;\; \left[-ik_x\mathtt{R} + \frac{\zeta_{\text{IV}}\hat{\sigma}}{(2\tilde{x})^{1/2}}\frac{\lambda}{T} + k_z^2\mu T\right]\tilde{u}_0 - \mu T\frac{\partial^2 \tilde{u}_0}{\partial \zeta_{\text{IV}}^2} + \frac{\lambda}{T}\tilde{v}_0 - \frac{\lambda\mu'}{(2\tilde{x})^{1/2}}\frac{\partial \tilde{\tau}_0}{\partial \zeta_{\text{IV}}} = 0, \tag{3.96}$$

$$\begin{aligned}\mathcal{Y}| \;\; &\frac{\zeta_{\text{IV}}}{\tilde{x}}\frac{\lambda}{T}\tilde{u}_0 + \left[\frac{\zeta_{\text{IV}}\hat{\sigma}}{(2\tilde{x})^{1/2}}\frac{\lambda}{T} - ik_x\mathtt{R} + k_z^2\mu T\right]\tilde{v}_0 - \mu T\frac{\partial^2 \tilde{v}_0}{\partial \zeta_{\text{IV}}^2} + \frac{T}{(2\tilde{x})^{1/2}}\frac{\partial \tilde{p}_0}{\partial \zeta_{\text{IV}}} - \\ &\left[\frac{(\zeta_{\text{IV}}\lambda)^2}{(2\tilde{x})^{3/2}T} + \frac{\hat{\sigma}\mu'\lambda}{2\tilde{x}} + \frac{\zeta_{\text{IV}}\hat{\sigma}\mu'\lambda}{(2\tilde{x})^2} + \frac{\hat{\sigma}\mu\lambda}{6\tilde{x}T}\right]\tilde{\tau}_0 + \left[\frac{ik_x\mathtt{R}\mu}{3\,(2\tilde{x})^{1/2}} + \frac{\zeta_{\text{IV}}\hat{\sigma}\mu\lambda}{6\tilde{x}T}\right]\frac{\partial \tilde{\tau}_0}{\partial \zeta_{\text{IV}}} = 0,\end{aligned} \tag{3.97}$$

$$\mathcal{Z}| \;\; \left[\frac{\zeta_{\text{IV}}\hat{\sigma}\lambda}{(2\tilde{x})^{1/2}T} - ik_x\mathtt{R} + k_z^2\mu T\right]\tilde{w}_0 - \mu T\frac{\partial^2 \tilde{w}_0}{\partial \zeta_{\text{IV}}^2} - k_z^2 T\tilde{p}_0 = 0, \tag{3.98}$$

$$\mathcal{E}\rfloor \;\; \left[\frac{k_z^2}{\mathtt{Pr}}\mu T - ik_x\mathtt{R} + \frac{\zeta_{\text{IV}}\hat{\sigma}\lambda}{(2\tilde{x})^{1/2}T}\right]\tilde{\tau}_0 - \frac{\mu T^2}{\mathtt{Pr}}\frac{\partial^2 \tilde{\tau}_0}{\partial \zeta_{\text{IV}}^2} = 0. \tag{3.99}$$

These equations could be rearranged to eliminate $\tilde{w}_0$ and $\tilde{v}_0$. The boundary conditions are $\tilde{u}_0 = \tilde{v}_0 = \tilde{\tau}_0 = 0$ for $\zeta_{\text{IV}} = 0$ and $\tilde{u}_0$, $\tilde{v}_0$, $\tilde{\tau}_0 \to 0$ for $\zeta_{\text{IV}} \to \infty$. Finally, for $\tilde{x} = \mathcal{O}(1)$ and from the boundary-layer thickness $\delta^* = \mathcal{O}\left((\nu_\infty x^*/U_\infty^*)^{1/2}\right)$, we find that $\delta^*/\lambda_z^* = \mathcal{O}\left(\mathtt{G}^{1/2}\right)$, identified by Denier *et al.* (1991) as the most unstable regime for incompressible Görtler flow.

3.5. *Summary of physical results emerging from asymptotic analysis*

From the asymptotic analysis in the limit $\mathtt{G} \gg 1$, we can infer the following physical properties:

- as in the incompressible case, the unbalance between pressure and centrifugal forces triggers the Görtler instability at a streamwise location $\hat{x} = \mathcal{O}\left(\mathtt{G}^{-2/5}\right)$, i.e., when both the wall-normal and the spanwise pressure gradients are active in the wall-normal and spanwise momentum equations, respectively;
- in stage II, i.e., where the boundary-layer equations describe the flow as the spanwise viscous diffusion effects are negligible, increasing the Mach number causes:
  - the boundary-layer perturbation to intensify, as shown by the eigenvalues in table 1;
  - the perturbation to shift away from the wall;
- in stage III, i.e., further downstream where the flow is described by the boundary-region equations because the spanwise viscous diffusion and the spanwise pressure gradient are at work:
  - the growth rate decreases slightly downstream, as shown in figure 4;
  - increasing the Mach number has a stabilizing effect on the growth rate, which is more intense in supersonic flow conditions, as figure 4 shows;
  - for $\mathtt{M} = \mathcal{O}(1)$, the vortices move towards the wall as the Mach number increases, as shown in figure 3 and figure 4;
  - we have obtained a composite asymptotic solution, whose near-wall part is fully viscous and adiabatic, while the part in the boundary-layer core is inviscid.

4. Numerical results

In §4.1, we first present the results based on the LUBR equations, which are valid for the entire evolution of the boundary-layer perturbation. We then discuss the comparison between the LUBR results with the results obtained through the EV framework valid for $\hat{x} \gg 1$ in §4.2 and the asymptotic results (ASY) valid for $\mathtt{G} \gg 1$ and $\hat{x} = \mathcal{O}(1)$ in §4.3. In §4.4, the LUBR results are compared qualitatively with the DNS results by Whang & Zhong (2003).

4.1. *Unsteady boundary-region results*

Using the LUBR equations, we investigate the dependence of the evolution of compressible Görtler vortices on four main parameters, i.e., the Mach number, the Görtler number, the ratio of the disturbance wavelengths in the free stream, and the frequency. In order to obtain realistic results, this parametric analysis is based on wind tunnel data of compressible flows.

4.1.1. *Effect of Mach number*

The effect of the Mach number is investigated while keeping a constant unit Reynolds number $\mathtt{R}_u^* = U_\infty^*/\nu_\infty^*$. As the free-stream mean velocity U_∞^* changes, it directly affects both $\mathtt{M}$ and $\mathtt{R}_u^*$, p_∞^* affects $\mathtt{R}_u^*$ through ν_∞^*, whereas T_∞^* modifies $\mathtt{M}$ through the speed of sound $a_\infty^* = a_\infty^*(T_\infty^*)$ and changes $\mathtt{R}_u^*$ through ν_∞^*. The Reynolds number $\mathtt{R}_u^*$ is thus kept

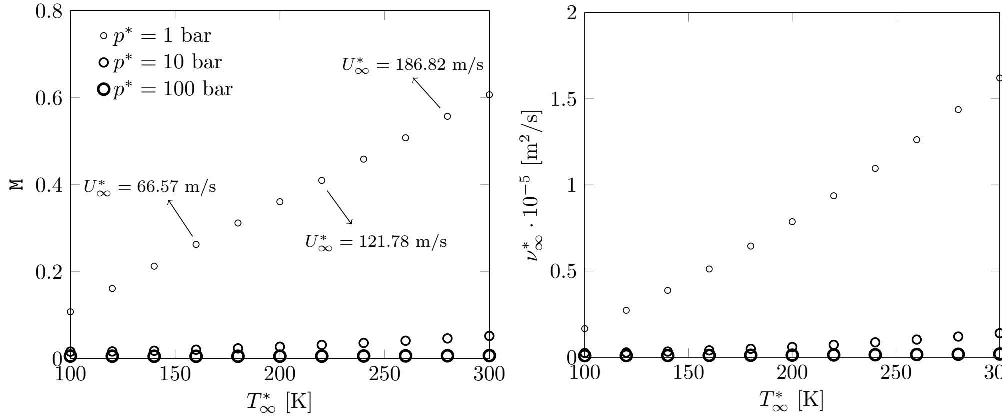

Figure 5: Influence of pressure p^*_∞ and temperature T^*_∞ on the subsonic Mach number (left) and on the kinematic viscosity ν^*_∞ of air (right) for $\mathtt{R}^*_u = 13 \cdot 10^6$ m^{-1}. The points in the two graphs correspond to the same flow conditions.

constant by selecting the correct combination of U^*_∞, T^*_∞, and p^*_∞ as the desired $\mathtt{M}$ is achieved. Figure 5 shows the influence of the free-stream temperature and pressure on the subsonic Mach number (left) and the free-stream kinematic viscosity (right).

This approach has been used in several wind tunnel studies. Laufer (1954) conducted experiments in the supersonic wind tunnel of the Jet Propulsion Laboratory in the range $1.4 < \mathtt{M} < 4$, with $\mathtt{R}^*_u = 13.3 \cdot 10^6$ m^{-1} and a free stream dominated by vortical disturbances. No information on the pressure and temperature conditions was given in their article. Flechner *et al.* (1976) studied transitional boundary layers in the transonic tunnel at NASA Langley Research Center and maintained the stagnation temperature at 322 K. Three different Mach numbers $\mathtt{M} = 0.7, 0.8, 0.83$ were investigated through a change in the free-stream dynamic pressure while keeping $\mathtt{R}^*_u = 13.1 \cdot 10^6$ m^{-1}. This wind tunnel was equipped with a control system that allowed independent variation of Mach number, stagnation pressure, and temperature. We consider the cases of steady vortices (frequency $f^* = 0$) in conditions similar to the experimental configuration of De Luca *et al.* (1993), i.e., with spanwise wavelength $\lambda^*_z = 8 \cdot 10^{-3}$m, corresponding to $\mathtt{R} = 1273.2$, and radius of curvature $r^* = 10$m, corresponding to $\mathtt{G} = 206.4$. The Mach number is limited to $\mathtt{M} \leqslant 4$ to maintain valid the assumptions of ideal gas and constant Prandtl number. The dimensionless wall-normal coordinate $y_{99} \equiv y^*/\delta^*_{99}$ is used when comparing results at different Mach numbers.

The maximum along y_{99} of the amplitude of the streamwise velocity perturbation $|\bar{u}(\hat{x})|_{\max} \equiv \max_{y_{99}} |\bar{u}(\hat{x}, y_{99})|$ as a function of $\hat{x}$ is shown in figure 6 (left) for different Mach numbers. For $\hat{x} = \mathcal{O}(1)$, increasing $\mathtt{M}$ decreases the growth rate, i.e., the kinematic Görtler vortices ($\mathtt{G_V}$-vortices) become more stable, especially for supersonic flows. This confirms the asymptotic results for stage III. This is true only sufficiently downstream from the leading edge where the Görtler instability is fully developed and δ^* is comparable with λ^*_z. In the early stages of the streamwise-velocity perturbation where instead the spanwise viscous diffusion is negligible, the effect of the Mach number is reversed as shown in the inset of figure 6 (left). This confirms the theoretical results for stage II. The stabilizing effect of the Mach number when $\delta^* = \mathcal{O}(\lambda^*_z)$ is in accordance with early studies utilizing linearized theories for the primary instability (Hammerlin 1961; Kobayashi & Kohama 1977; El-Hady & Verma 1983; Spall & Malik 1989; Hall & Malik 1989; Wadey 1992). The

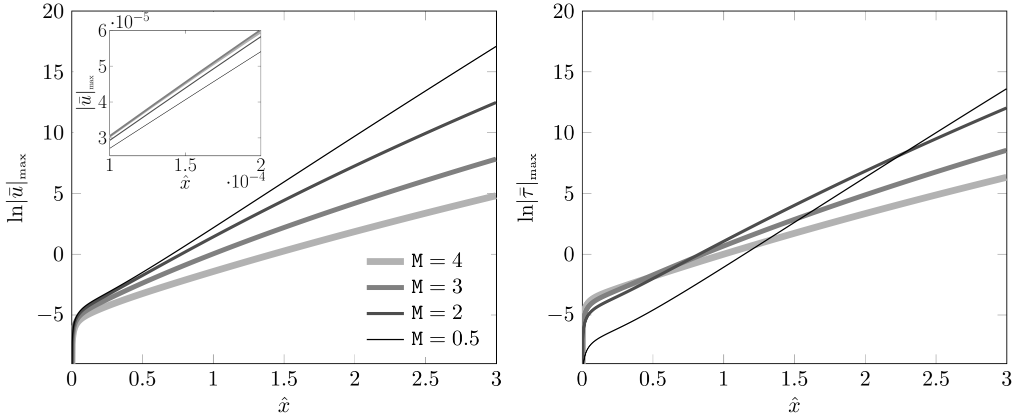

Figure 6: The effect of the Mach number on the maximum streamwise velocity perturbation (left) and the maximum temperature perturbation (right) for a steady flow at $\mathtt{R} = 1273.2$, $\mathtt{G} = 206.4$ and $k_y = 1$.

most unstable Görtler vortices are therefore incompressible. However, this is true only during the initial stages of the evolution as the recent experimental study by Wang *et al.* (2018) showed that transition to turbulence is achieved more rapidly for compressible Görtler vortices compared to the slower transition of incompressible Görtler vortices because the secondary instability of nonlinearly evolving vortices is more intense in the compressible case.

In addition to $\mathtt{G_V}$-vortices, compressibility effects generate thermal Görtler vortices, hereinafter called $\mathtt{G_T}$-vortices. They originate due to the velocity-temperature coupling within the boundary layer even in the absence of free-stream temperature disturbances, similar to the thermal Klebanoff modes over a flat plate (Ricco & Wu 2007). Figure 6 (right) reveals that the temperature perturbations also grow exponentially and are more stable sufficiently downstream, i.e., their growth rate decreases, as the Mach number increases. However, thanks to our receptivity framework we notice that in the proximity of the leading edge, where δ^* is smaller than λ_z^*, the temperature perturbations increase much more significantly with the Mach number than the velocity perturbations. We further note that the stabilizing effect of the Mach number occurs much further upstream for the $\mathtt{G_V}$-vortices than for the $\mathtt{G_T}$-vortices. Since further downstream the growth rate decreases with increasing Mach number, temperature perturbations for lower Mach number become dominant when $\hat{x}$ is sufficiently high. This reversed influence of compressibility caused by the growing presence of spanwise viscous diffusion along the streamwise direction was also detected on thermal Klebanoff in the presence of wall heat transfer (Ricco *et al.* 2009). None of the previous theoretical frameworks could trace the evolution of the velocity and the temperature perturbations from the leading edge and observe this effect of spanwise diffusion because local EV approaches were utilized without considering the influence of the base-flow receptivity to external disturbances on the evolution of the Görtler vortices.

The location of the maximum value of the perturbation amplitude is monitored to evince the wall-normal position of the Görtler vortices. Early studies by Kobayashi & Kohama (1977), El-Hady & Verma (1983), and Ren & Fu (2015) show that the vortices lift away from the wall as the Mach number increases, although through EV approaches they could not trace the evolution of the vortices from the leading edge because the

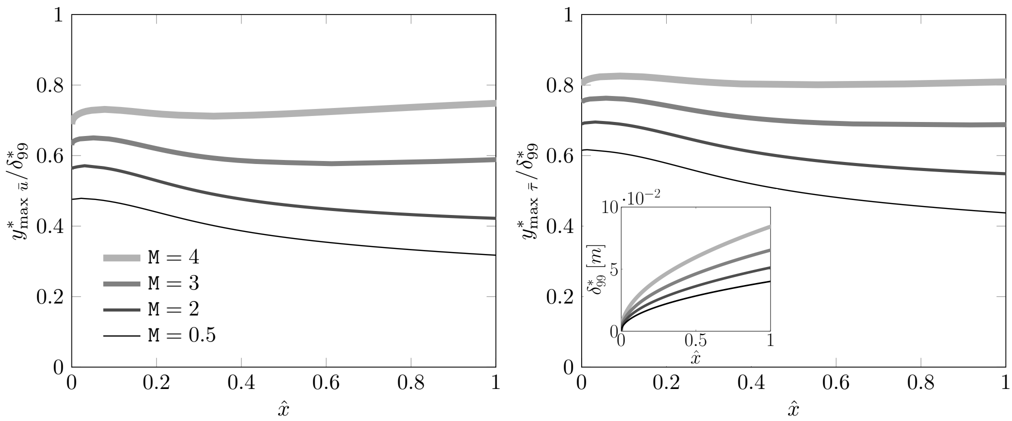

Figure 7: The effect of the Mach number on the wall-normal location of $\mathtt{G_V}$-vortices (left) and $\mathtt{G_T}$-vortices (right) for a steady flow at $\mathtt{R} = 1273.2$, $\mathtt{G} = 206.4$ and $k_y = 1$. Inset: Boundary-layer thickness based on $\lambda_z^* = 8 \cdot 10^{-3}$m.

external forcing due to the free-stream disturbances plays a crucial role there. This effect of compressibility on Görtler vortices was also noticed by Spall & Malik (1989), Hall & Fu (1989), and Wadey (1992). Previous studies have shown that in the limit of large Mach number the vortices move into a log-layer near the free stream. However, as we focus on $\mathtt{M} = \mathcal{O}(1)$, this lifting effect of the Mach number is not intense enough and the vortices are confined in the core of the boundary layer. Thanks to our receptivity framework, we can follow the wall-normal location of the $\mathtt{G_V}$-vortices and the $\mathtt{G_T}$-vortices as they evolve from the leading edge. Figure 7 confirms that by increasing the Mach number the $\mathtt{G_V}$-vortices (left) and the $\mathtt{G_T}$-vortices (right) occur at larger wall-normal locations. The influence of Mach number is stronger on the $\mathtt{G_V}$-vortices than on the $\mathtt{G_T}$-vortices and the $\mathtt{G_T}$-vortices are positioned closer to the free stream than the $\mathtt{G_V}$-vortices. The increase of boundary-layer thickness δ^*_{99} with the Mach number is also shown in the inset of Figure 7 (right).

As shown by Hall (1983) and Wu *et al.* (2011), incompressible Görtler vortices move closer to the surface as they evolve downstream and they become confined in the wall layer region. This behavior persists in the compressible regime as long as $\mathtt{M} < 3$. For $\mathtt{M} \geqslant 3$ the vortices are not confined near the wall but they evolve in the core of the boundary layer. The asymptotic results of stage III, based on the assumption $\mathtt{G} \gg 1$, cannot capture this behavior because vortices tend to shift towards the wall as $\mathtt{G}$ increases for any Mach number when $\mathtt{M} = \mathcal{O}(1)$.

Figure 8 shows the streamwise velocity perturbation profiles (left) and the spanwise velocity perturbation profiles (right) for $\mathtt{M} = 2$ and $\mathtt{M} = 4$. Both the streamwise and the spanwise velocity profiles show that the perturbations move towards the wall for $\mathtt{M} = 2$ and remain confined in the boundary-layer core for $\mathtt{M} = 4$. For this higher Mach number, the velocity gradient at the wall tends to zero as $\hat{x}$ increases, generating a near-wall region where the flow is largely unperturbed. Consequently, for $\mathtt{M} > 3$ the wall-shear stress of the perturbation is not a sound indicator for the growth of thermal Görtler vortices, while it is effective in the incompressible regime (Hall 1983, 1990). Temperature profiles behave similarly to the streamwise velocity profiles and their peak shifts slightly towards the free stream (not shown).

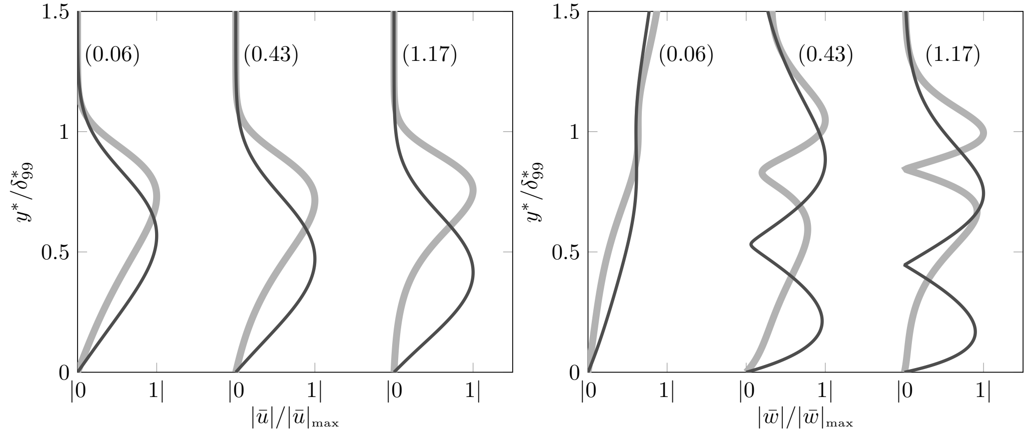

Figure 8: Influence of the Mach number, $\mathtt{M} = 2$ (—) and $\mathtt{M} = 4$ (—), on the normalized profiles of the streamwise velocity perturbation (left) and the spanwise velocity perturbation (right) for a steady flow at $\mathtt{R} = 1273.2$, $\mathtt{G} = 206.4$ and $k_y = 1$. Numbers in the parenthesis correspond to the streamwise location $\hat{x}$.

	$\mathtt{M} = 0$	$\mathtt{M} = 0.5$	$\mathtt{M} = 2$	$\mathtt{M} = 3$	$\mathtt{M} = 4$
$\mathtt{G} = 206.4$	0.083	0.083	0.08	0.095	0.099
$\mathtt{G} = 412.8$	0.052	0.052	0.048	0.049	0.053
$\mathtt{G} = 825.6$	0.033	0.033	0.031	0.031	0.032

Table 2: Streamwise locations $\hat{x}_\beta$ for different values of the Görtler number and the Mach number for a steady flow with $\mathtt{R} = 1273.2$ and $k_y = 1$.

4.1.2. *Effect of Görtler number*

In the context of steady vortices, we now analyze the effect of the Görtler number on the evolution of perturbations for $\mathtt{M} = 2$ and $\mathtt{M} = 4$. Keeping $\mathtt{R} = 1273.2$, radii of curvature $r^* = 5$m and $r^* = 10$m give $\mathtt{G} = 412.8$ and $\mathtt{G} = 206.4$, respectively.

The evolution of the perturbation is characterized by the parameter $\beta(\hat{x}) \equiv \mathrm{d}^2|\bar{u}(\hat{x})|_{\max}/\mathrm{d}\hat{x}^2$ (Viaro & Ricco 2018). Klebanoff modes, for which $\beta < 0$ due to their algebraic growth, first develop near the leading edge. When curvature effects become important the Klebanoff modes turn into Görtler vortices at a streamwise location $\hat{x}_\beta$ where $\beta = 0$ and starts growing with $\beta > 0$. The effect of the Görtler and Mach numbers on $\hat{x}_\beta$ is shown in table 2. The location $\hat{x}_\beta$ decreases as the Görtler number increases for all the Mach numbers and for subsonic conditions there is no Mach number influence. For supersonic conditions and low enough Görtler number, $\hat{x}_\beta$ increases with the Mach number, but $\hat{x}_\beta$ becomes independent of the Mach number in supersonic conditions if the Görtler number is sufficiently large.

Klebanoff modes contribute to the initial growth of the perturbation and, for sufficiently small Görtler numbers, i.e., $\mathtt{G} < 50$ for $\mathtt{M} = 4$, they stabilize after a certain streamwise location, as shown in figure 9. Only when $\mathtt{G}$ is large enough the instability is characterized by the more energetic Görtler vortices. This is confirmed by the recent

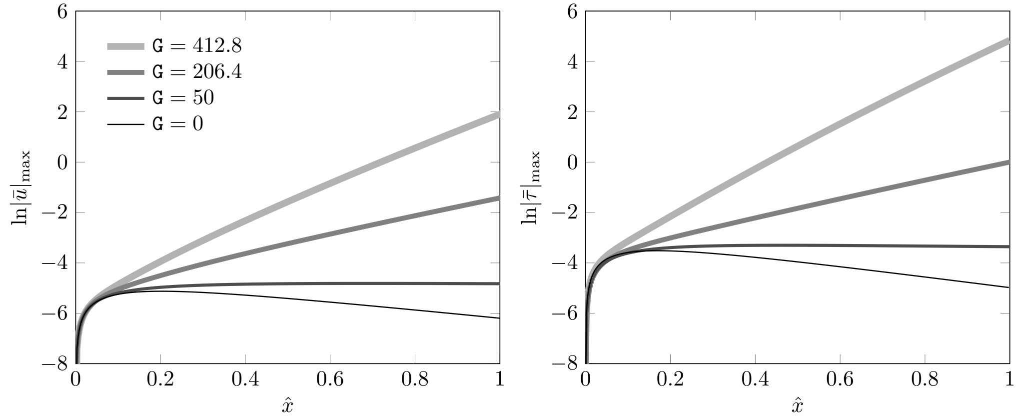

Figure 9: The effect of the Görtler number $\mathtt{G}$ on the maximum streamwise velocity perturbation (left) and temperature perturbation (right) for a steady flow with $\mathtt{M} = 4$, $\mathtt{R} = 1273.2$ and $k_y = 1$.

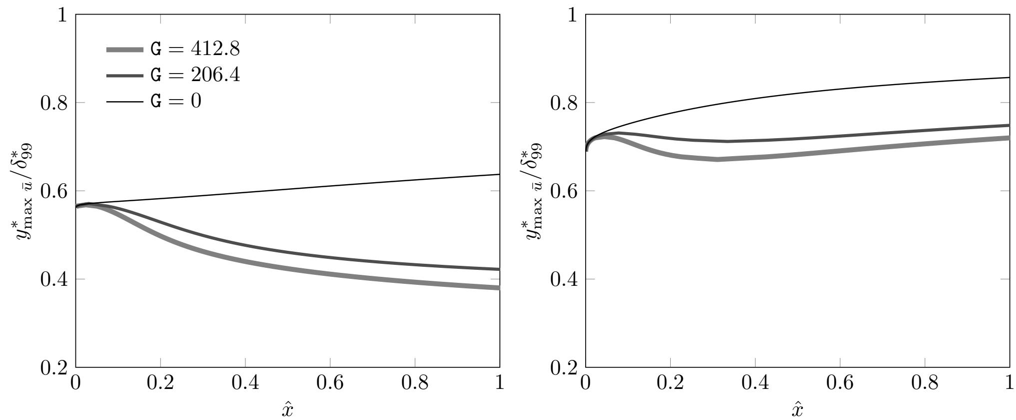

Figure 10: The effect of the Görtler number $\mathtt{G}$ on the wall-normal location of $\mathtt{G_V}$-vortices at $\mathtt{M} = 2$ (left) and $\mathtt{M} = 4$ (right) for a steady flow with $\mathtt{R} = 1273.2$ and $k_y = 1$.

experimental study of Wang *et al.* (2018) where for low $\mathtt{G}$ values only weak streaky structures are present and the centrifugal instability is detected only at higher Görtler numbers. Figure 9 also shows that, as the Görtler number increases, $\mathtt{G_T}$-vortices (right) are more unstable than $\mathtt{G_V}$-vortices (left) at $\mathtt{M} = 4$.

The location of $\mathtt{G_V}$-vortices is shown in figure 10 for $\mathtt{M} = 2$ (left) and $\mathtt{M} = 4$ (right). When the Görtler number increases the vortices move closer to the wall whereas when the Mach number grows they move away from the wall. High Mach number flows tend to behave more similarly to the flat-plate scenario.

The influence of the Mach number changes as the Görtler number increases. The asymptotic analysis reveals that for $\mathtt{G} \gg 1$ an increase of the Mach number makes the vortices move towards the wall. This was also noticed by Dando & Seddougui (1993) and it is confirmed by the LUBR results for high Görtler numbers. Table 3 schematically shows that, when $\hat{x}$ is held fixed and the subsonic or mildly supersonic Mach number increases, the vortices shift towards the boundary-layer core only when $\mathtt{G} = \mathcal{O}(1)$. In

$\mathtt{M}$	$\mathtt{G}$	$\hat{x}$	Vortex dynamics
$\approx 1 \uparrow$	$\mathcal{O}(1)$	$\mathcal{O}(1)$	$\rightarrow$ boundary-layer core
$\approx 1 \uparrow$	$\gg 1$	$\mathcal{O}(1)$	$\rightarrow$ wall
≈ 1	$\uparrow$	$\mathcal{O}(1)$	$\rightarrow$ wall
< 3	$\mathcal{O}(1)$	$\mathcal{O}(1) \uparrow$	$\rightarrow$ wall
$\geqslant 3$	$\mathcal{O}(1)$	$\mathcal{O}(1) \uparrow$	$\rightarrow$ boundary-layer core

Table 3: Influence of $\mathtt{G}$, $\mathtt{M}$, and $\hat{x}$ on the location of the Görtler vortices. Upward arrows ($\uparrow$) indicate increasing values and horizontal arrows ($\rightarrow$) denote the vortices moving towards the wall or the boundary-layer core.

addition, the position of the vortices as $\hat{x}$ increases is affected by the Mach number being smaller or larger than 3 for $\mathtt{G} = \mathcal{O}(1)$, as shown in figure 7.

Figure 11 (top) shows the streamwise velocity and temperature perturbation profiles at different streamwise locations. These profiles highlight the unperturbed near-wall regions for $\mathtt{M} = 4$ caused by the $\mathtt{G}_\mathtt{V}$-vortices and the $\mathtt{G}_\mathtt{T}$-vortices moving towards the free stream. The peaks in the profiles experience only a minor shift towards the wall as the Görtler number increases due to the high Mach number. Like for the Mach number effects, the influence of the Görtler number increases as the solution evolves downstream. The wall-normal velocity perturbation and the spanwise velocity perturbation represent the weak crossflow of the Görtler instability. These profiles, shown in figure 11 (bottom) for different values of $\mathtt{G}$, demonstrate that even though the free-stream vortical disturbance decreases exponentially in the streamwise direction, as described by (2.16) and (2.17), the perturbations inside the boundary layer soon become self-sustained when curvature effects become significant. The wall-normal velocity profiles present a single peak at $\eta \approx 2$ whereas the spanwise velocity profiles, which are more affected by $\mathtt{G}$, show the double-peak characteristic of the longitudinal counter-rotating $\mathtt{G}_\mathtt{V}$-vortices. As in the case of the streamwise perturbation velocity, the solution for $\hat{x} = 0.06$ differs only slightly from the flat plate one, proving that the influence of curvature is still weak. The confinement of the $\mathtt{G}_\mathtt{V}$-vortices for into the core of the boundary layer is also visible from the crossflow velocity profiles of figure 11 (bottom).

Previous studies have investigated how changes of the Görtler number affect the solution as the Mach number increases. The EV approach of El-Hady & Verma (1983) demonstrates that Görtler vortices are more sensitive to changes in the Görtler number as the Mach number grows. On the contrary, we show that Görtler vortices are less sensitive to changes in the curvature as the Mach number increases (e.g., refer to figure 10), which is in agreement with the results of Spall & Malik (1989).

4.1.3. *Effect of the free-stream wavelength ratio*

The effect of the free-stream wavelength ratio $k_y = \lambda_z^*/\lambda_y^*$ can only be studied through the receptivity formalism because k_y only appears in the initial and free-stream boundary conditions, i.e., equations (2.20)-(2.24) and (2.14)-(2.19), respectively. Figure 12 shows the effect of k_y on the streamwise perturbation velocity (left) and the wall-normal location of the $\mathtt{G}_\mathtt{V}$-vortices (right) for $\mathtt{M} = 4$ and $\mathtt{G} = 206.4$. The weak effect of k_y increases at higher Mach numbers (not shown). The flow becomes slightly more stable as k_y increases, with

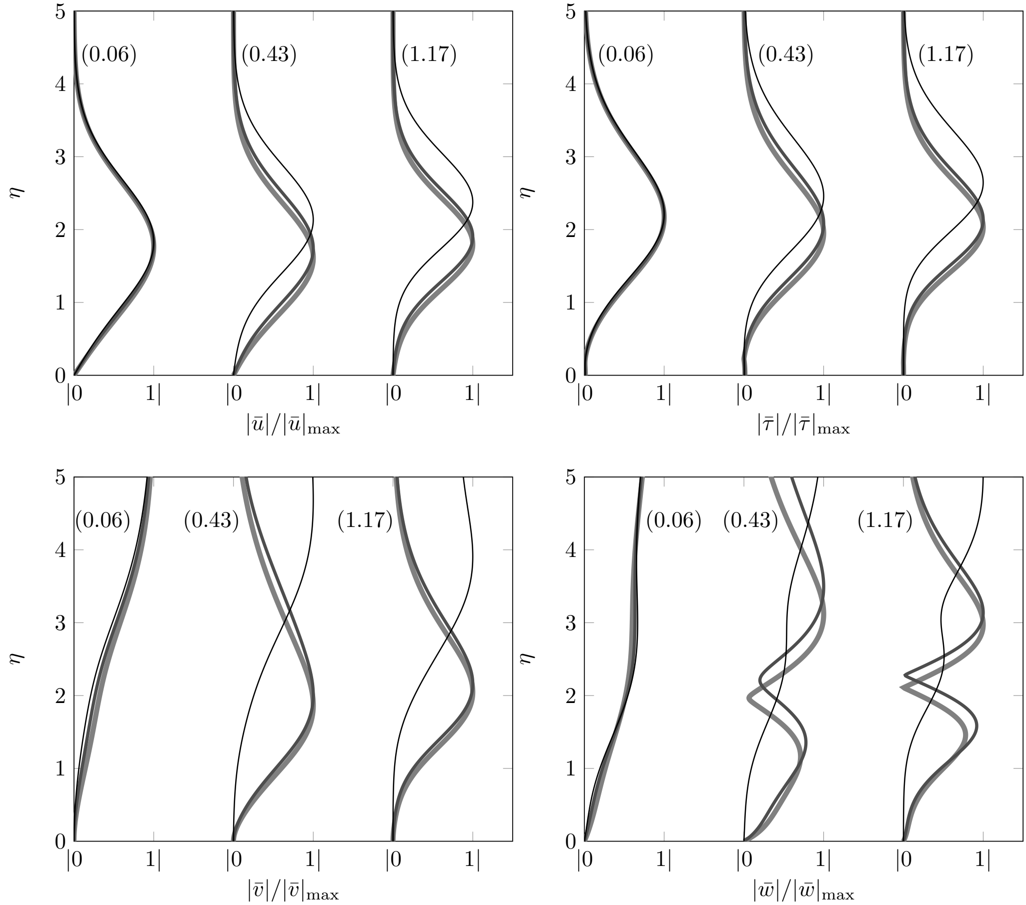

Figure 11: The effect of the Görtler number G, $G = 0$ (—), $G = 206.4$ (━) and $G = 412.8$ (━), on the normalized profiles of the streamwise velocity perturbation (top left), the temperature perturbation (top right), the wall-normal velocity perturbation (bottom left) and the spanwise velocity perturbation (bottom right) for a steady flow at $R = 1273.2$, $M = 4$ and $k_y = 1$. Numbers in the parenthesis correspond to the streamwise location $\hat{x}$.

the most unstable configuration achieved for $k_y = 0$. The growth rate of the streamwise velocity becomes nearly constant for sufficiently high $\hat{x}$. When the flow is more stable as k_y increases, the vortices initially tend to shift towards the wall but their wall-normal position becomes independent on k_y at sufficiently high values of $\hat{x}$, as shown in figure 12 (right). Contrary to the effect of Mach number and Görtler number, the influence of k_y on the wall-normal position of the vortices decreases as the streamwise location increases. Spall & Malik (1989) also noted that, for different initial conditions, the growth rates converged at sufficiently high scaled wavenumbers, i.e., sufficiently downstream, and that this convergence occurs closer to the leading edge as the Görtler number increases. The normalized streamwise velocity and the temperature profiles experience no significant variations as k_y changes whereas the profiles of the crossflow velocities vary with k_y but only at small streamwise locations (not shown).

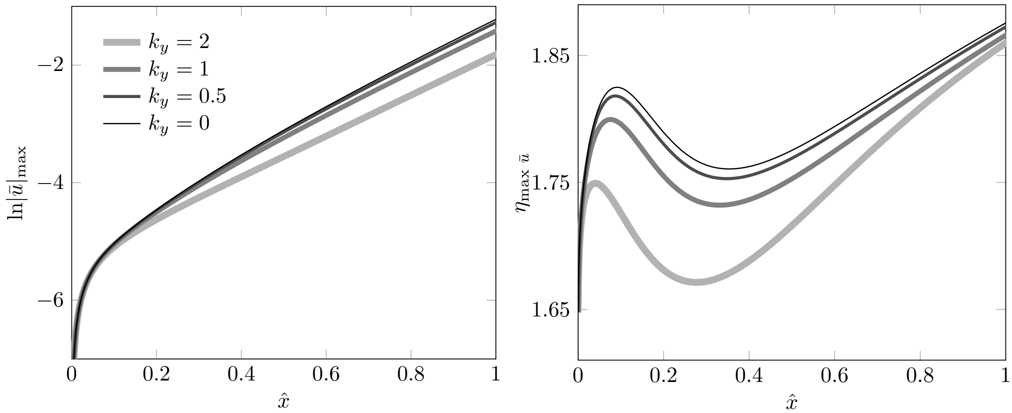

Figure 12: The effect of k_y on the maximum streamwise velocity perturbation (left) and wall-normal location of $\mathtt{G_V}$-vortices (right) for a steady flow at $\mathtt{R} = 1273.2$, $\mathtt{G} = 206.4$ and $\mathtt{M} = 4$.

4.1.4. *Effect of frequency*

The effect of frequency at two different Mach numbers, $\mathtt{M} = 0.5$ and $\mathtt{M} = 3$, is investigated by keeping a constant dimensionless wavenumber $\kappa = k_z/(k_x\mathtt{R})^{1/2} = \mathcal{O}(1)$ that, for $\hat{x} = \mathcal{O}(1)$, is representative of the ratio $\delta^*/\lambda_z^* = \mathcal{O}(1)$, i.e., the spanwise and the wall-normal diffusion effects are comparable. Flows at different Görtler numbers are also compared for $r^* = 5$m and $r^* = 10$m. For the subsonic case the Görtler numbers are $\mathtt{G} = 2494.7$ and $\mathtt{G} = 1247.3$, whereas, for the supersonic case, $\mathtt{G} = 479.4$ and $\mathtt{G} = 239.7$, respectively. The frequency is scaled as

$$\mathtt{F} \equiv \frac{f^*}{\mathtt{R}_u^*\, U_\infty^*}, \tag{4.1}$$

where the unit Reynolds numbers are $\mathtt{R}_u^* = 11 \cdot 10^6$ m^{-1} and $\mathtt{R}_u^* = 2.18 \cdot 10^6$ m^{-1} for a subsonic case (Flechner *et al.* 1976) and a supersonic case (Graziosi & Brown 2002), respectively. For each Mach number, the effect of frequency is studied by doubling and halving a reference frequency from wind tunnel experiments for supersonic and subsonic flows. At $\mathtt{M} = 3$, the reference frequency $f^* = 1000$Hz ($\mathtt{F} = 7.5 \cdot 10^{-7}$) comes from the work of Graziosi & Brown (2002), which corresponds to the maximum perturbation energy. Given that no experiments were found for $\mathtt{M} = 0.5$, the reference frequency $f^* = 250$Hz ($\mathtt{F} = 1.32 \cdot 10^{-7}$) was inferred from the knowledge of frequencies at very low Mach numbers (Boiko *et al.* 2010*b*), $f_{\max}^* \approx 20$Hz, and at high Mach numbers (Graziosi & Brown 2002), $f_{\max}^* \approx 10$kHz. This value additionally allows us to compare the same frequency, $f^* = 500$Hz, in the two Mach numbers considered. The parameters used to investigate the effect of frequency are summarized in table 4, along with the estimation of the boundary-layer displacement thickness $\delta_c^* = \delta_i^* + 1.192(\gamma - 1)\mathtt{M}^2 x_{\max}^*/\mathtt{R}^{0.5}$ (Stewartson 1964), where δ_i^* is the displacement thickness for incompressible flows and $x_{\max}^* = 2$m.

Figure 13 shows the stabilizing effect of increasing the frequency on the temperature perturbation while keeping a constant radius of curvature $r^* = 5$m. The stabilizing influence of doubling the reference frequencies is more intense compared to the destabilizing effect of halving them, for both Mach numbers and for $r^* = 10$m (not shown). The same conclusions can be drawn for the maximum velocity perturbation $|\bar{u}(\hat{x})|_{\max}$, which also agree with the findings of Hall (1990) and Ren & Fu (2015).

Frequency plays an important role on the location of Görtler vortices. As the main

M	G	f^* [Hz]	$\mathtt{F} \cdot 10^{-7}$	λ_z^* [m]	R	$k_x \cdot 10^{-5}$	κ	δ_c^* [m]
		125	0.66			215	0.3000	
0.5	1247.3 — 2494.7	250	**1.32**	0.0029	5157.51	430	**0.2125**	0.002
		500	2.64			860	0.1503	
		500	3.75			640	0.3000	
3	239.7 — 479.4	1000	**7.49**	0.005	1735.66	1280	**0.2125**	0.009
		2000	14.98			2560	0.1503	

Table 4: Flow parameters from wind tunnel data used for the analysis of the unsteady Görtler instability at $r^* = 5$m and $r^* = 10$m. Reference cases are in bold.

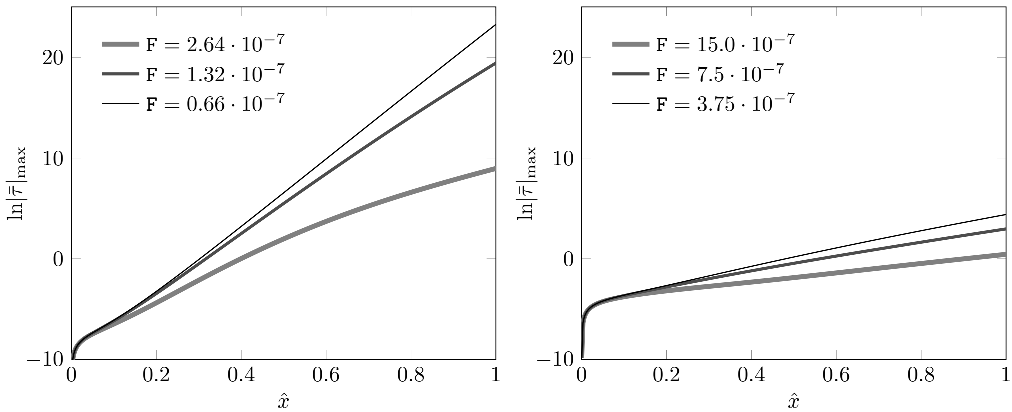

Figure 13: The effect of the frequency F on the maximum temperature perturbation for a plate with $r^* = 5$m and $k_y = 1$, at $\mathtt{M} = 0.5$, $\mathtt{G} = 2494.7$ (left) and $\mathtt{M} = 3$, $\mathtt{G} = 479.4$ (right).

effect of increasing the frequency is to move the vortices away from the wall, figure 14 (left) shows that, even for low Mach numbers, $\mathtt{G_T}$-vortices are not confined near the wall if the frequency is high enough. At high Mach numbers, the effect of frequency on the location of $\mathtt{G_T}$-vortices is more intense and starts closer to the leading edge, as shown in figure 14 (right). $\mathtt{G_V}$-vortices are located closer to the wall with a weaker dependence on the frequency than $\mathtt{G_T}$-vortices (not shown).

To summarize, Görtler vortices tend to move towards the boundary-layer core when the perturbation is more stable, i.e., as F or M increase, or G decreases. As k_y increases, the perturbation is slightly more stable and Görtler vortices tend to move closer to the wall.

4.1.5. *Growth rate and streamwise length scale of the perturbation*

From the solution of the LUBR equations, the streamwise velocity of the perturbation $\bar{u} = \bar{u}(\hat{x}, \eta)$ can be used to compute the complex parameter $\sigma = \sigma_{\mathrm{Re}} + i\, \sigma_{\mathrm{Im}}$ as

$$\sigma(\hat{x}, \eta) = \left. \frac{1}{\bar{u}} \frac{\partial \bar{u}}{\partial \hat{x}} \right|_{\eta}, \tag{4.2}$$

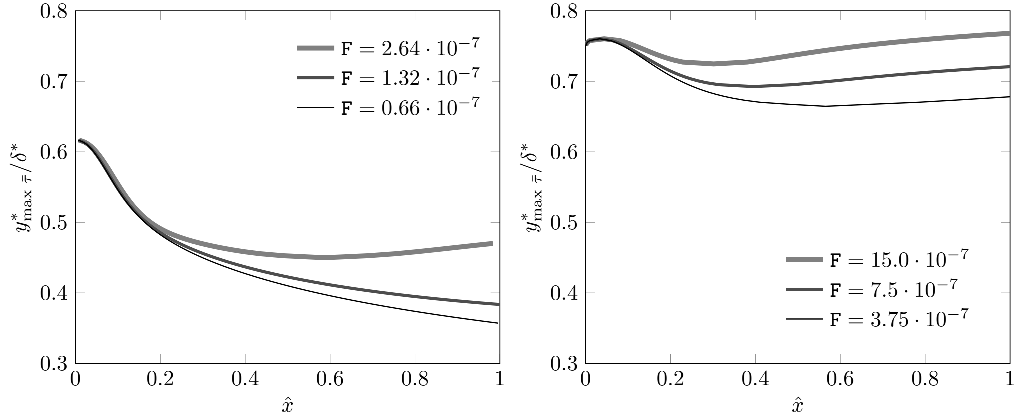

Figure 14: The effect of the frequency F on the wall-normal location of $\mathtt{G_T}$-vortices for a plate with $r^* = 5$m and $k_y = 1$, at $\mathtt{M} = 0.5$, $\mathtt{G} = 2494.7$ (left) and $\mathtt{M} = 3$, $\mathtt{G} = 479.4$ (right).

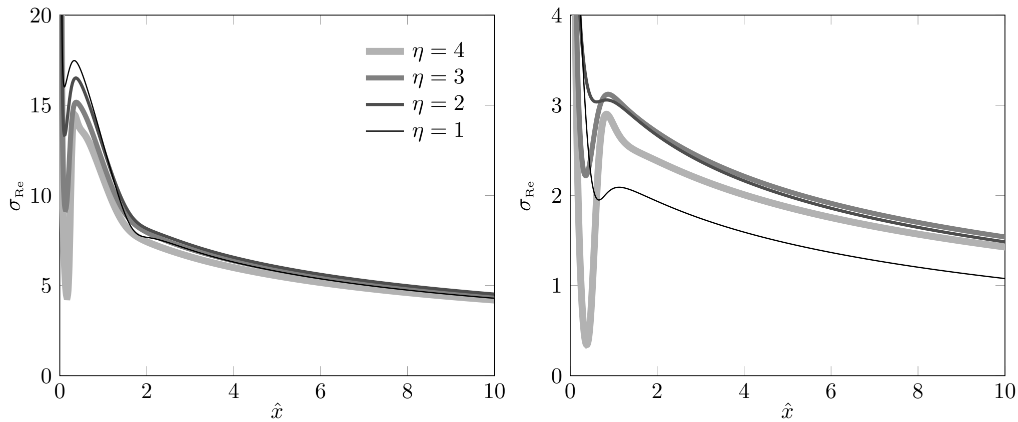

Figure 15: Influence of η on $\sigma_{\mathrm{Re}}(\hat{x}, \eta)$ for $\mathtt{M} = 0.5$, $\mathtt{G} = 1247.3$, $k_y = 1$, $\mathtt{F} = 1.32 \cdot 10^{-7}$ (left) and $\mathtt{M} = 3$, $\mathtt{G} = 239.7$, $k_y = 1$, $\mathtt{F} = 7.5 \cdot 10^{-7}$ (right).

where σ_{Re} is the growth rate and σ_{Im} is proportional to the inverse of the streamwise length scale. In the EV framework, applying the decomposition (2.25) to (4.2) gives $\sigma = \sigma_{\mathrm{EV}}(\hat{x})$. However, figure 15 shows that the perturbation inside the boundary layer grows at different rates at different wall-normal locations η, with the maximum growth rate located at $\eta \approx 2$. The dependence on η is more intense closer to the leading edge and decreases at large $\hat{x}$, but, even at large $\hat{x}$ this effect is still not negligible, especially in supersonic conditions. The relative difference $\Delta\sigma_{\mathrm{Re}}$ between the maximum and minimum value of $\sigma_{\mathrm{Re}}(\hat{x}, \eta)$ at $\hat{x} = 10$, i.e., $\Delta\sigma_{\mathrm{Re}} = (\sigma_{\mathrm{Re,max}} - \sigma_{\mathrm{Re,min}})/\sigma_{\mathrm{Re,max}}$, is $\Delta\sigma_{\mathrm{Re}} = 7.2\%$ and $\Delta\sigma_{\mathrm{Re}} = 29.9\%$ for $\mathtt{M} = 0.5$ and $\mathtt{M} = 3$, respectively. This is confirmed by figure 15 (right) where the perturbation closest to the wall displays the lowest growth rate.

The imaginary part of (4.2), $\sigma_{\mathrm{Im}}(\hat{x}, \eta)$, can be used to define the streamwise length scale of the boundary-layer perturbation as

$$\lambda_{x,\mathrm{bl}}(x, \eta) \equiv \frac{2\pi\mathtt{R}}{\sigma_{\mathrm{Im}}(\hat{x}, \eta)}, \tag{4.3}$$

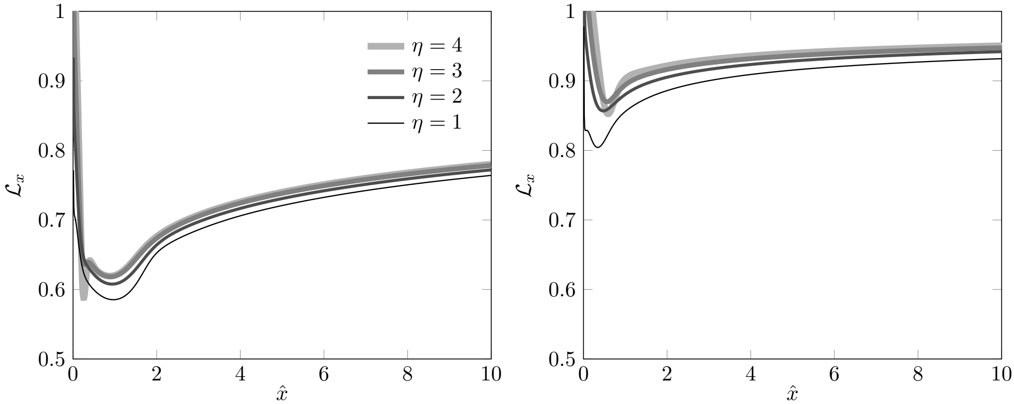

Figure 16: Influence of η on $\mathcal{L}_x(x, \eta)$ for $\mathtt{M} = 0.5$, $\mathtt{G} = 1247.3$, $k_y = 1$, $\mathtt{F} = 1.32 \cdot 10^{-7}$ (left) and $\mathtt{M} = 3$, $\mathtt{G} = 239.7$, $k_y = 1$, $\mathtt{F} = 7.5 \cdot 10^{-7}$ (right).

which, as shown schematically in figure 1, is linked through receptivity to λ_x, the constant streamwise wavelength of the free-stream disturbance. The parameter

$$\mathcal{L}_x(x, \eta) \equiv \frac{\lambda_{x,\mathrm{bl}}}{\lambda_x} = \frac{k_x \, \mathtt{R}}{\sigma_{\mathrm{Im}}(\hat{x}, \eta)} \tag{4.4}$$

can therefore be defined. Figure 16 shows the dependence of $\mathcal{L}_x$ on η for $\mathtt{M} = 0.5$ (left) and for $\mathtt{M} = 3$ (right). For all cases considered $\mathcal{L}_x < 1$, which means that the streamwise boundary-layer length scale is always smaller than the streamwise free-stream wavelength. The ratio decreases with $\hat{x}$ near the leading edge, but then increases as the perturbation evolves, i.e., $\lambda_{x,\mathrm{bl}}$ approaches λ_x further downstream. As the Mach number increases $\mathcal{L}_x$ becomes closer to unity, as shown in figure 16 (right). Increasing the frequency also has the same effect (not shown). Therefore, the more unstable the perturbation is, the more $\lambda_{x,\mathrm{bl}}$ differs from λ_x.

4.2. *Comparison with results from the eigenvalue analysis*

We now compare the LUBR solution with the solutions of the parallel and non-parallel EV equations.

4.2.1. *Growth rate and streamwise length scale of the boundary-layer perturbation*

Figure 17 shows the comparison between the growth rate (left) and the streamwise length scale ratio (right) of the LUBR solution and EV solution. The most important point is that the receptivity process selects the most unstable modes, which, in the limit $\mathtt{G} \gg 1$, correspond to the first eigenvalues of table 1. The non-parallel EV solution (solid circles) is a better approximation for the growth rate and the streamwise length scale than the parallel EV solution (empty circles) at $\eta = 2$, where the growth rate is at its maximum. The parallel and non-parallel EV formulations show the strongest disagreement with the receptivity LUBR solution closer to the leading edge, where the solution has not yet acquired a modal form. In this region, the non-parallel effects and the initial and free-stream boundary conditions thus play a key role in the dynamics of the perturbation. In the limit $\hat{x} \to 0$ the EV solution is invalid, with the growth rate becoming negative. Results show a tendency of the EV approach to overestimate the growth rate, which is in agreement with the results of Spall & Malik (1989). The agreement between the LUBR solution and the parallel EV solution is worse in the supersonic case than in

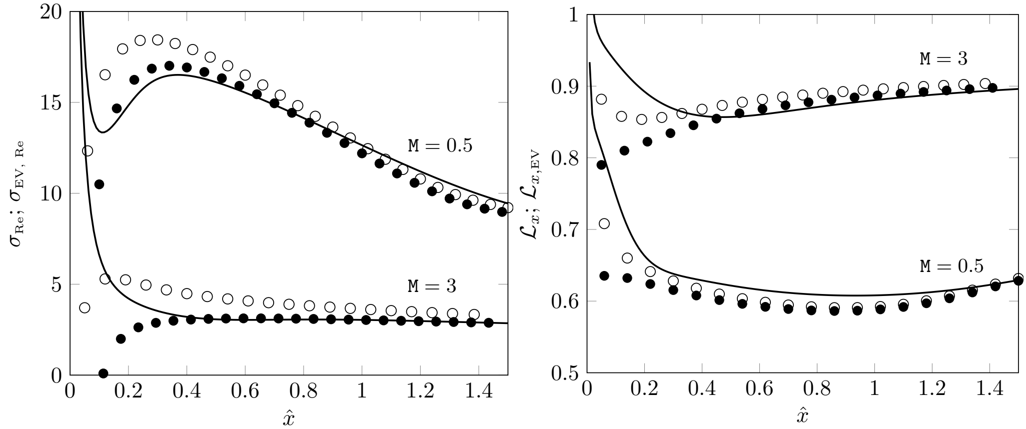

Figure 17: Comparison between the LUBR $\sigma_{\mathrm{Re}}(\hat{x},\eta)$ (——) at $\eta = 2$, the non-parallel EV $\sigma_{\mathrm{EV,\ Re}}(\hat{x})$ (●), and the parallel EV $\sigma_{\mathrm{EV,\ Re}}(\hat{x})$ (○) (left) and comparison between the LUBR $\mathcal{L}_x(\hat{x},\eta)$ (——) at $\eta = 2$, the non-parallel EV $\mathcal{L}_{x,\mathrm{EV}}(\hat{x})$ (●), and the parallel EV $\mathcal{L}_{x,\mathrm{EV}}(\hat{x})$ (○) (right), for $\mathtt{M} = 3$, $\mathtt{G} = 1247.3$, $k_y = 1$, $\mathtt{F} = 1.32 \cdot 10^{-7}$ and $\mathtt{M} = 3$, $\mathtt{G} = 239.7$, $k_y = 1$, $\mathtt{F} = 7.5 \cdot 10^{-7}$.

the subsonic case. The use of the rigorous receptivity LUBR framework becomes therefore essential to capture the entire evolution of the perturbations inside the boundary layer.

4.2.2. *Velocity and temperature profiles*

The velocity and temperature EV profiles are compared with the LUBR profiles in figure 18 for $\mathtt{M} = 3$. Since the eigenfunctions are obtained to within an arbitrary undefined constant, the solutions are normalized by the maximum values at each streamwise location to be compared with the LUBR solutions. The non-parallel EV solution approximates the profiles well for sufficiently high $\hat{x}$. Under the parallel flow approximation, the maximum of the perturbation is slightly shifted upwards and the solution is overestimated in the region above the maximum, especially near the leading edge, where the non-parallel effects are most significant. As the wall is approached both the parallel and the non-parallel EV solutions agree well with the LUBR solution.

The crossflow profiles shown in figure 19 highlight the limit of the EV solution. Close to the leading edge there is a strong influence of the free-stream vortical disturbances that cannot be captured by the simplified EV framework. Therefore, a correct analysis in this region is only possible when the receptivity of the base flow to the external vortical disturbances is considered. The disagreement in the free stream is expected, but the solutions do not even match near the wall. The non-parallel EV solution begins to approximate the crossflow perturbations well only for sufficiently high $\hat{x}$. We previously demonstrated how the growth rate is not only a function of $\hat{x}$, as shown by the decomposition (2.25), but it does also change with η even for large streamwise locations. Similarly, figures 18 and 19 demonstrate that the eigensolutions are not a simple function of η but do depend on the streamwise location $\hat{x}$.

4.3. *Comparison with results from the asymptotic analysis*

The asymptotic exponents $\breve{\sigma}(\breve{x})$ in (3.42) denote the earliest growth of the Görtler vortices triggered by the external free-stream disturbances. As the instability evolves, they turn into the fully developed local eigenmodes $\sigma_{\mathrm{EV}}(\hat{x})$ of (2.25). From (3.62) the

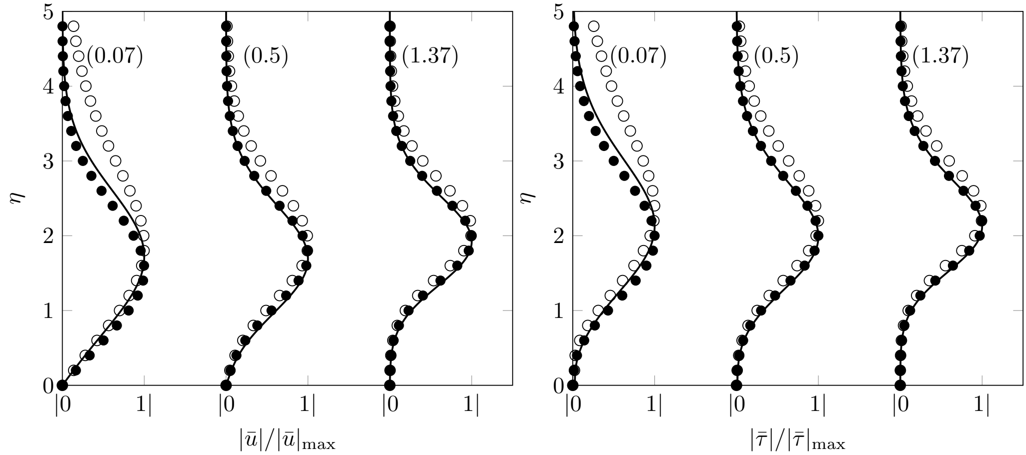

Figure 18: Comparison between the LUBR solution (——), the non-parallel EV solution (●), and the parallel EV solution (○) for the streamwise velocity profiles (left) and temperature profiles (right) at $\mathtt{M} = 3$, $\mathtt{F} = 7.5 \cdot 10^{-7}$, $\mathtt{G} = 239.73$, $k_y = 1$. Numbers in the parenthesis correspond to the streamwise location $\hat{x}$.

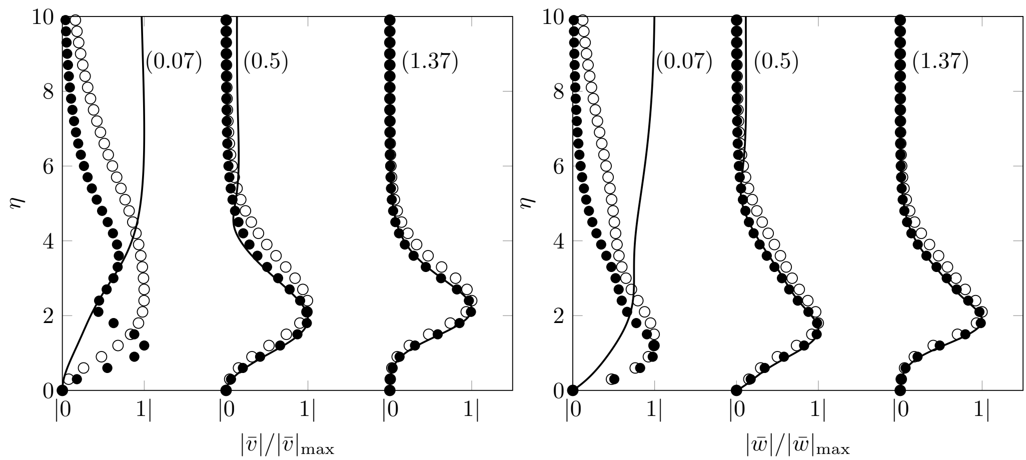

Figure 19: Comparison between the LUBR solution (——), the non-parallel EV solution (●), and the parallel EV solution (○) for the wall-normal velocity profiles (left) and spanwise velocity profiles (right) at $\mathtt{M} = 3$, $\mathtt{F} = 7.5 \cdot 10^{-7}$, $\mathtt{G} = 239.73$, $k_y = 1$. Numbers in the parenthesis correspond to the streamwise location $\hat{x}$.

streamwise velocity of the stage III solution multiplied by $\mathtt{G}^{-1/2}$ can be compared with the LUBR streamwise velocity $\bar{u}$. Figure 20 shows that the growth rate (left) and the normalized streamwise velocity LUBR profiles (right) tend to the asymptotic solution as the Görtler number increases. This is in accordance with the $\mathtt{G} \gg 1$ limit of the asymptotic analysis, although it occurs at very high Görtler and at high $\hat{x}$.

4.4. *Qualitative comparison with DNS data*

The lack of experimental data for compressible Görtler flows makes it difficult to validate our results. We here carry out a qualitative comparison with the DNS data by

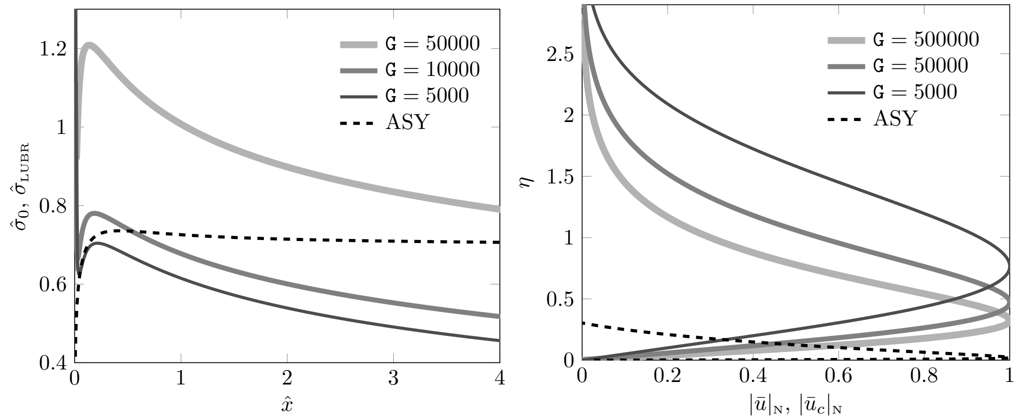

Figure 20: Comparison between the composite solution $\bar{u}_c$ from the asymptotic stage III for $\mathtt{G} = 10^{15}$ (- - -) and the LUBR results of the growth rates at $\eta = 2$ (left) and of the normalized streamwise velocity profiles at $\hat{x} = 1$ (right) for $\mathtt{M} = 3$.

Whang & Zhong (2003), who first studied the response of a hypersonic boundary layer ($\mathtt{M} = 15$) over a concave surface to free-stream vortical and acoustic disturbances. As the Mach number in their simulations is much higher than ours, quantitative agreement with our moderate supersonic data would not be possible. Nevertheless, our receptivity results are useful because they explain the physics of the instability observed by Whang & Zhong (2003). In their work, the DNS data are compared with data from the linear eigenvalue stability theory. As we have shown, this latter approach cannot fully capture the physics of the vortices, especially near the leading edge, where the effect of the free-stream perturbation is crucial.

Figure 21 presents the evolution of the amplitude of the steady streamwise and temperature perturbations obtained by Whang & Zhong (2003) (left) and by our LUBR simulations (right). Values are normalized by the first peak value of the streamwise velocity. The streamwise velocity perturbation and the temperature perturbation evolve in similar fashion, showing the initial algebraic growth due to the streaks, followed by viscous decay and by the Görtler instability downstream. These three phases have been reported by Viaro & Ricco (2018) to occur at sufficiently low Görtler number to detect a competing effect between the damping action of the viscous effects and the centrifugal instability. Consistently with our results on the effect of Mach number, the temperature perturbations become larger and larger than the velocity perturbations as the Mach number grows.

Whang & Zhong (2003) refer to the first growing phase as an early transient growth due to leading-edge effects and correctly identify the Görtler vortices as responsible for the subsequent instability following the intermediate decay. They also point out that, according to the linear stability theory, the region near the leading edge should be stable and the growth of disturbances should be absent. All these observations match our theoretical predictions. Our eigenvalue analysis indeed predicts decay near the leading edge where instead the direct forcing from the free stream creates the transient growth. We can then describe the initial growth reported by Whang & Zhong (2003) as the thermal and kinematic Klebanoff modes, which are always present from the leading edge at every Görtler number (Viaro & Ricco 2018) and are caused by the free-stream receptivity, i.e., the continuous action of the free-stream vortical disturbances, and not only by a leading-edge effect as stated by Whang & Zhong (2003).

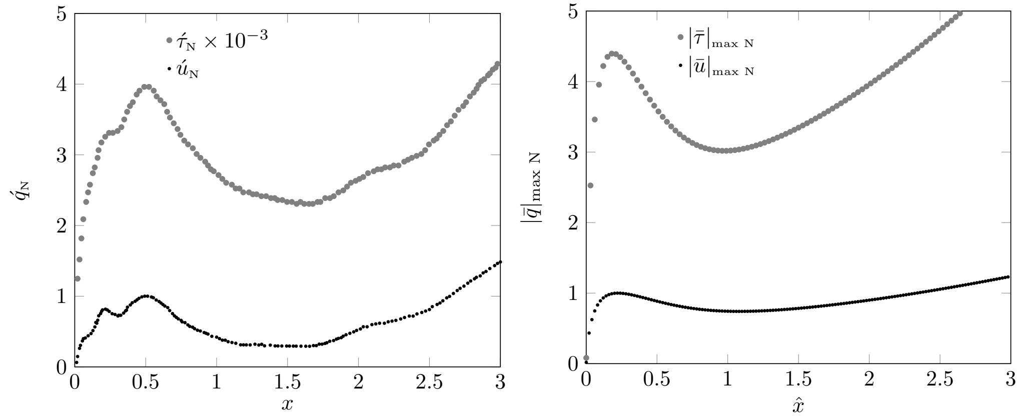

Figure 21: Comparison of velocity and temperature perturbations relative to the DNS data of Whang & Zhong (2003) at $\mathtt{M} = 15$ (left) and the LUBR results at $\mathtt{M} = 4$ (right). Data are normalized by the peak of the perturbation velocity.

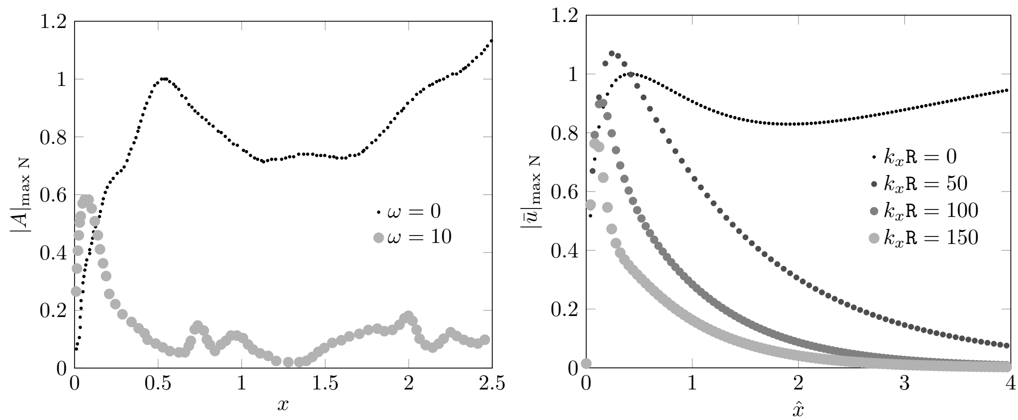

Figure 22: Comparison of the influence of frequency relative to the DNS data of Whang & Zhong (2003) at $\mathtt{M} = 15$ (left) and the LUBR results at $\mathtt{M} = 4$ (right). Data are normalized by the peak value for the steady case.

As we have shown, increasing the frequency has a stabilizing effect on the boundary-layer flow. This is consistent with the DNS results by Whang & Zhong (2003), shown in figure 22 (left) and compared with our LUBR results in figure 22 (right). For sufficiently high frequency, the Klebanoff modes do not turn into Görtler vortices downstream. For the cases presented in figure 22 only steady perturbations are subject to centrifugal instability.

5. Conclusions

For the first time, the evolution of compressible Görtler vortices over streamwise-concave surfaces triggered by small-amplitude free-stream disturbances of the gust type has been investigated. Although only kinematic perturbations exist in the free stream, the boundary layer is populated by both velocity and temperature Görtler vortices that grow significantly downstream through the inviscid unbalance between centrifugal and pressure effects.

We have solved the boundary-region equations to investigate the receptivity of the base flow to free-stream vortical disturbances and we have also adopted two eigenvalue frameworks, based on the parallel and non-parallel flow assumptions, and a high-Görtler-number asymptotic formalism, that has been revelatory of the different stages of evolution of the Görtler instability from the leading edge. We have carried out a complete parametric study on the effects of frequency, ratio of free-stream wavelengths, Mach number, and Görtler number, focusing particularly on the growth rates, streamwise length scale, and location of the velocity and temperature perturbations.

The crucial point is that both the initial conditions from the proximity of the leading edge and the outer free-stream boundary conditions are determined by the oncoming free-stream flow. This link is clearly elucidated in mathematical form in the milestone essay by Leib *et al.* (1999), from which the work by Ricco & Wu (2007) and Wu *et al.* (2011) take inspiration. It is evident from the analysis that both conditions play a cardinal role in the development and growth of the Görtler vortices. Despite the fact that the eigenvalue approach accounts neither for the initial conditions, because it is a local approximation, nor for the free-stream forcing, because it is based on an homogeneous system, it determines the growth rate and streamwise length scale of the vortices with discrete accuracy but only sufficiently downstream from the leading edge. The receptivity boundary-region solutions thus eventually match the eigenvalue solutions, which occurs when the free-stream disturbance has decayed. However, it is only through the rigorous receptivity framework that the amplitude of the Görtler vortices can be uniquely computed and linked to the amplitude of the free-stream perturbation at each streamwise location. Furthermore and arguably most importantly, the eigenvalue formulation leads to completely incorrect results not only in the very proximity of the leading edge, but also at locations comparable with the streamwise wavelength of the free-stream flow. These streamwise stations may not be close to the leading edge and only the receptivity can inform us on where the agreement between the two solutions is of good quality. This proves that the inclusion of the correct initial and free-stream forcing is essential to compute the flow from the leading edge, especially in supersonic conditions. It also means that, even if an amplitude were assigned to the eigenvalue solution in order to use it for downstream computations and thus somehow bypass the modeling of the receptivity process from the leading edge, the shape of the velocity, temperature, and pressure profiles would be incorrect. It is unknown at this stage how this mismatch may affect the subsequent computation of the nonlinear stages and of the flow breakdown to turbulence. All these considerations are of course also true for the incompressible case studied by Wu *et al.* (2011) and for the hypersonic cases at very high Mach numbers, which falls outside the scope of the present work.

The asymptotic analysis based on the limit of high Görtler number is also recipient of the same comments devoted to the eigenvalue approach, but it is an extremely powerful tool for elucidating the physics of the Görtler instability, for example for distinguishing between the inviscid core and the wall-attached thin viscous region, which together lead to the construction of an accurate semi-analytical velocity profile. This and other physical properties could only be revealed through the asymptotic approach and neither through the full receptivity boundary-region approach nor through the eigenvalue approaches. As we are driven towards both a thorough physical understanding of the flow and accurate flow computations, this trident approach has proved to be an invaluable, and arguably indispensable, tool for our receptivity study.

We of course look forward to high-quality experimental studies on compressible Görtler flows forced by free-stream vortical disturbances, for the primary intent to attain quantitative comparisons. We recognize that these laboratory endeavors are tasks of remarkable difficulty for the achievement of a specified and fully measurable free-stream flow and for accurate measurements of the velocity and temperature profiles within the boundary layer. The extension of the present work to the nonlinear case and to the secondary instability of the Görtler vortices are research avenues of utmost interest that we are going to pursue by extending the theoretical frameworks of the nonlinear thermal Klebanoff modes by Marensi *et al.* (2017) and of the secondary instability of nonlinear incompressible streaks by Ricco *et al.* (2011).

We wish to acknowledge the support of the US Air Force through the AFOSR grant FA9550-15-1-0248. We would also like to thank Dr M. E. Goldstein, Dr E. Marensi and Dr C. Alvarenga for providing insightful comments on a preliminary version of the paper. We also thank the referees for their useful comments.

This work was presented at the European turbulence conference in August 2017, the three-dimensional instability mechanisms in transitional and turbulent flows colloquia in September 2017, and the APS meeting DFD in November 2017.

Appendix A. Numerical methodology

We here describe the numerical procedures used for the two theoretical frameworks, i.e., the LUBR framework and the eigenvalue framework. Through a careful grid convergence analysis, the numerical results have been compared successfully with the results of Ricco & Wu (2007) for the compressible flow over a flat plate and of Wu *et al.* (2011) for the incompressible flow over concave surfaces.

A.1. *Boundary region framework*

The code used to solve the LUBR equations for the orthogonal curvilinear coordinate system is a modification of the code used by Ricco & Wu (2007) for a Cartesian coordinate system. The code was also modified to introduce the independent variable $\hat{x}$ instead of $\bar{x}$. The parabolic nature of the equations allows using a marching scheme. The equations (2.9)-(2.13), complemented by the boundary conditions (2.14)-(2.19) and the initial conditions (2.20)-(2.24), are solved with a second-order finite-difference scheme, central in η and backward in $\hat{x}$. In reference to figure 23, the derivatives of a fluid property $\mathbf{q}(\hat{x},\eta) = \{u, v, w, \tau\}$ are

$$\frac{\partial q}{\partial \eta} \approx \frac{q_{j+1} - q_{j-1}}{2\Delta\eta}, \qquad \frac{\partial^2 q}{\partial \eta^2} \approx \frac{q_{j+1} - 2q_j - q_{j-1}}{(\Delta\eta)^2}, \qquad \frac{\partial q}{\partial \hat{x}} \approx \frac{\frac{3}{2}q_{i,j} - 2q_{i-1,j} + \frac{1}{2}q_{i-2,j}}{\Delta\hat{x}}. \tag{A 1}$$

If the pressure is computed on the same grid as the velocity components, pressure decoupling phenomenon occurs. Therefore, the pressure is computed on a grid staggered in η as

$$p \approx \frac{p_{j+1} + p_j}{2}, \qquad \frac{\partial p}{\partial \eta} \approx \frac{p_{j+1} - p_j}{\Delta\eta}. \tag{A 2}$$

The pressure at the wall does not have to be specified and is calculated a posteriori by solving the z-momentum equation at $\eta = 0$. Due to the linearity of the equations, the system is in the form $\mathbf{Ax} = \mathbf{b}$. In a grid with N points along η, $\mathbf{A}$ is a $(N-2)\times(N-2)$ block-tridiagonal matrix where each block is a 5×5 matrix associated to the 5 unknowns $(\bar{u}, \bar{v}, \bar{w}, \bar{p}, \bar{\tau})$. Therefore, the wall-normal index j of the vectors and matrix runs from 1

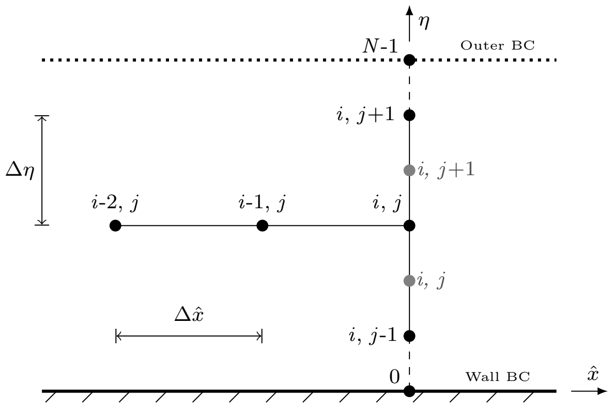

Figure 23: Sketch of the regular grid (black) and staggered grid (gray) used for the numerical scheme.

through $N-2$. The numerical procedure used to solve the linear system is found in the book of Cebeci (2002) on pages 260-264.

A.2. *Eigenvalue framework*

The eight first-order EV equations are discretized using a second-order implicit finite-difference scheme. The original homogeneous system is solved by enforcing the normalized boundary condition $\tilde{f}=1$, instead of $\tilde{u}=0$, at $\eta=0$. The initial guess for the eigenvalue $\sigma(\hat{x})$ is taken from the LUBR solution and iterated using the Newton's method until the wall boundary condition $\tilde{u}=0$ is recovered. The eigenvalue code computes the growth rate and streamwise length scale of the disturbance, along with the velocity, pressure and temperature profiles, at a specified location without starting the computation from the leading edge. It is therefore a relatively fast tool if one is interested in the local estimation of the solution. However, the eigenvalue approach requires the prior knowledge of an initial good guess that must be sufficiently close to the true solution in order for the code to converge. The sensitivity to the initial guess depends on the flow parameters, such as the Görtler number, the Mach number, the frequency, and the streamwise location. The eigenvalue approach may thus be more computationally expensive than the LUBR approach, which does not suffer from convergence issues.

Appendix B. Conditions of validity for initial and outer boundary conditions

In the analysis, the mean wall-normal velocity V is given by the compressible Blasius solution (2.7). However, at a fixed location $\hat{x}$, V tends to a constant as $\eta\to\infty$, which is nonphysical at a large wall-normal distance because the wall-normal velocity must decay to zero as the streamwise uniform flow is approached. In the outer region IV, the inviscid mean flow is correctly described by an outer streamfunction whose wall-normal velocity $V_{\text{out}}(\hat{x},y)\to 0$ as $y\to\infty$.

Therefore, the correct wall-normal velocity valid at any wall-normal location is obtained through a composite solution

$$V_{\text{c}} = V_{\text{in}} + V_{\text{out}} - V_{\text{com}}, \tag{B 1}$$

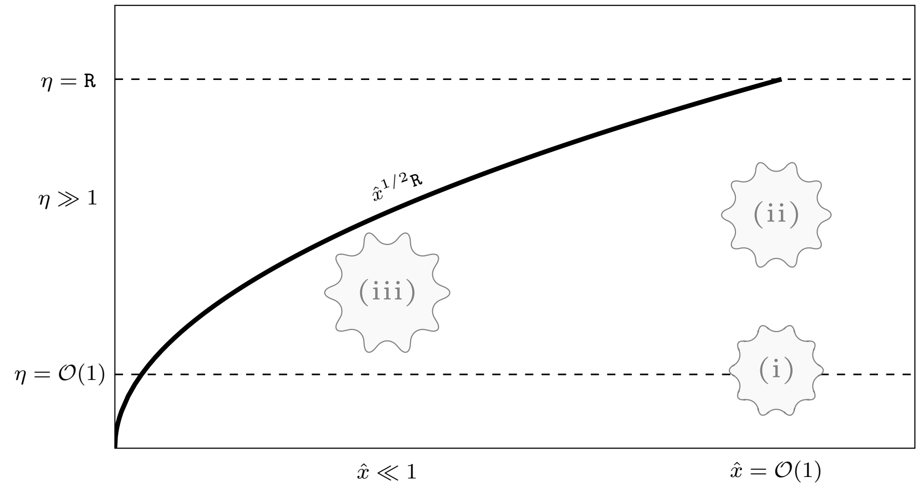

Figure 24: Regions of validity (i), (ii), (iii) of the compressible Blasius flow in the $(\hat{x}, \eta)$-plane.

where $V_{\text{in}}(\eta)$ is the compressible Blasius solution and V_{com} is the common solution

$$V_{\text{com}} = \lim_{\eta \to \infty} V_{\text{in}} = \lim_{y \to 0} V_{\text{out}}. \tag{B 2}$$

We must therefore identify the ranges of $\hat{x}$ and η for which the wall-normal velocity is rigorously represented by the Blasius velocity V_{in}, i.e., where $V_{\text{out}} \approx V_{\text{com}}$.

In $(\hat{x}, \eta)$-coordinates, the outer subsonic wall-normal mean velocity is

$$V_{\text{out}} = \frac{\phi_c}{(2\mathtt{R})^{1/2}} \,\mathfrak{Re}\left\{ \left[\underbrace{\hat{x}\mathtt{R}}_{\textcircled{1}} + \underbrace{i(2\hat{x})^{1/2}\left(1 - \mathtt{M}^2\right)^{1/2} \int_0^\eta T(\bar{\eta})\mathrm{d}\bar{\eta}}_{\textcircled{2}} \right]^{-1/2} \right\}, \tag{B 3}$$

where ϕ_c is a constant accounting for the compressibility effects and $\mathfrak{Re}$ denotes the real part. The common solution is

$$V_{\text{com}} = \frac{\phi_c}{\mathtt{R}(2\hat{x})^{1/2}}. \tag{B 4}$$

The condition $V_{\text{com}} \approx V_{\text{out}}$ translates to ranges of $\hat{x}$ and η for which, in (B 3), term $\textcircled{1}$ dominates over term $\textcircled{2}$. As the mean temperature $T(\eta) = \mathcal{O}(1)$, three cases can be distinguished for $\mathtt{R} \gg 1$:

(i) $\hat{x} = \mathcal{O}(1), \quad \eta = \mathcal{O}(1)$;

(ii) $\hat{x} = \mathcal{O}(1), \quad \eta \gg \mathcal{O}(1)$;

(iii) $\hat{x} \ll 1, \quad \eta \gg \mathcal{O}(1)$.

The condition $\textcircled{1} \gg \textcircled{2}$ is automatically satisfied for case (i), it is $1 \ll \eta \ll \mathtt{R}$ for case (ii), and $1 \ll \eta \ll \hat{x}^{1/2}\mathtt{R}$ for case (iii). These results are summarized in figure 24.

In the supersonic case, the outer mean wall-normal velocity is

$$V_{\text{out}} = \frac{\phi_c}{(2\mathtt{R})^{1/2}} \left[\underbrace{\hat{x}\mathtt{R}}_{\textcircled{1}} + \underbrace{(2\hat{x})^{1/2}\left(\mathtt{M}^2 - 1\right)^{1/2} \int_0^\eta T(\bar{\eta})\mathrm{d}\bar{\eta}}_{\textcircled{2}} \right]^{-1/2}, \tag{B 5}$$

and the conditions of validity are the same as for the subsonic case.

Appendix C. Upstream behaviour of the LUBR equations

In the limit of $\hat{x} \to 0$ the LUBR solution can be obtained analytically for $\eta = \mathcal{O}(1)$ and $\eta \to \infty$. Summing these two solutions and subtracting their common parts, i.e., the values in the region along η where both solutions are valid, we obtain the upstream perturbation profiles that are uniformly valid for all η (2.20)-(2.24). These profiles provide the initial conditions for the LUBR equations (2.9)-(2.13). Details on this analysis are found in Leib *et al.* (1999), in which the initial conditions are equivalent, after rescaling in the $(\hat{x}, \eta)$ coordinates, to the ones here summarized in the following steps:

(i) The first step consists in writing the LUBR equations in terms of the variable

$$y^{(0)} = (2\hat{x})^{1/2}(k_x \mathtt{R})^{1/2}\bar{\eta}. \tag{C 1}$$

in the limit $\eta \to \infty$. Their solution that matches with the flow in the region IV of figure 1 outside the boundary layer is (Leib *et al.* 1999)

$$\bar{u} = 0, \tag{C 2}$$

$$\bar{v} = \frac{ie^{ik_x \mathtt{R}\hat{x}}}{(2\hat{x})^{1/2}\left(k_y - i|k_z|\right)}\left[e^{ik_y(2\hat{x})^{1/2}\bar{\eta}-(k_y^2+k_z^2)\hat{x}} - e^{-|k_z|(2\hat{x})^{1/2}\bar{\eta}}\right] + \frac{|k_z|}{(2\hat{x})^{1/2}}e^{ik_x\mathtt{R}\hat{x}-|k_z|(2\hat{x})^{1/2}\bar{\eta}}\int_0^{\hat{x}} g(\breve{x})\mathrm{e}^{-ik_x\mathtt{R}\breve{x}}\mathrm{d}\breve{x}, \tag{C 3}$$

$$\bar{w} = \frac{e^{ik_x\mathtt{R}\hat{x}}}{k_y - i|k_z|}\left[k_y e^{ik_y(2\hat{x})^{1/2}\bar{\eta}-(k_y^2+k_z^2)\hat{x}} - i|k_z|e^{-|k_z|(2\hat{x})^{1/2}\bar{\eta}}\right] + k_z^2 e^{ik_x\mathtt{R}\hat{x}-|k_z|(2\hat{x})^{1/2}\bar{\eta}}\int_0^{\hat{x}} g(\breve{x})\mathrm{e}^{-ik_x\mathtt{R}\breve{x}}\mathrm{d}\breve{x}, \tag{C 4}$$

$$\bar{p} = g(\hat{x})e^{-|k_z|(2\hat{x})^{1/2}\bar{\eta}}, \tag{C 5}$$

$$\bar{\tau} = 0. \tag{C 6}$$

The limit of (C 2)-(C 6) for $\hat{x} \to 0$ represent the first part of the upstream perturbation profiles.

(ii) The second step consists in substituting the power series solution

$$\bar{\mathbf{q}}(\hat{x}, \eta) = \sum_{n=0}^{\infty}(2\hat{x})^{n/2}\left[2\hat{x}\, U_n(\eta), V_n(\eta), W_n(\eta), (2\hat{x})^{-1/2}P_n(\eta), 2\hat{x}\, T_n(\eta)\right] \tag{C 7}$$

for $\eta = \mathcal{O}(1)$ and $\hat{x} \to 0$ into the LUBR equations (2.9)-(2.13) and equating the terms of like powers of $\hat{x}$. We obtain the system of ordinary differential equations for the leading terms in the power series, $n = 0$,

$$\mathcal{C}\rceil \quad \left(\frac{\eta_c T'}{T} + 2\right)U_0 - \eta_c U_0' - \frac{T'}{T^2}V_0 + \frac{1}{T}V_0' + W_0 - \left(\frac{FT'}{T^2} + \frac{2F'}{T}\right)T_0 + \frac{F}{T}T_0' = 0, \tag{C 8}$$

$$\mathcal{X}| \quad (2F' - \eta_c F'')\,U_0 - \left[F + \left(\frac{\mu}{T}\right)'\right]U_0' - \frac{\mu}{T}U_0'' + \frac{F''}{T}V_0 + \left[\frac{FF''}{T} - \left(\frac{\mu' F''}{T}\right)'\right]T_0$$

$$- \frac{\mu' F''}{T} T_0' = 0, \tag{C 9}$$

$$\mathcal{Y}| \;\; P_0' = 0, \tag{C 10}$$

$$\mathcal{Z}| \;\; \left(F + \frac{\mu' T'}{T} - \frac{\mu T'}{T^2}\right) W_0' + \frac{\mu}{T} W_0'' = 0, \tag{C 11}$$

$$\mathcal{E}\rfloor \;\; -\eta_c T' U_0 - \frac{2M^2(\gamma-1)\mu F''}{T} U_0' + \frac{T'}{T} V_0 + \left[\frac{FT' + 2TF'}{T} - \frac{1}{\mathtt{Pr}}\left(\frac{\mu' T'}{T}\right)' \right.$$
$$\left. - \frac{\mathtt{M}^2(\gamma-1)F''^2\mu'}{T}\right] T_0 - \left(F + \frac{2\mu' T'}{\mathtt{Pr}T} - \frac{\mu T'}{\mathtt{Pr}T^2}\right) T_0' - \frac{\mu}{\mathtt{Pr}T} T_0'' = 0, \tag{C 12}$$

and the system of ordinary differential equations for the second-order terms in the power series, $n = 1$,

$$\mathcal{C}\rceil \;\; \left(\frac{\eta_c T'}{T} + 3\right) U_1 - \eta_c U_1' - \frac{T'}{T^2} V_1 + \frac{1}{T} V_1' + W_1 - \left(\frac{FT'}{T^2} + \frac{3F'}{T}\right) T_1 + \frac{F}{T} T_1' = 0, \tag{C 13}$$

$$\mathcal{X}| \;\; (3F' - \eta_c F'')U_1 - \left[F + \left(\frac{\mu}{T}\right)'\right] U_1' - \frac{\mu}{T} U_1'' + \frac{F''}{T} V_1 + \left[\frac{FF''}{T} - \left(\frac{\mu' F''}{T}\right)'\right] T_1$$
$$- \frac{\mu' F''}{T} T_1' = 0, \tag{C 14}$$

$$\mathcal{Y}| \;\; P_1' = \left[\eta_c(TF' - FT - FT') + \eta_c^2 F'' T - \frac{4\mu' T'}{3}\right] U_0 + \frac{1}{3}\left[\mu - \eta_c T \left(\frac{\mu}{T}\right)'\right] U_0'$$
$$- \frac{\eta_c \mu}{3} U_0'' + \left(-F' - \eta_c F'' + \frac{FT'}{T}\right) V_0 + \left[F + \frac{4}{3}\left(\frac{\mu}{T}\right)'\right] V_0' + \frac{4\mu}{3T} V_0'' - \frac{2\mu' T'}{3} W_0$$
$$+ \frac{\mu}{3} W_0' + \left[FF' + \frac{F^2 T'}{T} + 3\mu' F'' - \eta_c (FF')' + \eta_c T \left(\frac{\mu' F''}{T}\right)' - \frac{4}{3}\left(\frac{\mu' T' F}{T}\right)'\right] T_0$$
$$+ \left(\eta_c \mu' F'' - \frac{4\mu' T' F}{3T}\right) T_0', \tag{C 15}$$

$$\mathcal{Z}| \;\; -F' W_1 + \left(F + \frac{\mu' T'}{T} - \frac{\mu T'}{T^2}\right) W_1' + \frac{\mu}{T} W_1'' + k_z^2 T P_0 = 0, \tag{C 16}$$

$$\mathcal{E}\rfloor \;\; -\eta_c T' U_1 - \frac{2\mathtt{M}^2(\gamma-1)\mu F''}{T} U_1' + \frac{T'}{T} V_1 + \left[\frac{FT' + 3TF'}{T} - \frac{1}{\mathtt{Pr}}\left(\frac{\mu' T'}{T}\right)' \right.$$
$$\left. - \frac{\mathtt{M}^2(\gamma-1)F''^2\mu'}{T}\right] T_1 - \left(F + \frac{2\mu' T'}{\mathtt{Pr}T} - \frac{\mu T'}{\mathtt{Pr}T^2}\right) T_1' - \frac{\mu}{\mathtt{Pr}T} T_1'' = 0. \tag{C 17}$$

These two systems must be solved by imposing the wall no-slip conditions on the velocity and a null temperature gradient at the wall. The boundary conditions for $\eta \to \infty$ are found by expanding (C 2)-(C 6) for $\hat{x} \to 0$ and $\eta = \mathcal{O}(1)$. It follows that

$$\bar{v} \to -\overline{\eta} - \frac{i}{2}(2\hat{x})^{1/2}(k_y + i|k_z|)\left(\overline{\eta}^2 + 1\right)$$

$$+ \frac{|k_z|}{(2\hat{x})^{1/2}}\left[1 - |k_z|(2\hat{x})^{1/2}\overline{\eta}\right]\int_0^{\hat{x}} g(\breve{x})\mathrm{e}^{-ik_x\mathrm{R}\breve{x}}\mathrm{d}\breve{x} + \dots\,, \tag{C 18}$$

$$\bar{w} \to 1 + (2\hat{x})^{1/2} i\left(k_y + i|k_z|\right)\overline{\eta} + k_z^2\int_0^{\hat{x}} g(\breve{x})\mathrm{e}^{-ik_x\mathrm{R}\breve{x}}\mathrm{d}\breve{x} + \dots\,. \tag{C 19}$$

The small-$\hat{x}$ asymptote of the unknown function $g(\hat{x})$ must now be found. We do this by matching (C 18) with the large-η limit of V_0 in (C 7). Introducing the viscosity-induced transpiration velocity V_c as

$$V_c = -\lim_{\eta\to\infty}(V_0 - \overline{\eta}), \tag{C 20}$$

we find that for $\hat{x} \to 0$

$$g(\hat{x}) \to -\frac{V_c}{|k_z|(2\hat{x})^{1/2}} + g_1 + \dots, \tag{C 21}$$

where the constant g_1 is unknown at this point. Matching with the solution for pressure (5.31) of Leib *et al.* (1999) shows that $P_0 \to -V_c/|\kappa|$ and $P_1 \to g_1 + V_c\overline{\eta}$ for $\eta \to 0$. After substitution of (C 21) into (C 19) and comparing with the form of the power series, one finds that the boundary conditions for $\eta \to \infty$ of W_0 and W_1 are $W_0 \to 1$ and $W_1 \to i(k_y + i|k_z|)\overline{\eta} - V_c|k_z|$, respectively. The boundary conditions on U_0 and U_1 are also easily found by comparing (5.20) of Leib *et al.* (1999) and $\bar{\tau} = 0$ with the power series solution. Therefore, U_0 and $U_1 \to 0$ for $\eta \to \infty$. No boundary condition needs to be specified on the vertical velocity component, but the large-η asymptote of V_1 is useful for determining the constant g_1. Indeed, setting $U_1 = 0$ in the continuity equation (C 13) and using the large-η limit of W_1, one finds that for $\eta \to \infty$

$$V_1 = -i\left(k_y + i|k_z|\right)\left(\frac{\eta^2}{2} - \beta_c\eta\right) + V_c|k_z|\eta + c_1, \tag{C 22}$$

where c_1 is a constant depending on k_y and k_z. Matching the above expression with the $\mathcal{O}((2\hat{x})^{1/2})$ term of (C 18) yields

$$g_1 = \frac{2c_1}{|k_z|} + 2V_c\beta_c + \frac{i}{|k_z|}\left(\beta_c^2 + 1\right)\left(k_y + i|k_z|\right). \tag{C 23}$$

(iii) Finally, comparing (C 7) with the small-x expansion (C 2)-(C 6), we find their common parts, denoted by $\overline{v}_c$, $\overline{w}_c$ and $\overline{p}_c$, as follows:

$$\overline{v}_c = -\overline{\eta} - V_c + (2\hat{x})^{1/2}\left[-\frac{i}{2}(k_y + i|k|)\left(\overline{\eta}^2 + 1\right) + V_c|k_z|\overline{\eta} + \frac{1}{2}|k_z|g_1\right], \tag{C 24}$$

$$\overline{w}_c = 1 + (2\hat{x})^{1/2}\Big[i(k_y + i|k_z|)\overline{\eta} - V_c|k_z|\Big], \tag{C 25}$$

$$\overline{p}_c = \frac{P_0}{(2\hat{x})^{1/2}} + g_1 + V_c\overline{\eta}. \tag{C 26}$$

REFERENCES

Boiko, A.V., Ivanov, A.V., Kachanov, Y.S. & Mischenko, D.A. 2010*a* Investigation of weakly-nonlinear development of unsteady Görtler vortices. *Thermophys. Aeromech.* **17** (4), 455–481.

Boiko, A.V., Ivanov, A.V., Kachanov, Y.S. & Mischenko, D.A. 2010*b* Steady and unsteady Görtler boundary-layer instability on concave wall. *Europ. J. Mech. B/Fluids* **29** (2), 61–83.

Boiko, A.V., Ivanov, A.V., Kachanov, Y.S., Mischenko, D.A. & Nechepurenko, Y.M. 2017 Excitation of unsteady Görtler vortices by localized surface nonuniformities. *Theor. Comput. Fluid Dyn.* **31** (1), 67–88.

Borodulin, V.I., Ivanov, A.V., Kachanov, Y.S. & Mischenko, D.A. 2017 Systematic study of distributed excitation of unsteady Görtler modes by freestream vortices. *Eur. J. Mech. - B/Fluids* .

Cebeci, T. 2002 *Convective Heat Transfer*. Springer-Verlag, Berlin Heidelberg.

Chen, F.J., Malik, M.R. & Beckwith, I.E. 1992 Gortler instability and supersonic quiet nozzle design. *AIAA J.* **30** (8), 2093–2094.

Choudhari, M. 1996 Boundary layer receptivity to three-dimensional unsteady vortical disturbances in the free stream. *AIAA Paper 96-0181* .

Ciolkosz, L.D. & Spina, E.F. 2006 An experimental study of Görtler vortices in compressible flow. *AIAA Paper* (4512), 1–21.

Dando, A.H. & Seddougui, S.O. 1993 The compressible Görtler problem in two-dimensional boundary layers. *IMA J. Appl. Math.* **51** (1), 27–67.

De Luca, L., Cardone, G., Aymer de la Chevalerie, D. & Fonteneau, A. 1993 Görtler instability of a hypersonic boundary layer. *Exp. Fluids* **16**, 10–16.

Denier, J.P., Hall, P. & Seddougui, S.O. 1991 On the receptivity problem for Görtler vortices: vortex motions induced by wall roughness. *Phil. Trans. R. Soc. Lond. A* **335** (1636), 51–85.

El-Hady, N.M. & Verma, A.K. 1983 Growth of Görtler vortices in compressible boundary layers along curved surfaces. *J. Eng. Applied Sc.* **2** (3), 213–238.

Finnis, M.V. & Brown, A. 1997 The linear growth of Görtler vortices. *Int. J. Heat and Fluid Flow* **18** (4), 389–399.

Flechner, S.G., Jacobs, P.F. & Whitcomb, R.T. 1976 A high subsonic speed wind tunnel investigation of winglets on a representative second-generation jet transport wing. *NASA TN D-8264* .

Floryan, J.M. 1991 On the Görtler instability of boundary layers. *Prog. in Aerosp. Sci.* **28** (3), 235–271.

Floryan, J.M. & Saric, W.S. 1982 Stability of Görtler vortices in boundary layers. *AIAA J.* **20** (3), 316–324.

Ginoux, J.J. 1971 Streamwise vortices in reattaching high-speed flows: a suggested approach. *AIAA J.* **9** (4), 759–760.

Goldstein, M.E. 1978 Unsteady vortical and entropic distortions of potential flows round arbitrary obstacles. *J. Fluid Mech.* **89**, 433–468.

Goldstein, S. 1938 *Modern developments in fluid dynamics: an account of theory and experiment relating to boundary layers, turbulent motion and wakes*, , vol. 1. Clarendon Press.

Görtler, H. 1940 Uber eine Dreidimensionale Instabilitat Laminarer Grenzschichten am Konkaven Wanden. *Naschr Wiss Gas, Gottingen Math Phys Klasse* **2** (1).

Graziosi, P. & Brown, G.L. 2002 Experiments on stability and transition at Mach 3. *J. Fluid Mech.* **472**, 83–124.

Gulyaev, A.N., Kozlov, V.E., Kuzenetsov, V.R., Mineev, B.I. & Sekundov, A.N. 1989 Interaction of a laminar boundary layer with external turbulence. *Fluid Dynamics. Translated from Izv, Akad. Navk. SSSR Mekh. Zhid. Gaza 6, vol. 5, pp. 55-65.* **24** (5), 700–710.

Hall, P. 1983 The linear development of Görtler vortices in growing boundary layers. *J. Fluid Mech.* **130**, 41–58.

Hall, P. 1990 Görtler vortices in growing boundary layers: the leading edge receptivity problem, linear growth and the nonlinear breakdown stage. *Mathematika* **37** (74), 151–189.

HALL, P. & FU, Y. 1989 On the Görtler vortex instability mechanism at hypersonic speeds. *Theor. Comp. Fluid Dyn.* **1** (3), 125–134.

HALL, P. & MALIK, M. 1989 The growth of Görtler vortices in compressible boundary layers. *J. Eng. Math.* **23** (3), 239–251.

HAMMERLIN, G. 1961 Über die Stabilität einer kompressiblen Strömung längs einer konkaven Wand bei verschiedenen Wand-temperaturverhältnissen. *Deutsche Versuchsanstalt für Luftfahrt* (176).

KEMP, N. 1951 The laminar three-dimensional boundary layer and a study of the flow past a side edge. *MSc Thesis, Cornell University* .

KOBAYASHI, R. & KOHAMA, Y. 1977 Taylor-Görtler instability of compressible boundary layers. *AIAA J.* **15** (12), 1723–1727.

KOTTKE, V. 1988 On the instability of laminar boundary layers along concave walls towards Görtler vortices. In *Propagation in Systems Far from Equilibrium*, pp. 390–398. Springer.

LAUFER, J. 1954 Factors affecting transition Reynolds numbers on models in supersonic wind tunnels. *J. Aero. Sc.* **21**, 497–498.

LEIB, S.J., WUNDROW, D.W. & GOLDSTEIN, M.E. 1999 Effect of free-stream turbulence and other vortical disturbances on a laminar boundary layer. *J. Fluid Mech.* **380**, 169–203.

LI, F., CHOUDHARI, M., CHANG, C.-L., GREENE, P. & WU, M. 2010 Development and breakdown of gortler vortices in high speed boundary layers. In *48th AIAA Aero. Sc. Meeting*, p. 705.

LIEPMANN, H.W. 1945 Investigation of boundary layer transition on concave walls. *NACA Wartime Rep. W87* .

MANGALAM, S.M., DAGENHART, J.R., HEPNER, T.F. & MEYERS, J.F. 1985 The Görtler instability on an airfoil. *AIAA Paper* **85-0491**.

MARENSI, E. & RICCO, P. 2017 Growth and wall-transpiration control of nonlinear unsteady Görtler vortices forced by free-stream vortical disturbances. *Phys. Fluids* **29** (11), 114106.

MARENSI, E., RICCO, P. & WU, X. 2017 Nonlinear unsteady streaks engendered by the interaction of free-stream vorticity with a compressible boundary layer. *J. Fluid Mech.* **817**, 80–121.

MATSUBARA, M. & ALFREDSSON, P.H. 2001 Disturbance growth in boundary layers subjected to free-stream turbulence. *J. Fluid Mech.* **430**, 149–168.

MAYLE, R.E. 1991 The role of laminar-turbulent transition in gas turbine engines. *J. Turbom.* **113** (4), 509–537.

OVCHINNIKOV, V., CHOUDHARI, M.M. & PIOMELLI, U. 2008 Numerical simulations of boundary-layer bypass transition due to high-amplitude free-stream turbulence. *J. Fluid Mech.* **613**, 135–169.

REN, J. & FU, S. 2015 Secondary instabilities of Görtler vortices in high-speed boundary layer flows. *J. Fluid Mech.* **781**, 388–421.

RICCO, P., LUO, J. & WU, X. 2011 Evolution and instability of unsteady nonlinear streaks generated by free-stream vortical disturbances. *J. Fluid Mech.* **677**, 1–38.

RICCO, P., TRAN, D.-L. & YE, G. 2009 Wall heat transfer effects on Klebanoff modes and Tollmien-Schlichting waves in a compressible boundary layer. *Phys. Fluids* **21** (024106).

RICCO, P., WALSH, E.J., BRIGHENTI, F. & MCELIGOT, D.M. 2016 Growth of boundary-layer streaks due to free-stream turbulence. *Int. J. Heat Fluid Flow* **61**, 272–283.

RICCO, P. & WU, X. 2007 Response of a compressible laminar boundary layer to free-stream vortical disturbances. *J. Fluid Mech.* **587**, 97–138.

SARIC, W.S. 1994 Görtler vortices. *Annu. Rev. Fluid Mech.* **26** (1), 379–409.

SCHNEIDER, S.P. 2008 Development of hypersonic quiet tunnels. *J. Spacecr. Rock.* **45-4**, 641–664.

SPALL, R.E. & MALIK, M.R. 1989 Görtler vortices in supersonic and hypersonic boundary layers. *Phys. Fluids* **1** (11), 1822–1835.

STEWARTSON, K. 1964 *The theory of laminar boundary layers in compressible fluids*. Oxford, Claredon Press.

SWEARINGEN, J.D. & BLACKWELDER, R.F. 1983 Parameters controlling the spacing of streamwise vortices on concave walls. *AIAA Paper* (83-0380).

TANI, I. 1962 Production of longitudinal vortices in the boundary layer along a concave wall. *J. Geophys. Res.* **67** (8), 3075–3080.

Viaro, S. & Ricco, P. 2018 Neutral stability curves of low-frequency Görtler flow generated by free-stream vortical disturbances. *J. Fluid Mech.* **845** (R1).

Volino, R.J. & Simon, T.W. 1995 Bypass transition in boundary layers including curvature and favorable pressure gradient effects. *J. Turbomach.* **117** (1), 166–174.

Wadey, P.D. 1992 On the linear development of Görtler vortices in compressible boundary layers. *Europ. J. Mech. B/Fluids* **11**, 705–717.

Wang, Q.-C., Wang, Z.-G. & Zhao, Y.-X. 2018 Visualization of Görtler vortices in supersonic concave boundary layer. *J. Visual.* **21** (1), 57–62.

Whang, C.W. & Zhong, X. 2002 Receptivity of Görtler vortices in hypersonic boundary layers. *AIAA Paper 2002-0151* .

Whang, C.W. & Zhong, X. 2003 Leading edge receptivity of Görtler vortices in a Mach 15 flow over a blunt wedge. *AIAA Paper 2003-0790* .

Wu, X. & Moin, P. 2009 Direct numerical simulation of turbulence in a nominally zero-pressure-gradient flat-plate boundary layer. *J. Fluid Mech.* **630**, 5–41.

Wu, X., Zhao, D. & Luo, J. 2011 Excitation of steady and unsteady Görtler vortices by free-stream vortical disturbances. *J. Fluid Mech.* **682**, 66–100.

Xu, D., Zhang, Y. & Wu, X. 2017 Nonlinear evolution and secondary instability of steady and unsteady Görtler vortices induced by free-stream vortical disturbances. *J. Fluid Mech.* **829**, 681–730.